An Efficient Propulsion System for Small Underwater Vehicles

by

Stefan Deucker

Vordiplom
Universtät Hamburg

Submitted to the Department of Ocean Engineering
in partial fulfillment of the requirements for the degree of

Master of Science

at the

MASSACHUSETTS INSTITUTE OF TECHNOLOGY

February 1997

Signature of Author .....
Department of Ocean Engineering
1.17.1997

Certified by .....
Dr. James Bellingham
Principal Research Engineer MIT Sea Grant
Thesis Supervisor

Accepted by .....
Prof. Kim J.Vandiver
Chairperson, Department Committee on Graduate Students

An Efficient Propulsion System for Small Underwater Vehicles

by

Stefan Deucker

Submitted to the Department of Ocean Engineering
on 1.17.1997, in partial fulfillment of the
requirements for the degree of
Master of Science

Abstract

The range and endurance of small, survey-class Autonomous Underwater Vehicles (AUVs) depends strongly on the efficiency of the propulsion system, as it is the major energy consumer. Odyssey II, a survey-class AUV developed by MIT Sea Grant, is a typical example of such vehicle platforms.

The research presented in this thesis leads to a thorough understanding of AUV propulsion performance, provides propulsion system design-tools, and identifies a more efficient propulsion system for the Odyssey II vehicle. The computational model of a thruster includes an electric permanent magnet DC motor and its thermal effects, viscous and frictional losses, the shaft seal and the gearbox. In connection with a propulsor design code, this computational model enables the designer to match thruster and propulsor to achieve maximum system performance. Additionally, the thruster unit currently used in Odyssey is investigated experimentally and the occurring losses inherent to each component are quantified. Since the Odyssey II thruster is characteristic of those used in other deep AUVs, the model and tools developed here are directly applicable.

The evaluation of design options has revealed a promising design of a propulsion system design for the Odyssey II vehicle with an estimated system efficiency of 59%.

Thesis Supervisor: Dr. James Bellingham
Title: Principal Research Engineer MIT Sea Grant

Contents

List of Figures

List of Tables

Acknowledgments

für meine Eltern,

für ihre Liebe und Unterstützung die all dies ermöglichte

The successful completion of this thesis was made possible by the friendly support of many people, who I would like to thank here. First of all, I would like to thank the people at the MIT Sea Grant Autonomous Underwater Vehicle Laboratory who made my work there enjoyable as I had the fortune to work with people who I like and respect. Special appreciation is due to my advisor Dr. James Bellingham, Dr. Thomas Vaneck and Dr. James Bales for their many insights and encouragements along the way. Furthermore, I would like to thank my academic advisor Prof. Douglas Carmichael as well as Joseph Curcio, Dr. Bradley Moran, Dr. Thomas Consi, Franz Hover, Farzam Toudeh-Fallah, Joseph Ziehler and Robert Grieve from MIT Sea Grant.

Great gratitude is due to Benthos for lending the dynamometer. Special thanks there to Samuel Patterson for his friendly help and patience.

Last, but not least, I would like to thank Albert Bradley from the Woods Hole Oceanographic Institution for answering all my questions and being the best teacher I have ever met.

This work was supported by the Office of Naval Research under contract N00014-95-1-1316, and by MIT Sea Grant College Program under contract NA46RG0434.

Chapter 1

Introduction

Among the oceanographic scientific community and the offshore industry, there exists a need for economical access to the ocean and its abyssal depths. Historically, most deep-water oceanographic data have been gathered from towed instrument platforms or sleds. Another class of tethered platform is the remotely operated vehicle (ROV), commonly used in offshore oil activity, which provides many of the advantages of manned submersibles at lower cost and significantly reduced risk to humans.

Both of these systems place few constraints on payload size, power consumption, or data transmission rate. The major drawback of both is that large-lateral-scale surveys are precluded by the presence of the tether. In addition, the inherent drag of the tether limits the operating speed drastically. Furthermore, for deep-water use, both systems require a large operating vessel, at tremendous cost.

Small autonomous underwater vehicles (AUVs) have the potential to provide economical access to the ocean. Lacking a tether and needing only a small vessel for deployment, AUVs can increase the effectiveness of oceanographic research by a factor of two to ten [4] at significantly reduced cost, depending on the exact circumstances of the mission. In particular, small vehicles can be operated with minimal logistic support from remote sites, off small ships, or in rough seas. Additionally, they have the potential for low-cost fabrication as a variety of inexpensive manufacturing techniques can be used that are not available for larger vehicles.

Many applications exist for this class of extended-survey AUVs. Scientific and industrial applications include, for example, under ice studies, offshore oil operations, large scale ocean struc-

ture surveys, environmental and pollution monitoring and rapid response to episodic events.

1.1 The AUV Odyssey II

MIT Sea Grant has designed, built and deployed five of the Odyssey II class AUVs. The vehicles are 2.2 meters long and weigh about 195 kilograms. The fairings and mechanical structures of these vehicles are integral, and constructed entirely of polyethylene. Polyethylene is robust, acoustically transparent for frequencies up to 25 kHz and is inexpensive to manufacture. Two glass spheres in each AUV provide pressure housing for the electronics and the batteries. The thruster, a commercially available product, has been matched with an off-the-shelf propeller. One configuration of the vehicle, carrying C&T (Conductivity and Temperature) probes in the nose and an ADCP (Acoustic Doppler Current Profiler) in the midsection, is shown in Figure 1-1.

Similar deep ocean, extended-survey AUVs include the Advanced Unmanned Search System, AUSS, built and operated by the Naval Ocean Systems Center, the French vehicle, Epaulard, the Soviet MT-88 and the Woods Hole Oceanographic Institution's Autonomous Benthic Explorer, ABE.

1.2 Motivation

The performance of AUVs is limited by the finite energy that can be stored within the vehicle. Maximizing the vehicle's performance requires a low-drag vehicle, coupled with efficient propulsion, and electronics that consume minimum power.

A major consideration in the design of a small AUV is the trade-off between range and payload capacity. The maximum range for this kind of vehicles occurs when approximately $\frac{2}{3}$ of the available energy is spent on electronics and $\frac{1}{3}$ on propulsion [7]. In practice the maximum available energy is spent on propulsion. Since the propulsion system is the largest consumer of energy, its efficiency is crucial to maximize vehicle performance and endurance.

Odyseey II's propulsion system is typical for an extended survey AUV propulsion system. It consists of a brushless DC motor mated to a two-bladed propeller by means of a gearbox, allowing Odyseey II to operate at a speed in excess of 3 knots. The motor and gearbox are

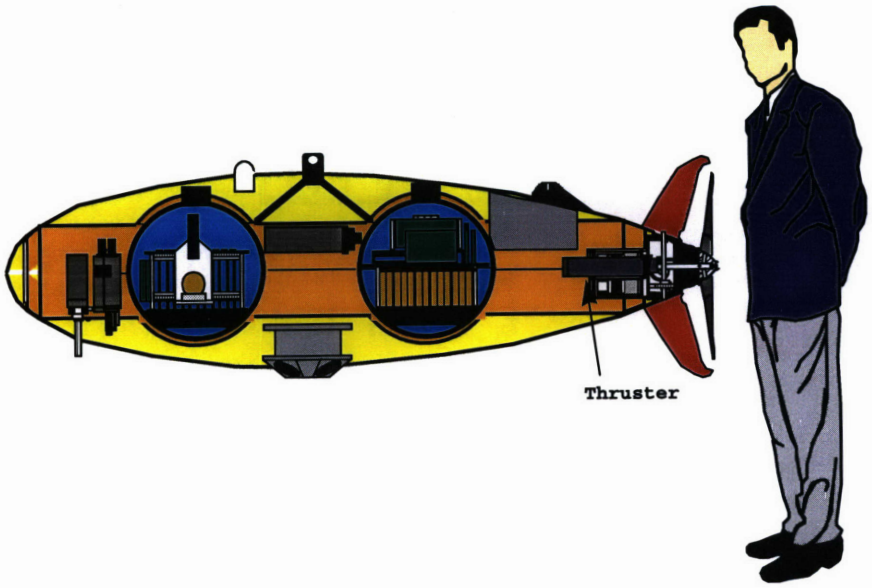

Figure 1-1: The Odyssey II Vehicle. The vehicle is about 2.2 m long and 0.6 m in diameter with the thruster located at the stern of the vehicle. (© Dr. James Bellingham, MIT Sea Grant)

enclosed in an oil-filled housing that prevents seawater intrusion, and permits the thruster to operate at ambient pressure.

Experience with Odyseey II during various missions has shown that the range and endurance of the vehicle are significantly reduced by its inefficient propulsion system. Preliminary tests revealed an overall system efficiency of about 20%, limiting the vehicle endurance to about three hours. This poor performance motivates this thesis, as an improved understanding and better design of the propulsion system is clearly needed to create a better design for the future.

1.3 Approach and Objectives

The task of the research presented in this thesis is to develop a thorough understanding of AUV propulsion performance and use this understanding to identify the most energy-efficient design. Furthermore, the required design tools to accomplish this task were developed or identified. While Odyssey II is selected as a typical vehicle platform, the approach and the results are valid for any AUV of similar design as the vehicles mentioned above.

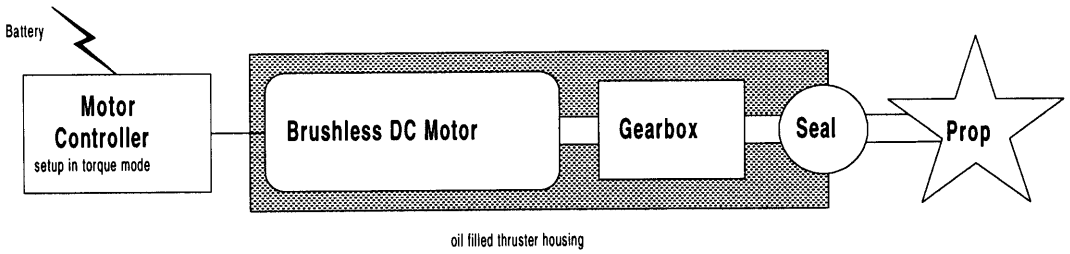

Figure 1-2: Schematic Propulsion System. The brushless DC motor controlled by an external motor controller, and the gearbox are enclosed in an oil-filled housing, tightened by a shaft-seal, forming the thruster, which is directly connected to the propulsor.

The following approach taken is taken. In Chapter 2 the requirements for the propulsion system of a survey-class AUV are stated in form of design specifications. Then, the propulsion system is broken down into two main components: thruster, converting electrical energy into mechanical energy, and a propulsor, converting mechanical energy into thrust. The components of the propulsion system is shown in Figure 1-2. The term 'thruster' describes the motor, gearbox and seal enclosed in the oil filled housing, and also includes the motor controller. Thruster and propulsor design options are identified and discussed. The method for accomplishing the propulsion system design is outlined.

In Chapter 3, a computational model of a thruster is developed. This model provides a design tool for motor selection and to match thruster and propulsor. The computational model takes characteristics of components usually found in thruster units into account as a permanent magnet electric motor and its thermal effects, viscous effects of the thruster fill fluid, the shaft seal and the gearbox. This extensive model allows an accurate match between thruster and propulsor.

Chapter 4 presents dynamometer tests investigating the performance of Odyseey II's thruster. The purpose of these tests is to investigate the characteristics of each component of the thruster experimentally and to quantify its inherent losses. These tests lead to a thorough understanding of the thruster and its performance influencing parameters. In Chapter 5, the computational model is verified using experimental data from the dynamometer tests.

In Chapter 6, the performance of different propulsion system design options is assessed using

the developed computational model and a propulsor design code, MIT-PLL. The outlined design path in Chapter 2 is applied to the Odyssey II example and the achievable system efficiencies are predicted leading to the identification of the most promising design option.

In Chapter 7 the findings of the conducted research are summarized.

1.4 Previous Work

Out of the variety of publications concerning propulsion of different vehicle-platforms, the following specialized underwater vehicle propulsors applicable to small, slow-moving underwater vehicles are discussed: ring thrusters [1] [34], counter-rotating ring thrusters [17], jet propulsion with a tilting nozzle [13], oscillating foil propulsion [2], electromagnetic seawater propulsion [26] and propeller stator propulsors [16]. The influence of thruster dynamics on underwater vehicle behavior has been investigated by Dana R. Yoerger et al. in 1990 [37].

Two publications specifically concerned with AUV propulsion system optimization are "A Systems Approach to AUV Propulsion Design", by Patrick K. Poole and Penn Clower [30] and "Propulsion Optimization for ABE, an AUV" by Thomas J. Woodford [36]. The first paper outlines an approach to AUV propulsion design, using a propeller-design-code developed by Patrick K. Poole, which is capable of designing one-stage screw propellers, and a simple permanent magnet electric DC motor model. The design cycle for the motor-gearbox-screw propeller design is discussed and examples of design cycles are given. The second paper presents the design of a single screw propeller tailored to ABE (Autonomous Benthic Explorer) with a matched motor and transmission. A lumped parameter model of the propulsion is developed and experimentally verified. The emphasis of this model is on dynamic responses of the propulsion system employing a ducted propeller.

The contribution of this thesis is the systematic assessment of available AUV propulsion system design options using computational methods and Odyssey II as a design example. The development of a computational model of the thruster (when used in connection with a propulsor design program) enables a designer to match the thruster and propulsor accurately to maximize system performance. Additionally, the existing thruster used in Odyssey II is investigated experimentally and the losses inherent to each component are quantified.

Chapter 2

Design Considerations and Options

In the beginning of this chapter the requirements on the propulsion system of a small survey class AUV are stated. Following, the propulsion system is broken down into its two main components: thruster and propulsor, and an overview over actuator and propulsor options is given. Each option is briefly discussed and assessed with regard to its feasibility. After that, the design path for accomplishing the propulsion system design using the previously as advisable identified actuator and propulsor options is outlined.

2.1 Specifications

The specifications for the propulsion system of a survey class AUV can be summarized as follows:

- *Highly energy-efficient.* Range and endurance of the AUV are strongly dependent on the efficiency of the propulsion system as it is the major energy consumer. The peak efficiency is desired for steady state operation more than for transient states as acceleration, deceleration or maneuvering.

- *Delivers required thrust.* The propulsion system has to generate the required thrust to propel the vehicle at the design speed (3 knots for Odyssey). Moreover, the thrust has to be adjustable to reduce vehicle speed if afforded by the mission task. In general, the system's efficiency peak should be the operating point at design speed. It will be seen

that this choice favours the maximum vehicle speed to be the design speed.

- *Reliable.* A failure of the propulsion system makes it impossible for the vehicle to achieve the mission task. Furthermore, the possibility of losing the vehicle exists (e.g. under ice missions). Therefore, it is desirable to build up the system from well known components, with proven reliability. Additionally it is desirable to minimize the number of moving parts. Redundancy and robustness of components are also design considerations.

- *Small and Lightweight.* The available space is limited due to the size of the vehicle. Additionally, it is desirable to keep the vehicle as buoyant as possible to increase the capacity for payload or additional batteries. Therefore, the propulsion system should be as lightweight as possible.

- *Main mechanical components are off-the-shelf products.* To keep the construction and development costs of the propulsion system low it is desirable to use as many commercially available components as possible. Furthermore, commercial products are mature and can be replaced easily if defect.

- *Easy and efficient to control.* The control of the propulsion system should be energy-efficient and easily controllable.

- *Does not interfere with electronics.* The electronic components of the propulsion system should not generate electric noise that interferes with other electronics of the vehicle.

- *Noise in acoustical neutral range.* The acoustic noise emitted from the motor and gearbox might interfere with the vehicle's navigation or communication system, which are based on acoustic signals. Commercial products for acoustic navigation and communication usually operate in the frequency range form 7 to 30 kHz and it is therefore desirable to minimize thruster noise within this frequency band. The frequency range for navigation and communication is dictated by the trade-off between bandwidth and maximum signal-range, which increases and decreases, respectively with frequency.

2.2 Design Options

The dominant design specification for the propulsion system is the requirement for high efficiency. In order to meet this specification and as many of the others as possible, the components of the propulsion system have to be chosen, designed, and matched very carefully.

The propulsion system can be broken down into two main components. The first, the thruster, converts electrical into mechanical energy. The second component is a propulsor, converting the mechanical energy supplied by the thruster into hydrodynamic thrust to move the vehicle through the water. Most modern underwater propulsions systems are one of two types. The first employs a conventional electric motor in a one-atmosphere housing with a gear-reduction stage and high-pressure shaft-seal. The other standard approach has no gear reduction but requires special seals and special high speed propellers. As one-atmosphere housings and the required shaft-seals are expensive for deep ocean applications, the housing can be flooded with oil to compensate for the ambient pressure and only a simple, low-frictional shaft-seal needs to be employed. Batteries are usually used as the energy source and the motors employed are usually direct current motors.

An emerging underwater vehicle propulsion system are ring thrusters [34] [1] [21]. In this integrated thruster concept, the stator of the electric motor is contained in the duct wall surrounding the propeller. The rotor forms a ring around the propeller and runs in the duct. There are several advantages to this technology. The bulk of the motor is removed and placed into a duct. A pressure or pressure-compensated housing is not needed. Ring thrusters with counter-rotating propellers promise especially good performance [17]. In general, ring thrusters are an attractive solution for thruster applications which require a high thrust using a small diameter propeller. It is not clear that their performance is comparable to slow moving, large diameter propulsors generating the same thrust. System-efficiency values are not published and therefore a direct comparison to other solutions is not possible. A major drawback of ring thrusters is that it can not be built from off-the-shelf products to match their design and power to a certain vehicle or mission task at low cost. Additionally, their design and manufacturing is expensive as both, the propulsor and the electric motor, have to be custom built for the vehicle.

2.2.1 Propulsor Options

The discussion of propulsor options in this section is restrained to feasible solutions. Promising, but currently infeasible options like the oscillating foil propulsion [2] or magnetohydrodynamic propulsors [26] are excluded. Furthermore, structure-dependent systems, like bottom crawlers or column creepers, are excluded as they are not compatible with various survey-class AUV mission tasks, which require a free swimming vehicle. This leaves propeller-based propulsors. for which the design and performance is well known and predictable due to an advanced propeller theory [19]. Computer programs for propeller design make it possible to design optimal propeller-based propulsors and to predict their efficiency under given operating conditions. Present propeller-based propulsor-design options are now reviewed.

Single Propeller

The single screw propeller was invented in 1836 and has been the prime-marine propulsor since the famous 'tug-of-war' in 1845, where the propeller powered warship 'Rattle' outperformed her paddle powered sistership 'Alecto'. A screw propeller relies on the principle of advancing an object by means of a rotating helical-screw. The primary energy losses occurring for a propeller operating in a fluid can be divided into viscous and rotational losses. Viscous losses are due to frictional losses through the interaction of the blades and the fluid, and drag forces due to flow separation. Rotational losses are due to the imparted rotational motion or 'swirl' to the fluid downstream, which constitutes a waste of energy as only the axial acceleration of the fluid produces thrust.

Rotational losses are dominant at low propeller rpm, whereas viscous losses are dominant at high propeller rpm (for a fixed propeller diameter). For a fixed propeller speed, rotational losses are dominant at a small diameter while viscous losses are dominant at a large propeller diameter. In-between is one point where viscous and rotational losses are sufficiently small to allow the propeller efficiency to peak.

Contra-Rotating-Propellers

Contra-rotating propellers can lead to a significant increase in propulsor efficiency. The energy that a conventional propulsor expends in rotating the flow can be partially recovered by the use

of a contra-rotating pair of propellers. At the same time the opposite rotations of the two sets of blades cancel out the torque reaction. However, there is a substantial penalty of complexity in the design of the co-axial shafting with its bearings and the drive arrangements.

Vane Wheel

The Grim [32] vane wheel is a freely rotating set of blades installed behind a propeller. The inner part of the vane wheel takes power from the propeller slip stream and transforms it by acting as a turbine into additional thrust, which is produced by the outer part of the vane wheel by acting as a propeller. Vane wheels are usually about twenty percent larger in diameter than the propeller and operate at about forty percent of the propeller's rate of rotation.

Pre/Post-Swirl Stators

A row of stator blades placed upstream or downstream of the propeller can also be used for the purpose of swirl cancellation. As with contra-rotating propellers, these propeller/stator combinations can lead to significant increase in propulsor efficiency. The drawback of all these swirl-loss recovering solutions is that additional control surfaces have to be placed in the flow, which cause additional viscous losses. For a lightly loaded propulsor the rotational losses are small and therefore the balance between viscous and rotational losses is sensitive. In other words, the energy losses in the slip-stream have to be significant (as is the case for moderately to highly loaded propellers) for the positive effect of the stator blades is larger than their inherent viscous loss. Nevertheless, stator blades provide a effective mean to remove the unbalanced torque. Another advantage of stator blades compared to the previous two solutions for swirl cancelation is that no additional moving parts are required.

Ducted Propeller

A ducted propeller has a shroud or duct around the rotor. In an open propeller, the tips of the blades cannot provide much thrust as the pressure difference between the front and back of the blade causes the flow to spill over the end, resulting in a rotation of the fluid causing the tip vortex downstream. By designing the blading to run with a small clearance from the duct, the pressure difference between the two sides of the blade can be sustained. The duct

can also be used to control the flow at the rotor, which is desirable when high propeller loading is afforded. Additionally, a duct can easily be combined with stator blades carrying the duct. Another advantage of a duct is that it protects the propeller blades. Nevertheless, it adds drag to the vehicle and is quite expensive to manufacture if a small clearing between blade and duct is desirable. The duct's profile shape is usually a faired profile, e.g. a NACA profile 4415.

2.2.2 Actuator Options

After having identified propeller-based propulsors as the feasible solution, the discussion of actuators in this section is restricted to solutions which convert electrical into rotational mechanical energy as this is the natural motion of propellers. The energy supply in an AUV is usually a battery, which implies (together with the need for rotational mechanical energy) the use of rotary electric DC motors. While AC motors are less expensive than DC motors, the control of AC motors using a DC voltage supply is expensive, making the low cost of the motors secondary.

Rotary electric DC motors can be classified in two groups [18]: motors having brushes and commutator, and motors without commutator. In all DC motors it is necessary to commutate the motor windings to properly distribute the current through the windings as the motor rotates. In brushed DC motors this switching is performed mechanically by the use of sliding contact brushes. In an oil-filled housing the brushes experience an increased wear and tend to hydroplane on the non-conductive fill-fluid. The effect of hydroplaning brushes leads to an increased motor resistance and a higher thermal load on the motor. Furthermore, the resulting arc tends to break down the fill-fluid (mostly oil), resulting in corrosive components. Additionally, the brushes tend to chatter. Therefore, the life expectance of brushed motors is short in the presence of a fill-fluid, which is usually needed for deep ocean applications. Thus only brushless DC motors will be considered. Two different designs are available.

Brushless Permanent Magnet DC Motors

In addition to removing the problems associated with operating brushes in oil, brushless motors offer a higher dynamic-performance than their brushed equivalent. The continuous stall-torque, peak stall-torque and maximum operating speeds are significantly higher for brushless motors

than for a brushed motor of equal size.

Other advantages of a brushless permanent-magnet motor compared to brushed motors include better heat dissipation, smaller motor size, reduced noise, low E.M.I. (Electro-Magnetic-Interference) and a lifetime limited only by the bearing life. Disadvantages of brushless motors are their higher cost and more complicated control electronics.

Switched-Reluctance Motor

[23] [22] Switched-reluctance motors offer a comparable performance to brushless DC motors together with some interesting advantages. The efficiency plateau versus motor speed is broader than for brushless permanent-magnet DC motors. As no permanent-magnets are employed, whose magnetic-field-strength is degraded with increasing operating temperature, the heat restrictions placed on the operating conditions are relaxed. Furthermore, the elimination of permanent magnets and the simple construction make the switched-reluctance motor inexpensive compared to permanent-magnet motors. For most switched-reluctance motor designs, the phases act independently, offering high redundancy if independent power electronics for each phase are used.

Unfortunately there are also some disadvantages. Expensive controllers are required to achieve high motor performance with switched-reluctance motors. The surfaces of the rotor and stator are not smooth for production motors manufactured today and therefore suffer increased viscous losses compared to brushless permanent-magnet DC motors. Additionally, they produce more noise and are heavier than brushless permanent-magnet DC motors.

Nevertheless, switched-reluctance motors are a interesting alternative to brushless permanent-magnet DC motors, especially due to the broad efficiency plateau and the redundancy they offer. Switched reluctance motors are relatively new in the marketplace and established so far in power ranges from 0.5-300 kW. The available power range at this time is too high for Odyssey II.

2.3 Design Path

The steps required to meet the design specifications discussed at the beginning of this chapter are now outlined. The chosen approach is valid for any kind of streamlined, slow moving,

underwater vehicle which, employs a propeller based propulsor. Figure 2-1 illustrates the design path and each step of the design process outlined in the following is represented in the flowchart.

2.3.1 Required Thrust and Power

The first step, represented by box number 1 in the flowchart, is to estimate the required thrust and power to propel the vehicle at its design speed. In general terms, the resistance R_D of a body to motion through a fluid can be expressed in the formulation [27]

$$R_D = \frac{1}{2}\ C_D\, \rho\, U^2\, A, \tag{2.1}$$

where C_D is a drag coefficient related to the shape of the body, ρ is the density of the fluid, U is the speed of the body and A is a representative area of the body. U should be the design speed of the vehicle. Equation 6.1 is a half-empirical representation of the physical properties associated with the drag of a body. The drag coefficient C_D is dependent on the Reynolds number and the fluid density ρ is dependent on its temperature and the salinity. Nevertheless, equation 6.1 gives a good estimate for the vehicle drag. The required propulsive power is the product of the required thrust and the vehicle speed. The power requirement goes up as the cube of the vehicle speed whereas the vehicle drag goes up as the square of the vehicle speed.

2.3.2 Preliminary Drive Power Estimation and Motor Selection

The next step in the design process, represented by box number 2 in Figure 2-1, is to identify the drive motors that are available for the propulsion system. In the sections above, propeller-based propulsors and brushless permanent-magnet DC motors have been identified as the propulsion system components. The brushless permanent-magnet DC motor and PWM electronics for its control presently represent the state-of-the-art combination of low noise, low weight, and high efficiency [22]. The available switched-reluctance motors are too big for small, slow moving underwater vehicles so far. To select candidate drive motors, it is useful to estimate the power needed to propel the vehicle at the design speed. A method of estimating the required propulsive power has been presented in the previous paragraph. To determine the required power-out from the thruster to the propulsor, the hydrodynamic efficiency of the propulsor needs to be known.

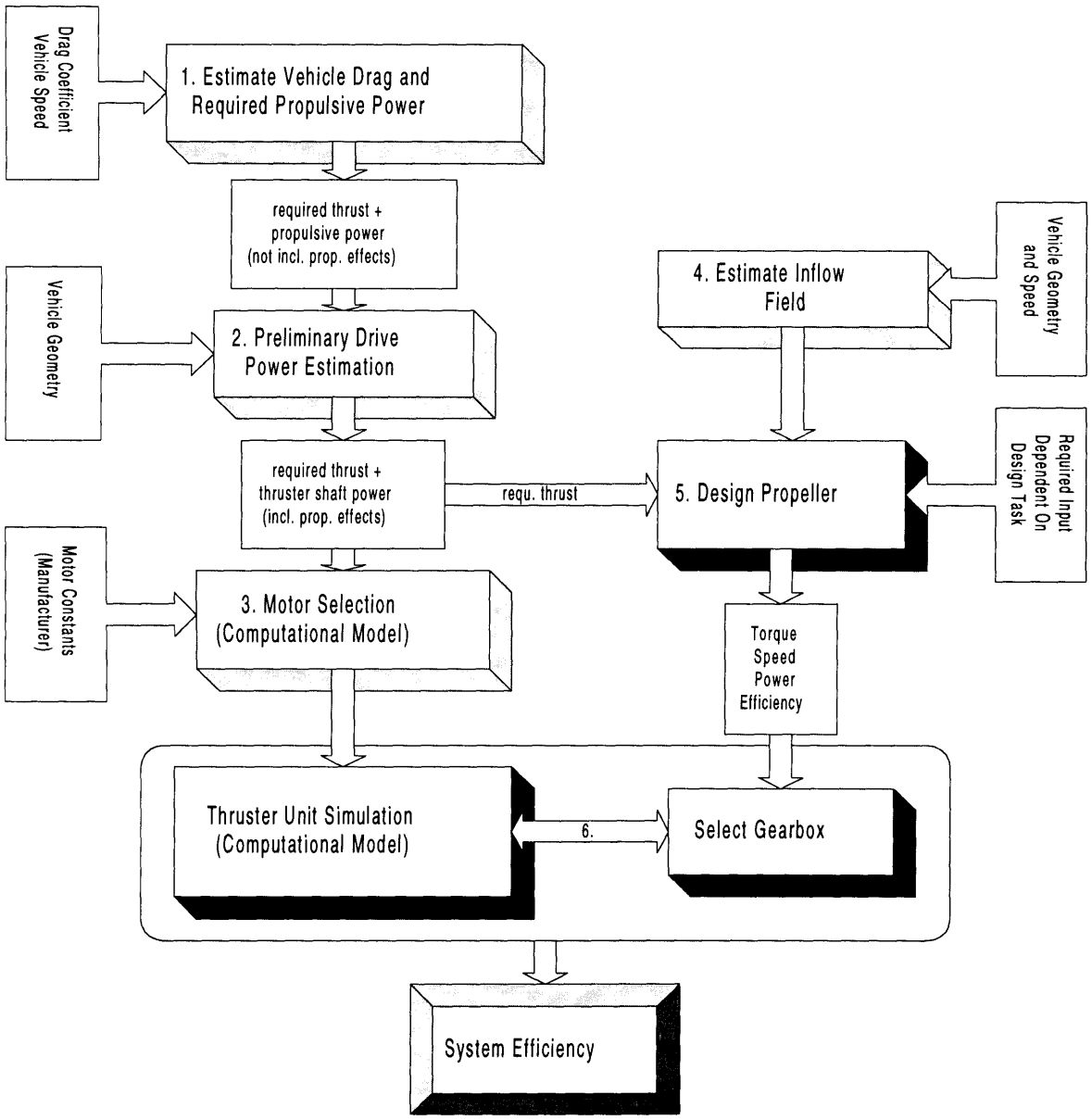

Figure 2-1: Design Process Flowchart. Step 1 in the design process is the estimation of the vehicle drag, not including the effects of the propulsor, followed by step 2, where the required thrust and thruster shaft-power is estimated including propulsor effects. Then, a motor for the thruster is selected in step 3, assuming an estimated gearbox-efficiency. Given an inflow-field into the propulsor, estimated in step 4, the propeller design program is used in step 5 to design a propulsor for specified operating conditions. The system efficiency is assessed applying step 6, where thruster and propulsor are mated together by means of a gearbox. The black-shadowed boxes mark the design steps which are repeated to assess different propulsion system solutions. Step 3 only needs to be revisted if the preliminary estimated propeller and gearbox efficiency in Step 2 was too far off from the calculated efficiencies in Step 5 and 6.

The efficiency of a propulsor can be divided into two parts: the efficiency of the device itself and effects arising from the interaction between the propulsor and the hull which is in close proximity.

The first part, the efficiency of the device itself, can be estimated using the 'Actuator Disc' model. It is the simplest representation of the ideal propeller. A constant pressure jump is somehow maintained over a disc of radius d placed in a uniform stream with speed U. By involving the momentum theorem and Bernoulli's equation it can be shown [19] that the efficiency of the actuator disk is

$$\eta_{ideal} = \frac{2}{1 + \sqrt{1 + \frac{T}{\frac{1}{2}\,\rho\, U^2\, \pi\, d^2}}}, \tag{2.2}$$

where T is the generated thrust. From this equation it can be seen that there is a benefit in having a large diameter propeller for a fixed vehicle speed and thrust. The actuator representation of a propeller contains no induced rotational velocities and no viscous losses. Therefore, the real propeller efficiency is significantly lower than the calculated ideal efficiency.

The second part of the propulsor efficiency arises from the interaction between the propulsor and the hull. The presence of the hull alters the free-flow velocity and therefore the inflow field into the propeller. The inflow field is estimated in the next section and is used by the propeller-design program to design an optimum propulsor in the given flow. Secondly, the pressure field around the propeller generally increases the resistance of the hull.

The propulsor develops its thrust by accelerating fluid through it. This acceleration effect extends forward and therefore the stern of the vehicle experiences a lower pressure than it would if it were towed. This in turn causes an increase in drag, which can be expressed in terms of the thrust deduction coefficient t

$$t = 1 - \frac{R_D}{T}, \tag{2.3}$$

where R_D is the resistance of the towed body and T the thrust. The coefficient t for submarines is tabulated as a function of the tailcone-angle in [9]. The required propulsive power for the self-propelled vehicle can then be estimated by solving Equation 2.3 for the thrust T and multiplying the obtained value with the vehicle design speed.

The required shaft-power of the thruster P_{req} can now be estimated as

$$P_{req} = P_{prop} \frac{1}{\eta_P \, \eta_G} = R_D \, U \frac{1}{\eta_{ideal} \, t} \frac{1}{\eta_P \, \eta_G}, \tag{2.4}$$

where P_{prop} is the required propulsive power, η_P the estimated propeller efficiency based on the calculated ideal propeller efficiency and η_G the estimated gearbox efficiency.

Having estimated the power required from the output shaft of the thruster, the computational model of the thruster presented in the next chapter can be used to assess and to choose between candidate motors with the task to identify a motor delivering the required power at high efficiency (box number 3 in the flowchart). If the operating point associated with P_{req} is close to the efficiency peak of the thruster and if the overall thruster efficiency is sufficiently high, an interesting thruster configuration has been identified.

2.3.3 The Inflow Field

Assuming that the propulsor is placed at the stern of the vehicle (for protection and because the bow is typically needed for sensors or tools), the inflow field into the propulsor is the free stream altered by the presence of the body. As the fluid passes around the hull it changes velocity. At the bow there is a stagnation point where the fluid velocity is zero. It then accelerates and has a speed slightly higher than the vehicle velocity around the sides. As the stern form reduces in diameter the fluid again slows down. In addition to the shape effects of the body, the viscosity effects of the fluid on the hull also slow down the fluid. Hence at the stern there is an area surrounding the tail of the hull where there is slow moving water, called the wake. It can be assumed that for streamlined hull forms and low speeds of advance no flow separation occurs.

The inflow field into the propulsor has an effect on the design and efficiency of the propulsor. Propeller design programs are capable of taking the effect of the wake into account given the inflow field into the propeller. Therefore the inflow field into the propulsor needs to be estimated. This is represented by box number 4 in Figure 2-1. The approach to calculate the inflow field is to represent the hull form using potential flow theory, yielding the fluid velocities on the surface of the hull. Then boundary-layer theory can be applied to estimate the velocity profiles around the hull and adjacent to the propulsor.

The thickness of the boundary-layer is dependent on the fluid velocity and on the extent of the surface in the direction of the flow. For small, slow-moving vehicles the thickness of the boundary-layer may not be significant for the propeller design and efficiency. Therefore it is useful to first estimate the boundary-layer thickness before conducting the potential flow calculations. The required calculations are outlined below.

An approximation for the hull surface is the flat plate. The fluid velocity is assumed to be uniform and equal to the speed of advance. For streamlined bodies the slopes of the hull are mostly small and therefore this is a reasonable approximation. An estimate for the inflow field can then be made by using the boundary-layer equations for laminar and turbulent flow.

The transition between laminar and turbulent flow occurs between $R_e = 10^5$ and $R_e = 2 * 10^6$, depending on the roughness of the surface and ambient turbulence, where R_e is the Reynolds number (a measure of inertia forces compared to viscosity forces) given by

$$R_e = \frac{U\, l}{\nu}, \tag{2.5}$$

where U is the fluid velocity, l a characteristic length and ν the viscosity of the fluid. After estimating the critical Reynolds number [27], equation 2.5 can be solved for the characteristic length l, giving the expected extent of the laminar boundary-layer over the surface of the body in the direction of the flow.

The thickness δ of the laminar boundary-layer can be estimated by using Blasius' solution for the flat plate

$$\delta = 4.9\, (\frac{\nu\, x}{U})^{\frac{1}{2}}, \tag{2.6}$$

where x is the point in question.

The rest of the vehicle's body will be covered with a turbulent boundary-layer. The thickness of the turbulent boundary-layer can be estimated by using the $\frac{1}{7}$-Power Approximation [27]

$$\delta = 0.373\, x\, (\frac{U\, x}{\nu})^{-\frac{1}{5}}. \tag{2.7}$$

The resulting thickness of the boundary-layer at the tail of the vehicle is then roughly the sum of the laminar and turbulent boundary-layers. If the thickness of the boundary-layer is

significantly smaller than the propeller diameter, the effect of the vehicle on the inflow field into the propeller can be neglected and the free, uniform stream is assumed to be the inflow field.

2.3.4 Propeller Design

Having determined the inflow field into the propulsor, the propulsor itself can be designed (box number 5 in Figure 2-1). Various design software-packages are available, based on different theoretical approaches, such as boundary-integral equation methods or streamline-curvature methods. The propeller design-tool used in this case to assess the propulsor design options discussed above is MIT-PLL (Propulsor Lifting Line), which is based on lifting-line theory for moderately-loaded propellers. Each blade of the propulsor is replaced by a straight, radial, lifting line. The geometry (pitch, chord, camber, thickness, etc.) of the physical propeller blade is replaced by a radial distribution of circulation, or loading. The advantage of this approach is that it can model two blade rows, enabling the user to assess unconventional propulsors as well as the influence of a duct. Thus, MIT-PLL is capable of modeling all propeller-based propulsors discussed above. Furthermore, MIT-PLL is used by the U.S. Navy for propeller design and has proved to be a reliable tool [27].

MIT-PLL requires a representation of the inflow field, an initial, approximate, description of the geometry of the propulsor including number of components, number of blades and component diameter. Additionally, the rate of rotation of the component, the vehicle speed and the required thrust need to be specified. Given these inputs, MIT-PLL then optimizes the circulation distribution on the lifting-lines representing the propeller blades. The goal is to find the load distribution which provides the prescribed thrust for a minimum torque. The contraction of the wake due to the propulsor is taken into account by MIT-PLL. Solid boundaries as a hub or a duct can be simulated by using an image vortex system. MIT-PLL can also estimate the optimum chord length (based on the trade-off between viscous losses and strength and cavitation considerations), calculate the effects of non-axis-symmetric stator blades, and calculate the effective wake.

MIT-PLL generates a variety of outputs. The most important ones are the recovered thrust, the efficiency of the propulsor and the required power. Furthermore the propulsor torque and thrust, torque and power coefficients are given. The quantities which are distributed over the

radius over the propeller are provided in a detailed output file. They include the estimated blade-section drag-coefficient, flow velocities and other quantities describing the flow and the loading.

The blade geometry is not defined by MIT-PLL, although properties such as the pitch, chord, camber and maximum thickness (which describe the shape of the lifting surface) are estimated and written to a file. The physical shape of the blade that will develop the circulation calculated by MIT-PLL can be obtained by using the Propeller Blade Design program MIT-PBD-14, which uses data generated by MIT-PLL.

The physical shape of the blade can be written by MIT-PBD-14 to files in standard surface (IGES) or solid-model (STL) format, which can be read by CAD software packages such as I-DEAS or AutoCAD. Within the CAD program the blades can be placed around the hub and the strength of the blades can be analyzed. When a satisfactory design is achieved the CAD program can produce files for a range of the manufacturing methods. These include CNC machining or rapid prototyping methods as stereolithography (SLA).

In summary, MIT-PLL allows the design of an optimum propeller for specified operating conditions. By varying parameters such as propeller rpm, propeller diameter, number of blades, etc. the optimum design can be found. The parameters that affect the design the thruster are the propeller torque and rotational speed, whose product is the required power.

2.3.5 Matching Thruster and Propulsor

The goal in matching the motor and the propulsor is to have both components operating at sufficiently high efficiencies to assure a good overall performance of the propulsion system. Electric motors usually have their peak efficiencies at high rotational-speed, whereas propulsors have their peak efficiencies at relatively low rotational-speed. To let both components operate at high efficiencies, a gearbox can be employed. The drawback of a gearbox is the inherent power loss and acoustic noise.

The two possible design solutions, with and without a gearbox, imply two types of thruster design. In the case of a gearbox, propulsive power is transmitted to the propulsor at a low rate of rotation and a high torque. The high torque can only be transmitted economically by a rigid shaft, which must pierce the thruster housing. Therefore, if a gearbox is used, the preferable

thruster design solution is an oil-filled housing with a relatively low-friction shaft-seal. In the other case, where no gearbox is employed, power is transmitted to the propulsor at a high rate of rotation and a low torque.

The design task is to maximize the efficiency of the overall system. Having a high gearbox-reduction-ratio to let motor and propulsor operate at high efficiencies causes significant losses in the gearbox, and it might pay-off to operate the propulsor at an operating point with a higher rate of rotation (and lower propulsor efficiency) to employ a gearbox with a smaller reduction-ratio and lower losses. The sensitivity of this trade-off is dependent on the sensitivity of the propulsor efficiency on its rotational speed and the sensitivity of the gearbox efficiency on the gearbox reduction ratio.

A good starting point is to first design the optimum propulsor for the specified operating conditions. The required parameters for the propeller design are in this case the desired vehicle speed and the required thrust. Then the chosen electric motor (Step 3 in Figure 2-1) is mated to the propeller by selecting a gearbox (Step 6 in Figure 2-1). The interfacing parameters between the thruster and the propulsor are the propulsor torque T_{prop} and rotational speed ω_{prop}, the shaft torque $T_{thruster}$, and the rotational speed $\omega_{thruster}$ from the thruster. These quantities are provided by the thruster model and the propulsor design-program. One uniquely-defined gearbox-ratio exists, which shifts the high motor-speed and low motor-torque to the required low propulsor-speed and high propulsor-torque, which allows both components to operate at high efficiencies ('Select Gearbox' in Figure 2-1). That gearbox ratio is found from

$$G = \frac{\omega_{thruster}}{\omega_{prop}} = \frac{T_{prop}}{T_{thruster}} \tag{2.8}$$

while

$$P = \omega_{thruster}\, T_{thruster} = \omega_{prop}\, T_{prop}. \tag{2.9}$$

The power losses occurring in the gearbox increase the required power-out of the electric motor slightly to compensate for these losses. This means that the desired operating point on the motor curve changes slightly and therefore also the gearbox reduction ratio. For the first iteration (iterations indicated by Step 6 in Figure 2-1) the thruster model, assuming no gearbox so far, can be used in connection with the required torque and speed of the propulsor, to determine

the required gearbox-reduction-ratio (Equation 2.8). For the second iteration the calculated gearbox-ratio is entered in the thruster model and thruster and propeller are matched again, resulting in a slightly changed gearbox-ratio. Experience has shown that no more than two iteration are usually needed to achieve a consistent gearbox-ratio.

The next step is to test the sensitivity of the trade-off between motor operating point, gearbox-reduction-ratio and propulsor-operating-point. The rate of rotation of the propulsor is increased (lowering its efficiency) and a new gearbox-ratio is determined. If the overall efficiency drops the design process is complete as a maximum has been found. If the overall efficiency increases, the rate of rotation of the propulsor is increased again, until the maximum is found. The boxes involved in this iteration are the blocks shadowed in black in Figure 2-1. The grey-shadowed blocks yield constant quantities for a given vehicle geometry and speed, and are independent from the thruster selection or propulsor design. Step 3 of the design process shown in Figure 2-1 has only to be revisited if the preliminary drive power estimation is too different from the values encountered during the propulsion system assessment, resulting in a shift of the thruster operating point away from the efficiency peak. In this case, a new motor has to be selected, delivering the required power-out at high efficiency. In general the gearbox trade-off has only a small influence on the required motor power-output and therefore the selected motor can mostly be used consistently.

The underlying assumption in this approach is that gearboxes are available in any reduction-ratio. This is not the case for off-the-shelf gearboxes. Nevertheless, the closest available gearbox can be chosen and then the system performance reevaluated to assess if the resulting system efficiency is sufficient.

There is a second possible design task in which a propulsor has to be matched to a given thruster torque and rotational speed. This design situation occurs if no or a predetermined gearbox is employed with a prescribed operating point for the thruster. Then, the propulsor speed is prescribed by the motor speed and the propulsor torque has to be adjusted by varying parameters the propulsor parameters (e.g. the diameter of the propulsor) to meet the desired operating point.

Chapter 3

Thruster Model

3.1 Introduction

In this chapter, the computational model of a thruster is presented. As outlined in the previous chapter, a representation of the thruster in the design process is required to select an optimum thruster and to assess the system efficiency. The representation of the thruster presented in the following is capable of modeling the components usually found in state-of-the-art thrusters. This includes the characteristics of an electric permanent-magnet DC motor, viscous losses due to a fill-fluid within the rotor-stator gap, frictional losses, thermal effects, a Crane shaft-seal and a planetary gearbox.

The Odyssey II propulsion system is a typical example of a propulsion systems employed in small AUVs. A brushless DC motor, which has its peak efficiencies at high rotational-speed, is linked to a propeller, which has its peak efficiencies at low-rotational speed, by means of a planetary gearbox, which ideally allows both components to operate at high efficiencies. The components are mostly off-the-shelf products mated together. The housing, which encloses the motor and gearbox is oil filled to compensate for the ambient pressure in deep-sea applications. This keeps the housing construction simple and to employ a low friction shaft-seal.

The parameters that need to be specified by the user as inputs to the model are usually provided by the manufacturer of the electric motor in form of motor constants. Furthermore, some parameters regarding motor geometry and the properties of the thruster components need to be specified. The user has the possibility to choose which parts of the thruster are taken

into account in the model. For example, the user can model a thruster with fill-fluid, gearbox and seal as well as a thruster without fill-fluid, gearbox and seal.

The computational model estimates the performance curves for the specified thruster configuration and operating conditions. An output file containing detailed thruster performance data is generated. Additionally, plots are displayed that show the performance.

In section 3.2 Theory, the approaches used to model the characteristics of the thruster are outlined. Section 3.3 The Program describes how the model incorporated the theory discussed in Section 3.2, its structure, and the input it requires. In the end of this chapter, a sample run of the computational model is displayed.

3.2 Theory

3.2.1 Expected Losses

Power losses within the thruster are due to armature power dissipation in the electric motor (referred to as I^2R losses) and torque losses in the mechanical components. Torque losses are expected to occur in the ball-bearings of the motor, in the gearbox, in the shaft-seal and in viscous losses associated with the fill-fluid. The total power losses can be closely estimated to be

$$P_l = I^2R + T_M\,\omega, \tag{3.1}$$

where I is the motor current, R the motor resistance, T_M the torque losses, and ω the motor speed.

Torque losses T_M within the thruster are due to two reasons: frictional losses and viscous losses. The characteristics of these two types of losses and where they are expected to occur are now discussed.

The influence of sliding friction is expected to occur in the ball-bearings of the motor, the gearbox and the seal. Sliding friction can be characterized by Coulomb's law

$$F_r = \mu\,F_n, \tag{3.2}$$

where F_r is the reactive force due to friction, μ the sliding friction coefficient, and F_n the normal

force between the surfaces in contact.

The coefficient μ depends on the materials in contact, the composition of their surfaces, the presence of a lubrication film, the lubrication conditions, the temperature and the humidity as well as, in part, on the velocity. Accordingly, the parameter μ is expected to fluctuate between certain limits over the operating range of the motor and to depend on the part in question.

The normal force, F_n, exerted by the seal on the shaft is constant, and (assuming the fluctuations of μ to be small) it can be expected that the reactive force in Equation 3.2 due to the seal is nearly constant over the operational range of the motor and only weakly dependent on motor speed. The frictional losses in the ball-bearings depend on the motor speed and the frictional losses in the planetary gears are a function of both, motor speed and load-torque.

Viscous losses, referred to as windage depend on the motor speed and the motor temperature (the temperature influences the viscosity of the fill-fluid). The main contribution of these losses occurs in the gap between stator and rotor of the motor. Assuming a Couette Flow [27] model, it can be expected that these losses increase linearly with motor speed. Windage in the gearbox is nonlinear and the positive effect of lubrication probably prevails.

3.2.2 The Brushless DC Motor

The performance characteristics of the motor are independent of the choice of mechanical versus electrical commutation. Mechanical commutation is achieved by the use of brushes. For electrical commutation, information about the rotor position is used by a motor controller to switch the stator windings correctly. The position sensor is called Hall effect sensor. A Hall effect sensor is typically located at the rear end of the electric motor and tells the motor controller the orientation of the rotor.

In an electric motor, electrical energy is converted into mechanical energy through the interaction of two magnetic fields. In this case, one field is produced by permanent-magnets on the rotor, whereas the other field is produced by an electrical current flowing in the stator windings of the motor. The resulting torque rotates the rotor. By commutating the current flowing in the windings, a continuous torque output is achieved.

A basic model describing this motor is shown in Figure 3-1. A circuit analysis of this

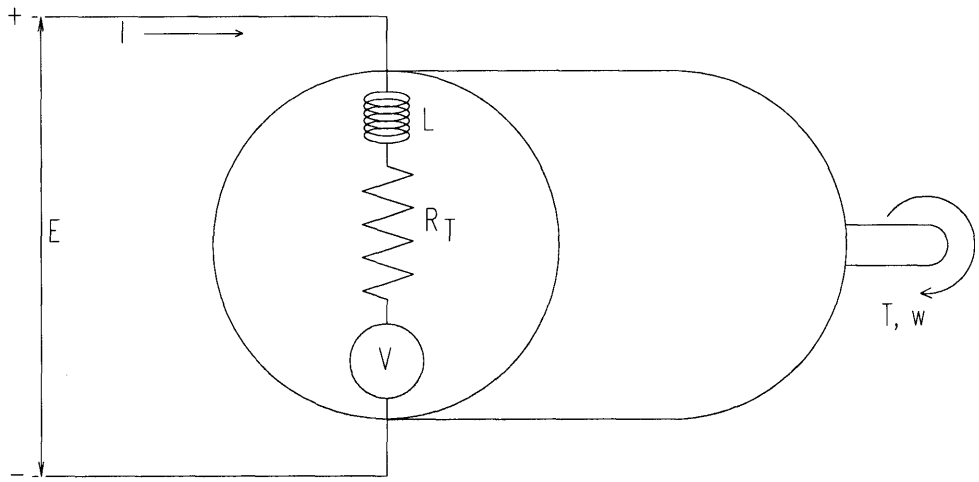

Figure 3-1: Motor Model. A circuit analysis yields the motor equation (Equation 3.3), where E is the applied voltage, I the motor current, L the winding inductance, R_T the winding resistance and V the back emf voltage. The mechanical power-out is $T * \omega$.

diagram yields the motor equation

$$E = I\,R_T + V + L\,\frac{dI}{dt}, \tag{3.3}$$

which is basically a voltage balance within the shown circuit. In this model, E is the applied voltage, I the motor current, L the winding inductance, R_T the motor resistance and V the back emf voltage (the induced voltage produced by the relative motion between the permanent-magnet field and the winding coils). The resistance of the wiring and the motor controller impose an additional resistance to the resistance of the stator coils, all of which is summed in R_T. Therefore, R_T is usually not the value given by the manufacturer for the motor resistance, but a higher value. The mechanical power generated by the motor is represented by the torque T and the motor speed ω.

Manufacturers of electric motors specify the performance characteristics of their products in terms of motor constants. It is therefore desirable to develop a motor model in terms of these easily accessible constants. Two important motor constants result from the interaction of the coils of wire with their current flow and the magnetic field produced by the permanent magnets. The first is the motor back emf constant K_E, which relates the induced voltage to

the motor speed by

$$V = K_E\,\omega. \tag{3.4}$$

The torque produced by the motor can be divided into two main components: static and dynamic torque losses T_M and the external load-torque T_L. Dynamic torque losses for brushless DC motors are a combination of frictional and viscous losses as discussed before. For the electric motors, where frictional losses are expected to occur in the ball-bearings and viscous losses in the rotor-stator gap, it can be assumed that the frictional losses are constant over the operating range and that the viscous losses are proportional to the motor speed. The motor torque T can then be expressed as

$$T = T_L + T_M = T_L + (T_F + DF\,\omega), \tag{3.5}$$

where T_F is a constant value for the frictional losses and DF is the viscous damping constant. Values for T_F and DF in air are usually given by the manufacturer.

The second important motor constant is the motor torque constant K_T. The torque produced by a permanent-magnet DC motor is proportional to the armature current I and K_T is the constant of proportionality

$$I = \frac{T_L + T_M}{K_T}. \tag{3.6}$$

This simple formula is valid as the magnetic flux produced by a permanent-magnet is constant. It does not vary with the speed of the motor or the armature current.

In applications where the motor electrical time constant is significantly less than the mechanical time constant, the $L\frac{dI}{dt}$ term in Equation 3.3 can be neglected. This is usually the case in iron-core motors.

Incorporating Equations 3.6, 3.4 and 3.5 into the motor Equation 3.3, yields the motor Equation in terms of the characteristic motor constants

$$E = \frac{T_L + T_M}{K_T}\,R_T + K_E\,\omega. \tag{3.7}$$

Solving equation 3.7 for ω gives an expression for the dependence of the motor speed on the load-torque

$$\omega = (\frac{-R_T}{K_T\ K_E})\ T_L + (\frac{E}{K_E} - \frac{R_T}{K_T\ K_E}\ T_M). \tag{3.8}$$

Together with 3.6, Equation 3.8 defines the performance of the electric motor for a given load-torque, T_L.

These two equations show clearly the linear dependence of rotational speed and motor current on load-torque, whereas Equation 3.8 also indicates that the speed of the motor is a function of the applied voltage. The stall-torque, which is the torque at zero speed, is proportional to the applied voltage. The no-load speed is also proportional to the applied voltage.

The most commonly used curves to summarize motor performance are speed, current, power-out, and efficiency versus load-torque. Power-out is the product of speed and torque and is therefore a second order polynomial. Efficiency is the ratio of power-out to power-in

$$\eta = \frac{T\,\omega}{E\,I}. \tag{3.9}$$

Typical motor performance curves are shown in Figure 3-2. The efficiency at very low speed, which is equivalent to high load-torque, is low because high torque requires high current which causes large I^2R losses in the motor windings. At high speed the efficiency falls because the viscous drag begins to take a significant amount of drive power.

The performance of the thruster is governed by the characteristics of the electric motor, the gearbox, the fill-fluid, and the shaft-seal. To model the complete thruster, a form of the motor curves must be developed which takes into account the torque losses due to the different components. It can be assumed that torque losses within the thruster are dependent on load-torque or motor speed or both or constant. Nonlinear effects are assumed to be negligible. This assumption is verified in the dynamometer tests in Chapter 5 and it has been shown that if speed or torque dependent losses occur, they are linearly dependent. Therefore it is valid to write

$$T_M = T_{M\ const} + T_M(T_L) + T_M(\omega) = T_F + T_{LT}(T_L) + DF\,\omega, \tag{3.10}$$

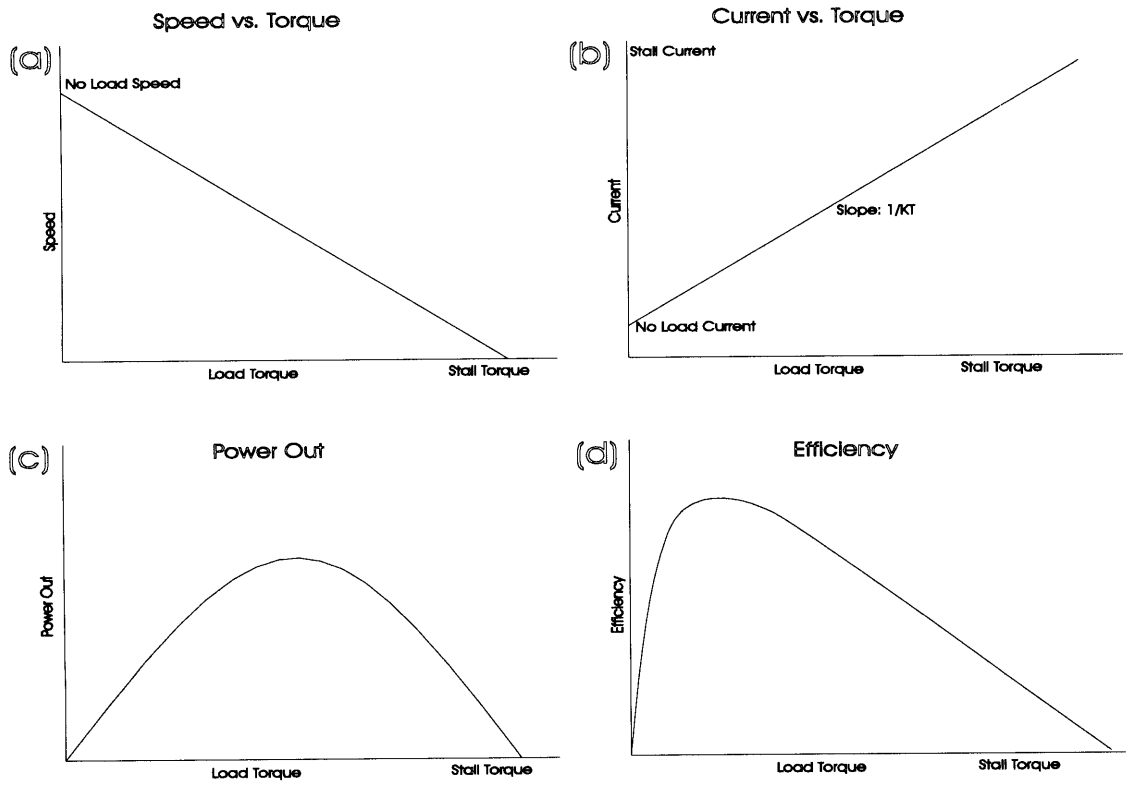

Figure 3-2: Motor Curves. Subplot (a) and (b) display the speed and current-versus-load-torque curves, which form the characteristic motor curves. Subplot (c) shows the power-out curve, which is the product of the motor speed and the load-torque. Subplot (d) shows the efficiency curve, which is the ratio of mechanical power-out and electrical power-in of the motor.

where T_F are constant losses, $T_{LT}(T_L)$ are load-torque dependent losses which will be assumed to be linear, and $DF\ \omega$ are linearly motor speed dependent losses, where DF is a viscous damping constant. As the motor is filled with oil, the model must account for the increased windage due to the higher viscosity of the oil compared to the viscosity of air. This is provided in the viscous damping constant, DF. Substituting Equation 3.8 into Equation 3.10 and solving for T_M yields an expression for the torque loss as a function of the load-torque. Substituting this result into Equations 3.6 and 3.8 yields the following expressions for I and ω as a function of the load-torque T_L and the applied voltage E,

$$I(T_L) = \frac{T_L\ K_E + [T_F + T_{LT}(T_L)]\ K_E + DF\ E}{DF\ R_T + K_T\ K_E} \tag{3.11}$$

and

$$\omega(T_L) = \frac{E\ K_T - T_L\ R_T - [T_F + T_{LT}(T_L)]\ R_T}{DF\ R_T + K_T\ K_E}. \tag{3.12}$$

Equation 3.11 and 3.12 are the basis of the motor model. All losses discussed below can be incorporated into these equations according to their dependence on load-torque or motor speed.

The Motor Controller

The motor controller is configured in torque mode. Given a DC input signal that indicates the desired torque level, the motor controller regulates the current flow to the stator windings with a Pulse Width Modulated (PWM) signal. The PWM signal chops the applied voltage to the level that drives the desired current level through the stator windings.

The motor torque is a linear function of motor current due to the properties of the two interacting magnetic fields. The rotor field is produced by permanent magnets and is therefore constant whereas the strength of the stator magnetic field is determined by the current flow through the windings. Thus the DC reference input signal determines the torque produced by the motor.

In the computational model it is assumed that the motor controller is fully opened (full duty cycle PWM signal) and that therefore the maximum possible current is flowing. Thus, the influence of the motor controller is reduced to an increased overall resistance, R_T.

Viscous Losses in the Motor

The windage caused in the motor by the viscosity of the fill-fluid is modeled using a Couette Flow [27] approach. Couette Flow is a solution of the Navier-Stokes equations in the special case of steady flow of a viscous fluid between two parallel walls, separated by a distance small compared to the horizontal dimensions of the walls. One wall is fixed while the other one moves with velocity U. The flow is assumed to be independent of the coordinates parallel to the walls and only dependent on the traverse y-coordinate.

This model is valid if the surface of the stator and rotor of the motor are smooth and the gap between stator and rotor is small compared to their length. This requirement is fulfilled for typical DC brushless motors. The equation describing the velocity profile u(y) over the height

h of the gap is given by

$$u(y) = \frac{1}{2\mu}\frac{dp}{dx}y(y-h) + \frac{U}{h}y, \tag{3.13}$$

where μ is the viscosity of the fluid, $\frac{dp}{dx}$ is a pressure gradient in the direction of the flow, which is in the case of the motor zero and U is the velocity of the moving wall, which is the rotor. The relationship between motor speed ω and U is given by

$$U = \omega\frac{d}{2}, \tag{3.14}$$

where d is the diameter of the rotor.

The resulting force on the non-moving wall, the stator, can be calculated using the stress relation in a Newtonian Fluid. The fundamental assumption of a Newtonian Fluid is that the stress tensor is a linear function of the velocity gradient. This is valid as a low-viscosity oil is usually used as thruster fill-fluid. As there is only one velocity gradient in a Couette Flow, the stress tensor simplifies to

$$\tau = \mu\frac{du}{dy}, \tag{3.15}$$

where μ in $[\frac{N}{m^2}s]$ is the viscous shear coefficient or simply the viscosity. The viscosity μ is just the kinematic viscosity υ times the density ρ of the fluid.

Integrating the shear stress exerted from the fluid on the rotor over the surface of the rotor yields the force F exerted on the rotor by the fluid

$$F = \frac{1}{2}\pi d^2 l\mu\frac{\omega}{h}. \tag{3.16}$$

This equation can be rewritten in terms of the rotor and stator diameter, D_1 and D_2, respectively. The loss of torque due to viscous losses in the motor can then finally be expressed as

$$T_{viscous}(\omega) = -\pi D_1^3 l\mu\frac{\omega}{-D_2 + D_1}, \tag{3.17}$$

or in terms of the damping constant DF

$$T_{viscous} = DF\,\omega \tag{3.18}$$

with

$$DF = \frac{-\pi D_1^3 l \mu}{-D_2 + D_1}. \tag{3.19}$$

Viscosity-Temperature Relationships The relationship between temperature and viscosity is discussed in [33]. Due to I^2R losses in the stator windings and due to mechanical losses, the motor temperature rises. Consequently, the temperature of the oil filling of the thruster increases by approximately the same amount as the winding temperature. The dynamic and kinematic viscosities of oils decrease with temperature. A good model for the viscosity variation of mineral oils and most synthetic fluids is provided by Walther's equation [35]

$$\mu(T) = A - B \log T, \tag{3.20}$$

where

$$B = \frac{\mu_1 - \mu_2}{\log T_1 - \log T_2}. \tag{3.21}$$

A and B are constants dependent on the oil type, where the constant B given by Equation 3.21 is the slope of a straight line in the $\log T$ and μ coordinate system. Equation 3.20 can be used for calculating the viscosity of liquids over a wide range of temperatures (from about -25 to 160 ^oC) provided two viscosities at different temperatures are known. The constant A can also be calculated from these both known points.

Equation 3.20 was tested with SAE oils of different dynamic viscosities for which the viscosities at different temperatures are known [14], The test revealed that a good fit can be achieved if the viscosities used represent the low and high end of the temperature range of interest. Otherwise, Equation 3.20 usually overestimates the decrease of viscosity over temperature, which can lead to significant errors at high temperatures.

Given the ultimate temperature rise of the motor due to power losses and knowing the viscosity of the fill-fluid at two different temperatures, it is possible to estimate the fill-fluid viscosity at the operating point.

Viscosity-Pressure Relationships The relationship between temperature and viscosity is discussed in [33]. The viscosity of oils also depends on the ambient pressure and increases with increasing pressure. The extend of change depends on the chemical composition of the

liquid as in the case described above. In technical practice, simple models are used, which ignore the nature and composition of the liquid. One of the most commonly used is due to Barus [3]. It predicts a linear relationship between viscosity and pressure and overestimates the effects of pressure for most oils. However, the viscosity-pressure effect is small compared to the viscosity-temperature effect and can therefore be neglected. For example, an increase in pressure of 25 bar (about 250 m water depth) causes the same increase in the viscosity as a drop of temperature of 1^oC.

Thermal Considerations

All power losses in the motor are dissipated as heat, which causes the motor temperature to rise. The major power losses are due to the current flow through the stator windings (IR^2 losses). The viscous and frictional torque losses in the motor, T_M, cause additional power losses. The power dissipation can be estimated using

$$P_d = I^2R + T_M\,\omega,$$

where R is the motor resistance given by the manufacturer (as only the power losses within the stator coils tend to heat it up) and not the overall resistance R_T. The ultimate temperature rise of the motor armature can be calculated using the thermal impedance. The thermal impedance TPR is a measure of the ultimate temperature rise per Watt of dissipated power, so the temperature increase ΔT is estimated by

$$\Delta T = P_d\,TPR. \tag{3.22}$$

The value for the thermal impedance given by the manufacturer is a 'worst case' value. This means that the value has been determined under worst operating conditions, e.g. motor at stall, in free air, and without heat sinking. Motor rotation, heat sinking, and the ambient seawater around the thruster will improve the heat transfer significantly and result in a much lower thermal impedance. This realistic thermal impedance can only be approximated and will depend strongly on the operating environment of the motor.

The motor resistance, torque constant, and back emf constant are functions of the motor

temperature. As the motor temperature increases, each of the three parameters will change in a manner which degrades the motor performance and increases the power losses. The actual resistance, torque constant, and back emf constant values for a given temperature change can be estimated using the empirical equations [31]

$$R_2 = R_1 \frac{234.5 + T_2}{234.5 + T_1}, \tag{3.23}$$

$$K_{T2} = K_{T1}(1 + C[T_2 - T_1]) \tag{3.24}$$

and

$$K_{E2} = K_{E1}(1 + C[T_2 - T_1]), \tag{3.25}$$

where C is a constant that depends on the type of motor and the type of permanent magnets employed. In the case of brushless motors with rare earth magnets, $C = -0.00025$.

The empirical estimates given by equations 3.22 through 3.25 are true for typical DC brushless motors in the power range of small underwater vehicles. To estimate the ultimate temperature rise and the changes in the motor constants for other motors, the model assumes that high-performance DC motors similar with properties are encountered.

For the thermal impedance this assumption holds as long as the magnitude of TPR is dependent on the motor geometry, the materials used, and the operating environment. It can be expected that electric motors in comparable power ranges have a similar geometry and consist of comparable materials and therefore will have comparable thermal properties.

The empirical formula estimating the change in motor resistance Equation 3.23 assumes a linear relationship between resistance and temperature and also assumes that copper wire is used in the windings.

The empirical formulas for calculating the torque and back emf constant Equations 3.24 and 3.25 are dependent on the parameter C. As discussed before, both motor constants are a result of the interaction of the coils of wire with their current flow and the magnetic field produced by the permanent magnets. Therefore, C takes different values for different permanent-magnet types and stator windings. For high performance brushless motors it can be expected that similar properties are encountered.

In conclusion, the calculation of the ultimate temperature rise of the motor and the calculation of the temperature influenced motor constants provides a reasonable estimate. Furthermore it allows investigation of the sensitivity of the system performance to different operating environments.

3.2.3 The Gearbox and the Seal

The gearbox converts the motor speed and torque to lower and higher levels, respectively. With this shift, torque losses are associated. To make the quantification of the torque losses in the gearbox analytically tractable, it is assumed that gearboxes are available in any speed-reduction ratio. Assuming that the gearbox is made up of arbitrarily small stages stacked together to achieve the desired speed reduction ratio, and that each of this stages has an efficiency η, the efficiency of the whole gearbox can be approximated by

$$\eta_G = G^{\kappa}, \tag{3.26}$$

where G is the desired speed reduction ratio and κ is a constant [8]. The underlying assumption in this model is that the efficiency of each arbitrarily small stage of the gearbox is the same. The overall gearbox efficiency is therefore only dependent on the speed reduction ratio G and a constant exponential scaling factor.

The coefficient κ has been determined by using efficiency values provided by a manufacturer [15] of planetary gearboxes in the torque and gearbox-reduction-range of interest for small underwater vehicles. The reported efficiencies were plotted against speed-reduction ratio and then approximated by determining the best fit for equation 3.26 by choosing κ. These were nine efficiency values over a speed-reduction range from 3.81:1 to 170:1. Equation 3.26 was fitted for the data using nonlinear regression. The discrete efficiency-data and the curve-fit are shown in Figure 3-3. The optimum value for κ was found to be

$$\kappa = -0.0385. \tag{3.27}$$

To incorporate the influence of the gearbox in the computational model, it is necessary to express its influence in terms of torque losses. If the gearbox were 100% efficient, the motor

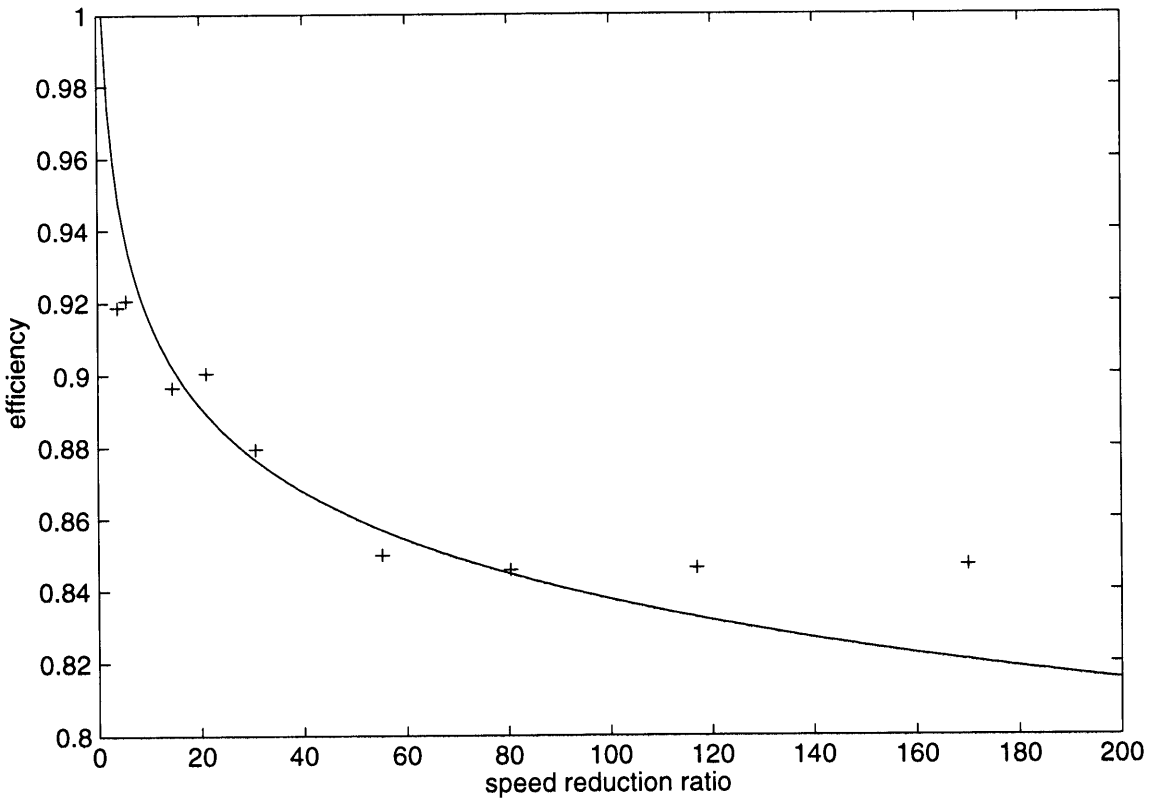

Figure 3-3: Gearbox Efficiency. Reported efficiency values for planetary gearboxes are plotted versus the gear-reduction-ratio and interpolated by a continuous function to estimate the gearbox-efficiency at any reduction-ratio.

torque T_m would be shifted without any losses, by the amount of the speed reduction ratio G to the gearbox shaft torque T_s

$$T_{s\,ideal} = G\,T_m. \tag{3.28}$$

In reality, the torque delivered at the gearbox output shaft is reduced by the gearbox efficiency

$$T_s = (\eta_G\,G)\,T_m. \tag{3.29}$$

The torque loss due to the gearbox as a function of the output shaft-torque, T_s, can then be

expressed as the difference between the ideal and the real case

$$\Delta T_m = \frac{T_s}{G} - \frac{T_s}{\eta_G G}. \tag{3.30}$$

The gearbox shaft-torque is equal to the load-torque; therefore, the torque loss due to the gearbox is a function of the load-torque.

This approach in modelling the losses inherent to the gearbox does not take into account the effects fill-fluid in the gearbox. The fill-fluids employed are usually light oils, whose presence will have an positive effect through increased lubrication and an negative effect through viscous losses. Both effects are assumed to be small and will be neglected.

In the dynamometer tests described in Chapter 4 it was found that the shaft-seal causes a constant torque loss, independent of the load-torque or the motor speed. The experimentally obtained torque loss is 1.2 Ncm. This value is used in the computational model to simulate the shaft-seal. Different kinds of shaft seals will cause different amounts of torque loss. However, the experimentally obtained value gives the best estimate of the loss associated with the shaft-seal.

3.3 The Program

The models of each component of the thruster discussed above have been combined in a MATLAB [24] program to simulate the performance of the thruster. Not included in this model are the effects of lubrication due to the oil filling, nonlinear effects and effects of the motor controller other than an increase in resistance. The user can specify which components of the thruster are to be simulated. Assuming that a motor is always part of it, the user can independently add the seal, a fill-fluid (by specifying its viscosity at two different temperatures), and a gearbox or combinations of the previous.

The parameters that need to be specified are summarized in Table 3.1 . Parameters that are usually provided in the specifications of the manufacturer of the electric motor are marked with an asterix. The remaining parameters are either prescribed by the application (e.g. applied voltage and ambient temperature) or can be obtained from the specifications of the manufacturer (e.g. the speed reduction ratio of the gearbox or the viscosity of the fill-fluid). The diameter of the rotor and stator can be obtained by opening up the motor and measuring the

Parameter	Units	Description
E	V	applied Voltage
R	ohms	stator resistance *
R_T	ohms	overall resistance, including wiring and controller
K_T	$\frac{N\,m}{A}$	torque constant *
K_E	$\frac{V}{rad/s}$	back emf constant *
T_F	N m	motor friction torque *
T_L	N cm	load-torque range, in terms motor shaft torque
T	^oC	ambient temperature
T_{max}	^oC	max winding temperature *
TPR	$\frac{^oC}{W}$	thermal impedance *
D_1	mm	rotor diameter
D_2	mm	stator diameter
L	mm	length of rotor/stator
G	-	gearbox speed reduction ratio
T_1, T_2	^oC	temperature of known viscosity of fill-fluid
μ_1, μ_2	$\frac{N\,s}{m^2}$	viscosity of fill-fluid at two temperatures

Table 3.1: Required Thruster Parameters

diameters. The thermal impedance has to be estimated based on the worst case value provided by the manufacturer. All variables are defined within the MATLAB script file and can be changed by editing this file. A program listing can be found in the Appendix.

The program is divided into three parts. In the first part the variables are introduced. In the second part the thruster performance calculations are conducted. The results are then written to a file and displayed in the third part of the program.

The computation is divided into two stages. In the first stage, the characteristic motor curves (with all included losses) are calculated for each operating point. The independent variable in all calculations is the load-torque. The basis for these calculation are Equations 3.11 and 3.12, which incorporate the losses that depend on the load-torque and speed. The viscous losses in the gap between rotor and stator are described by Equations 3.18 and 3.20. Equation 3.26 estimates the efficiency of the gearbox, whereas the estimation of the torque loss associated with the shaft-seal is based on an experimentally obtained value. Having calculated the modeled losses, the ultimate temperature rise can be estimated for each operating point using equation 3.22. Due to this change in temperature for steady state operation of the motor, the viscosity of the fill-fluid changes, which in turn changes the viscous losses. Therefore, the first stage of

the program is enclosed in a loop, which iterates between viscous losses, temperature change and fill-fluid viscosity until convergence is achieved.

Two plots are generated from the data obtained in the first stage. The first one shows the viscosity of the fill-fluid and the actual temperature for each iteration. This provides the possibility to check if the loop converges and if reasonable values are calculated. The second plot shows the viscous and frictional losses, the electrical I^2R losses, the ultimate temperature rise due to electrical and torque losses as well as the ultimate winding temperature. All plots are shown versus load-torque where the maximum torque is chosen to be the torque for which the maximum winding temperature is exceeded.

In the second stage, the altered motor constants for each steady state operating point (Equation 3.23 to 3.25), and its inherent temperature rise, are estimated and the resulting motor performance curves are calculated. The results of these calculations are shown in a third plot, compared to the characteristic motor curves obtained in stage one, which did not include the influence of the altered motor constants. The plot includes the current, speed, power-in and power-out as well as the efficiency versus load-torque curves.

3.4 Sample Run

This section shows the results of a sample run of the computational model. The thruster being simulated is the Odyssey II thruster employing a 5.54:1 gearbox manufactured by Globe Motors [15], a Crane shaft-seal, and Enduro Oil [28] as the fill-fluid. The motor is a Pittman Model 5113 DC brushless motor [29]. The thermal impedance is estimated to be 1 $\frac{^oC}{W}$. The ambient temperature is chosen to be 3 ^oC, which is characteristic of a deep ocean environment.

The viscosities of the Enduro Oil have been determined by the specifications of the manufacturer, by an experiment, and by extrapolation. The kinematic viscosity at a temperature of 40^oC is given by the manufacturer as 2 cSt. The density of the oil, which is needed for calculating the dynamic viscosity, was determined using a precise balance and a container of known volume. The obtained value is 784 $\frac{kg}{m^3}$. From these both values, the dynamic viscosity of the oil could be calculated for a temperature of 40^oC. The viscosity of the Enduro Oil at a temperature of 26^oC was estimated by assuming the same slope of the viscosity versus temper-

Parameter	Value	Description
E	48 V	applied Voltage
R	2.33 ohms	stator resistance
R_T	3.75 ohms	overall resistance, including wiring and controller
K_T	0.12 $\frac{N\,m}{A}$	torque constant
K_E	0.12 $\frac{V}{rad/s}$	back emf constant
T_F	4 10^{-3} N m	motor friction torque
T_L	0-200 N cm	load-torque range, in terms motor shaft torque
T	3 ^oC	ambient temperature
T_{max}	155 ^oC	max winding temperature
TPR	1 $\frac{^oC}{W}$	thermal impedance
D_1	30.4292 mm	rotor diameter
D_1	31.1658 mm	stator diameter
L	62 mm	length of rotor/stator
G	5.54	gearbox speed reduction ratio
T_1, T_2	40, 26 ^oC	temperature of known viscosity of fill-fluid
μ_1, μ_2	15.69, 24.84 10^{-4} $\frac{N\,s}{m^2}$	viscosity of fill-fluid at two temperatures

Table 3.2: Thruster Parameters Sample Run

ature curve in the logT coordinate system for the Enduro Oil as for a light motor oil (SAE10) for which the slope is known.

The overall resistance R_T, including the wiring and the motor controller, is hardly measurable and has been estimated by closing the power balance between power losses, power-out and the power input described in Chapter 4. This resistance value also lead to a good curve fit between experimental results and the computational model as described in Chapter 5. The input parameters are summarized in Table 3.2.

The results of running the program with the parameters specified above are now presented and discussed. Figure 3-4 shows the convergence check plot used to control the convergence of the first loop. From Figure 3-4 (a) it can be seen that the viscosity of the fill-fluid converges rapidly, from an initial value of about $5 * 10^{-3}$ $\frac{N\,s}{m^2}$ in the first loop (where the thruster is not heated up yet) to a significantly lower value for each steady-state operating point. For the high end of the load-torque range shown it can be seen that the fill-fluid viscosity would intersect the x-axis and negative viscosity values would be encountered. This is prevented in the program by specifying a minimum viscosity value. If the estimated fill-fluid viscosity drops below the viscosity of air, it is set to a value which is equivalent to the viscosity of air. The failure of the

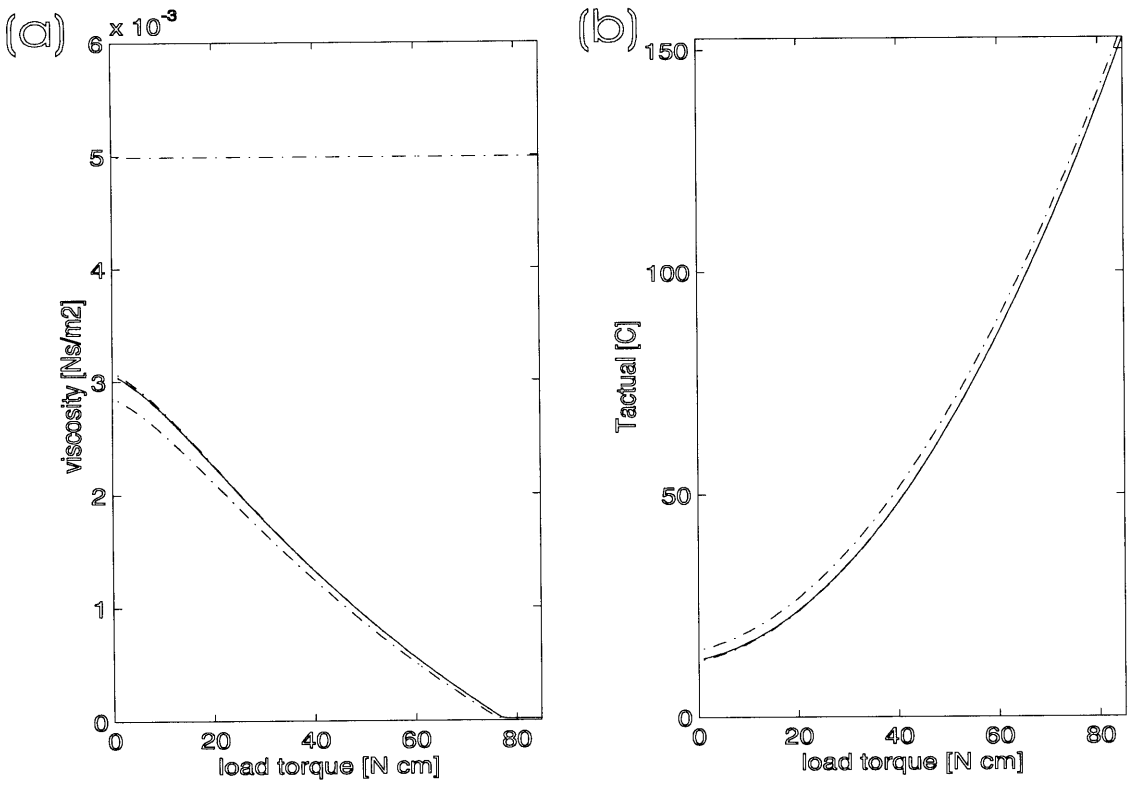

Figure 3-4: Convergence Check. Plot (a) shows the convergence of the fill-fluid viscosity from an initial value of about $5 * 10^{-3}$ $\frac{N\,s}{m^2}$ for the thruster at room temperature to a lower viscosity at steady-state operation due to an increase in temperature caused by the modeled losses. Plot (b) shows the convergence of the actual winding temperature to a steady-state value.

extrapolation of the viscosity values for high temperatures is due to the quality of the curve fit discussed before.

Figure 3-4 (b), showing the actual winding temperature, supports the behavior described above. It can be seen that the higher the load-torque, the more significant the I^2R losses are, which heat up the motor and lead to the parabolic dependence of the temperature on load-torque. The maximum possible load-torque is 85 N cm as the maximum winding temperature of 155 ^oC is exceeded for higher load torques.

Figure 3-5 (a) and (b) shows the viscous and frictional losses as well as the electrical power losses. The viscous and frictional losses are the sum of the losses due to the fill-fluid, the gearbox and the shaft-seal. Figure 3-5 (c) shows the ultimate temperature rise due to viscous and

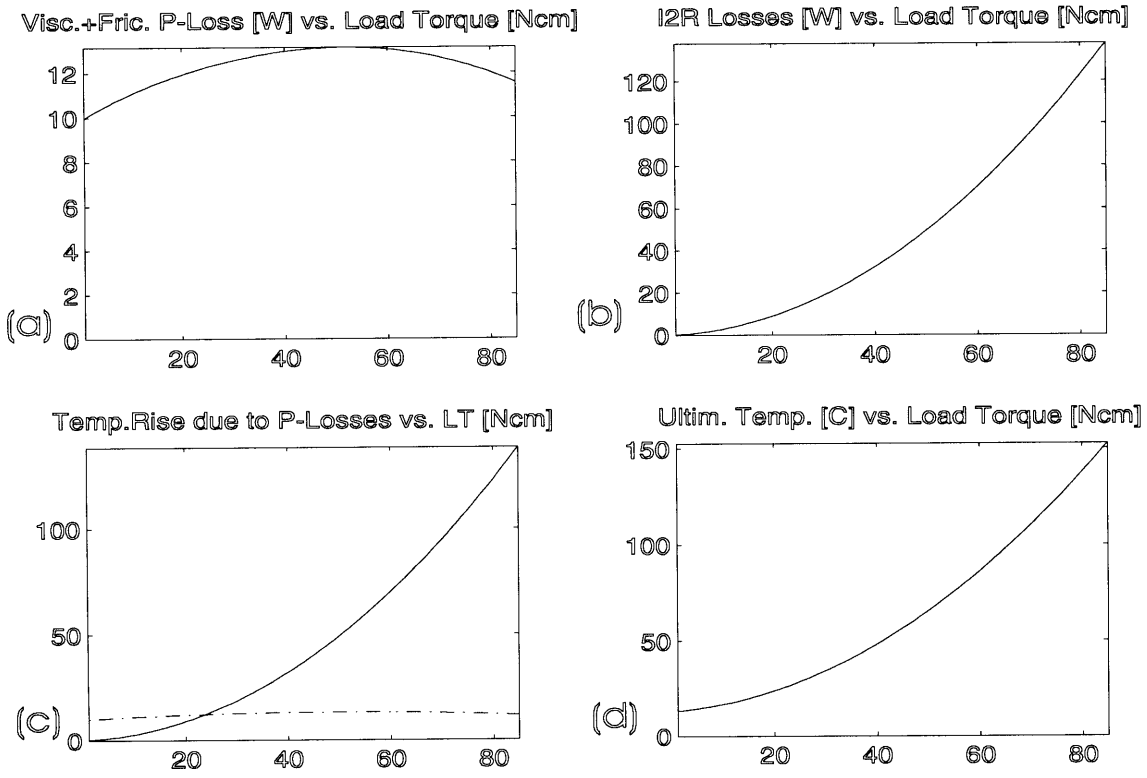

Figure 3-5: Losses and Ultimate Temperature Rise. Plot (a) and (b) show the magnitude of the viscous, frictional and electrical losses. Plot (c) shows the ultimate temperature rise due to viscous and frictional power losses (dotted-dashed line) and the ultimate temperature rise due to electrical losses (solid line). Plot (c) shows the steady-state winding-temperature.

frictional power losses (dotted-dashed line) and the ultimate temperature rise due to electrical I^2R losses (solid line). Figure 3-5 (d) shows the actual steady-state winding-temperature in the operating environment.

Figure 3-6 finally shows the motor curves. The solid curves are the results of the calculations performed in the first loop, which do not yet include the influence of temperature on the motor constants. The dotted-dashed motor-performance curves are calculated using the motor constants altered according to the temperature change at each steady state operating point. It is clearly seen that an increase in motor temperature degrades its performance. The model predicts a peak efficiency of the thruster of 71%. The maximum continuous power-out is 117 Watts.

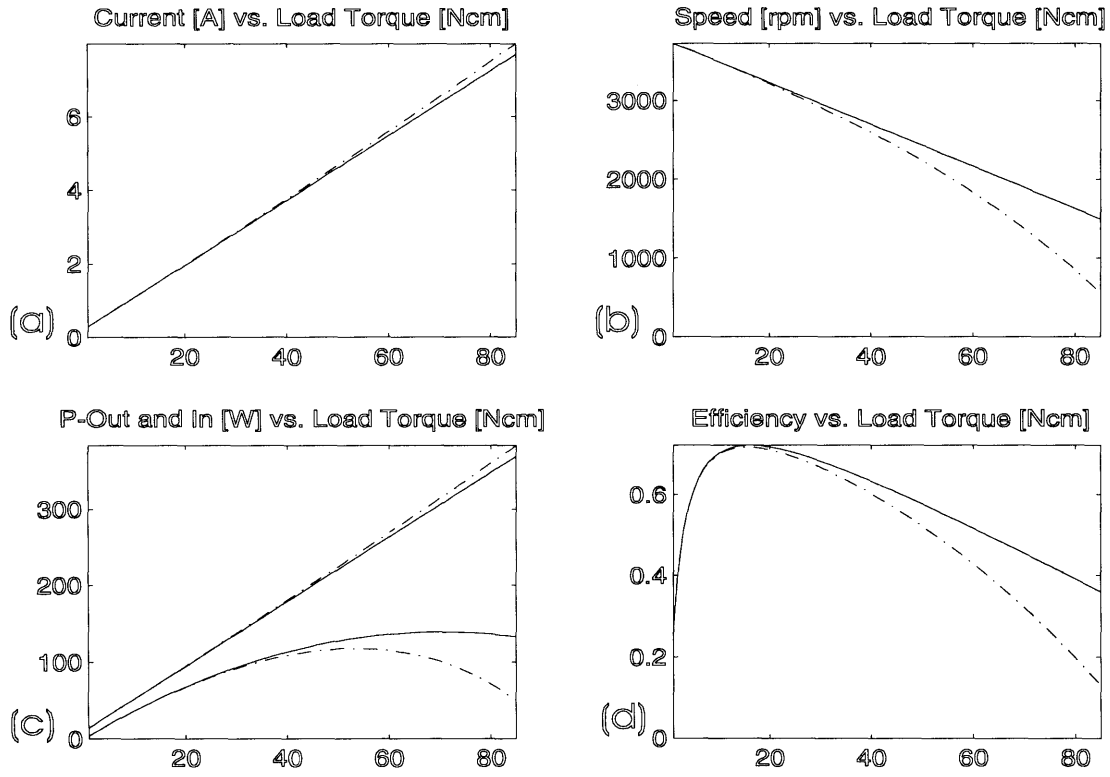

Figure 3-6: Motor Curves. Plots (a), (b), (c) and (d) show the motor curves, where the solid lines do not include thermal effects. The dotted-dashed lines represent the steady-state motor curves, including thermal effects.

Figure 3-7 presents steady-state efficiency curves for different thruster parameters. The base line for this comparison is the thruster modeled above, which is represented in Figure 3-7 by a solid black line. Single parameters have been changed to show their impact on the whole thruster performance. In particular:

- The ambient temperature has been increased form 3 to 25 ^oC. The effect is a slightly improved efficiency in the low-load-torque range (which is equivalent to high rotational speed) due to the decreased viscosity of the fill-fluid.
- The fill-fluid has been changed from oil to air. The effect is a significantly improved efficiency in the low load-torque range due to the reduced viscous losses.
- The gear-ratio has been increased from 5.54 to 20. The effect is a significant loss in

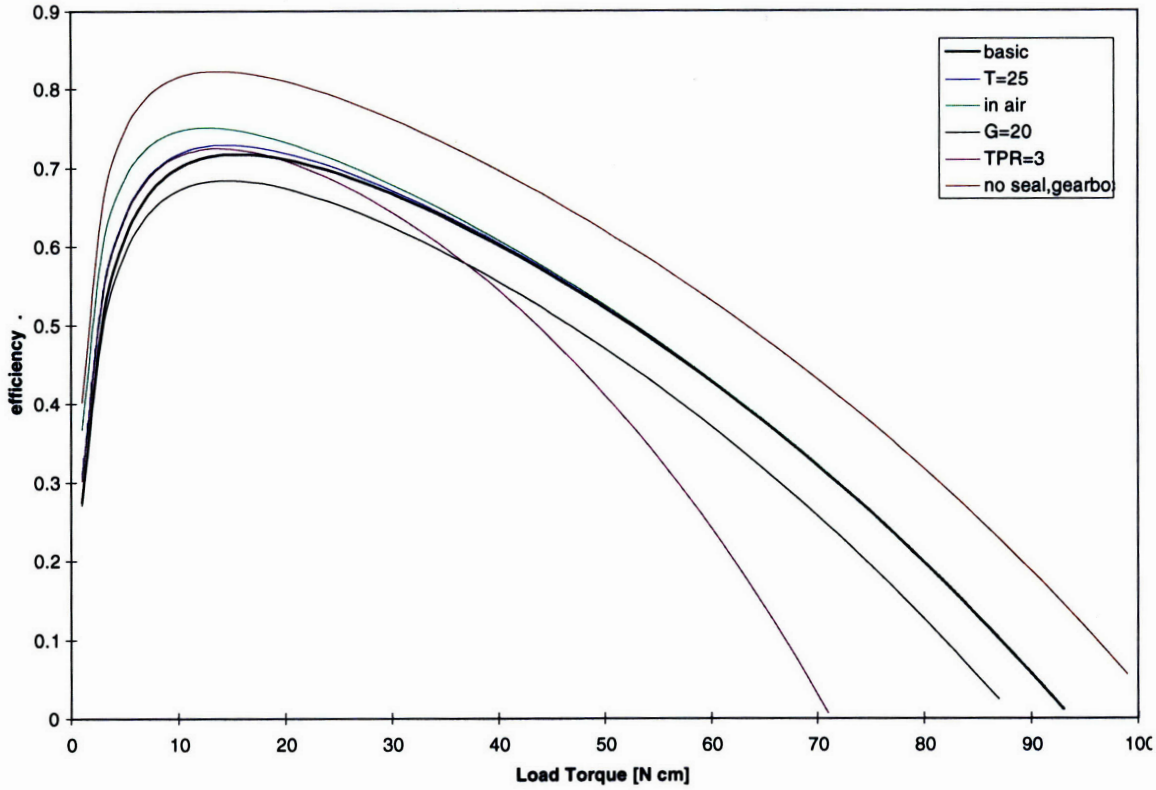

Figure 3-7: Efficiency Curves for Different Thruster Parameters. The impact of changing thruster parameters such as the ambient temperature, the fill-fluid, the gear-ratio, the thermal impedance and the gearbox/seal presence is shown by plotting the altered efficiency curves together with the efficiency curve generated by using the original Odyssey II thruster configuration and parameters (thick black line labeled 'basic').

efficiency for increasing load-torque.

- The thermal impedance has been increased from 1 to 3 $\frac{^{\circ}C}{W}$ (3 is the 'worst-case-value' given by the manufacturer, whereas 1 is an estimated value for the increased heat dissipation for an oil-filled thruster in a low-temperature environment) to assess the effect of worsened heat-dissipation. Due to the increased heating up of the thruster, the performance at low load-torque improves as the fill-fluid viscosity decreases, whereas the worsened heat dissipation degrades the motor performance for higher load torques.

- The seal and the gearbox have been removed. The effect is a major improvement in the thruster performance of about 8% over the whole torque range.

The validity of the computational model will be proved in Chapter 5, using the results of the dynamometer tests from Chapter 4.

Chapter 4

Dynamometer Tests

4.1 Introduction

To develop an improved understanding of the efficiency issues influencing the performance of the Odyssey II thruster and to verify the computational model presented in the previous chapter, the Odyssey II thruster has been tested using a dynamometer. A dynamometer is an apparatus capable of simultaneously measuring shaft torque and speed of a rotating machine. By measuring these quantities, power-out of the machine can be calculated.

Although the characteristics of each component of the propulsion system are well known, the influence of their interactions on the overall performance is not. Effects such as viscous losses in the gearbox and lubrication effects are not captured in the computational model and may lead to deviations between the model and the experiments. Furthermore, the effect of varying the position of the Hall-effect sensors can only be investigated experimentally.

The following tests reveal the influence of each component of the thruster on the overall efficiency of the system.

4.2 Theory

The objectives of the dynamometer tests are to measure the performance of the thruster in different configurations, allowing the characterization of the influence of the different thruster

components on the overall efficiency. Efficiency is defined as the ratio of power-out to power-in

$$\eta = \frac{P_{out}}{P_{in}} = \frac{\omega\, T}{E\, I}. \tag{4.1}$$

The four quantities on the right hand side of Equation 4.1 need to be measured to characterize the performance of the thruster.

4.3 Apparatus

4.3.1 The Odyssey II Thruster

The Odyssey II thruster consists of a motor-gearbox combination enclosed in an oil-filled housing as described before (Figure 1-2). The motor is a Pittman Model 5113 DC brushless motor [29]. This motor employs a permanent-magnet, smooth-surfaced rotor with the windings located on the stator.

Both the motor and the gearbox have been customized to fit into the thruster housing. The housing is a cylindrical body with a diameter of approximately 57 mm and a length of approximately 250 mm. The fluid used for compensation is Enduro oil, a mineral oil, which has proved not to interfere with the electronics. A Crane shaft-seal is located in one end-cap of the thruster housing.

The motor is controlled by a Copley Controls Corp. model 513 motor controller. The motor is controlled in torque mode, which allows it to generate a constant torque determined by a DC reference signal. The controller uses a Pulse Width Modulated (PWM) signal to regulate the energy flow to the motor. The gearbox is manufactured by Globe Motors and uses a planetary gearwheel arrangement to achieve a speed-reduction ratio of 5.54:1. The maximum continuous operating torque is 11.3 Nm.

4.3.2 The Experimental Setup

The experimental setup consisted of the thruster unit driven by the motor controller, a dynamometer connected to a readout instrument, two power supplies, two logical probes and an oscilloscope. An overview over the experimental setup and the test equipment is shown in

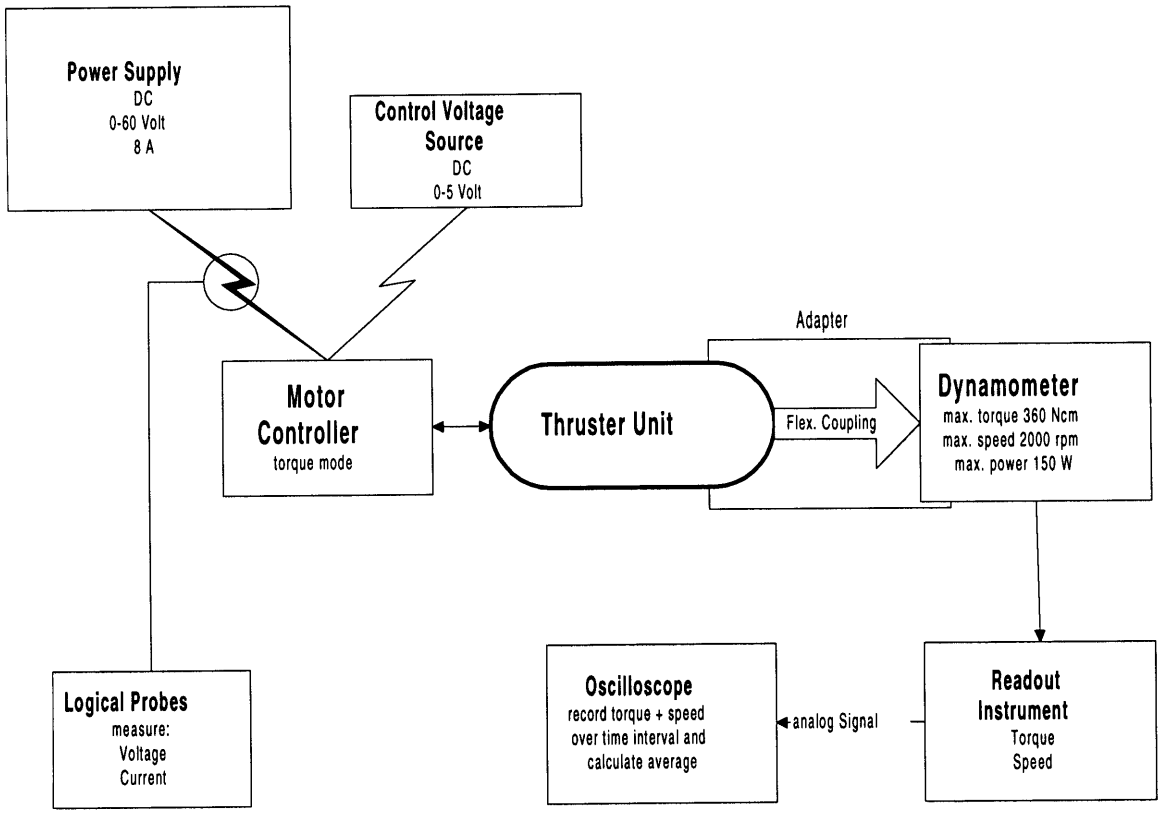

Figure 4-1: Experimental Setup.

Figure 4-1.

The thruster housing and the dynamometer were connected by an adapter which provided a stiff connection between these units. To minimize the effects of misalignment, the thruster shaft and the dynamometer shaft were linked using a flexible coupling.

The dynamometer uses a torque transducer, a speed transducer and a dynamic torque-spindle mounted to a shaft supported by two ball-bearings as shown in Figure 4-2. The torque transducer consists of a bearing-mounted torsion-bar with a maximum torque rating of 360 Ncm and an overload capacity of +/- 100%. The speed transducer is a low-inertia, DC tachometer. The dynamic torque-spindle employs a magnetic-particle brake to produce the load torque. The limits of this torque spindle are reached by either exceeding the maximum torque of 360 Ncm, the maximum speed of 2000 rpm or the maximum continuous power of 150 watts.

A readout instrument, connected to the dynamometer, displays the measured torque and

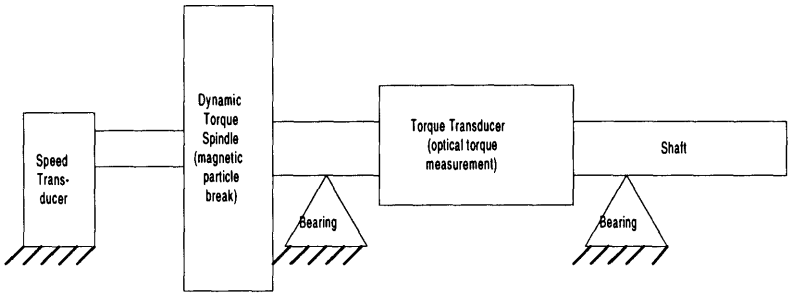

Figure 4-2: Dynamometer.

speed. The torque display is zeroed using a potentiometer. Readout options include a 'hold' function, which latches the torque and speed readout, as well as a 'peak' function which records the maximum torque and speed values over a time interval. The torque-control option permits discrete adjustment of the load torque or allows the torque to be ramped up from zero to stall torque at an adjustable rate. Two analog outputs on the readout instrument allow torque and speed readouts to be read using an oscilloscope. The oscilloscope was used to record the torque and speed signal over a time interval and calculated the averages.

Two power sources were used, both connected to the motor controller. One operates as a power supply, the other one as a reference signal source. The voltage of the power supply is adjustable from 0 to 60 volts and limited by a maximum current capability of 8 amperes. The reference signal is adjustable from 0 to 10 volts.

Two multimeters (Tektronix Multimeters Model 252) were used to measure the voltage and current between the power supply and the motor controller; therefore the motor controller is included in the system evaluation. The multimeter used for current measurements is capable of recording the current reading over a time interval and calculating the average. Both probes offer a 'hold' function which allows them to freeze the current reading.

All instruments were placed on a stable workbench free from vibrations and operated at an ambient temperature of approximately 22.5 ^{o}C. The cable connections between the test equipment, especially the connection from the power supply to the motor controller, were sized for the applied power.

Component	Accuracy
Torque Transducer	+/- 1% of span, 3.6 Ncm (includes ripple, linearity hysteresis, and calibration)
Speed Transducer	+/- 0.5 % of span, 10 rpm
Torque Display	+/- 0.25% of span +/- one digit
Speed Display	+/- 0.25% of span +/- one digit
Torque Analog Output	+/- 0.2% of span, 0.72 Ncm
Speed Analog Output	+/- 0.1% of span, 2 rpm

Table 4.1: Dynamometer Accuracy Specifications

4.3.3 Potential Error Sources

The dynamometer employs an optical shaft torque measurement system. Errors in this system may arise from changes in the shear modulus of the test section and dimensional deviations in diameter and gage length caused by temperature changes. Furthermore, errors may arise from non-linearities in the deflection and in the instrument system. Spurious signals may be caused by faulty installation or by stray electric currents. Other error sources include bearing friction, calibration arm length error, calibration weight error, errors in measurement of rotational speed, misalignment forces and vibrations. The accuracies assumable according to the dynamometer manufacturer are summarized in Table 4.1.

The manufacturer's specifications for the multimeters specify an accuracy in measuring DC voltage +/- 0.1% over a range from 4 to 1000 volts. The accuracy in measuring current is specified to be +/- 0.8% for up to 10 amperes.

The voltage drop over the probe measuring the current was found to be 0.3 volts at a maximum current of 8 amperes. This equals a probe resistance of 0.0375 ohms. As the voltage is measured directly at the power supply, the applied voltage to the motor is different from the measured voltage due to the probe resistance. The error in % can be expressed as

$$\varepsilon = \frac{I\,\Omega}{E}\,100\,\%,$$

where I is the measured current, E the measured voltage and Ω the probe resistance. For example, at a voltage of 40 volts and a current of 8 amperes, the voltage error would be 0.75%. The effect of this error was found to have a very small effect on the evaluation of the experimental results and has therefore been neglected.

The errors resulting from the oscilloscope, the averaged fluctuations of torque, speed and current readout, and minor influences like the flexible coupling, are not quantified. Furthermore the effects of the motor controller on the test results are not known and not easily quantifiable. Non-linear behavior might affect results in a non-systematic manner. Nevertheless, the component accuracies discussed above are worst case values and it can be assumed that they overestimate the actual experimental error.

4.4 Techniques

4.4.1 Calibration

The calibration of the torque transducer has been checked using a static calibration procedure recommended by the manufacturer. In-situ calibration is not feasible due to its complexity and would be more inaccurate than a static calibration.

A wooden calibration beam was attached to the torque transducer input shaft in a horizontal position while locking the output shaft. By placing a known weight on the calibration beam at a prescribed distance from the shaft axis, a torque load resulted. This torque load is the product of the distance of the weight from the shaft axis and the weight times gravity.

By incrementally varying the weight up to the maximum torque capability of the torque transducer and recording the resulting torque readouts, a calibration-curve was obtained. These measurements were compared to the calculated torque and deviated for all data-points less than 1% from the calculated torque values.

The speed-transducer readout was checked by comparing the speed calculated from the period of the Hall-effect sensor signal to the speed readout. The oscilloscope was connected to one of the three Hall-effect sensor connections between motor and motor controller. The period of the resulting square wave signal was measured using the oscilloscope. As the magnet used to sense the motor position has two north and two south poles, one revolution of the shaft produces two peaks. Knowing this and the period of the signal, the shaft speed in revolutions per minute could be calculated. Spinning the motor at a slight load torque over the rpm range of the dynamometer (0 to 2000 rpm) and comparing the speed readout to the speed measured by the oscilloscope revealed that the speed readout was accurate within 1% over the speed

Test	motor	gearbox	oil	seal	Remarks	Motivation	Voltage
1	+	-	-	-	room temp	motor efficiency	24 to 40 volts
2	+	-	-	+	room temp	influence of seal	24 to 40 volts
3	+	-	+	+	Enduro Oil room temp	influence of oil-filling without gearbox	24 to 48 volts
4	+	+	+	+	Enduro Oil room temp	influence of gearbox with oil-filling	24 to 52 volts
5	+	+	-	-	room temp	influence of gearbox without oil-filling	24 to 40 volts
6	+	+	+	+	temp. 3 °C	temperature effects	40 volts
7	+	+	+	+	Carnation Oil room temp	viscosity effects	40 volts
8	+	+	+	+	Carnation Oil + Additive	viscosity and lubrication effects	40 volts
9	+	+	-	-	vary pos. of Hall-effect sens.	effect of Hall-effect sensor position	30 and 40 volts

Table 4.2: Tested Thruster Configurations

range.

The multimeters used for measuring voltage and current were compared with other similar multimeters to determine the range of possible readout fluctuations. The displayed digits coincided and no deviations were found.

4.4.2 Scope of the Tests

To determine the influence of the different components of the thruster, tests in different configurations were conducted. These different configurations were obtained by adding or removing components from the thruster. Furthermore, the influence of low temperature encountered in the deep ocean, different thruster fill-fluids and the position of the Hall-effect sensors were investigated. The tested assemblies are summarized in Table 4.2.

4.4.3 Experimental Procedures

The experimental procedure used during the tests evolved from several trial-and-error approaches used to find a procedure which gave accurate and repeatable results. After the dy-

namometer has been turned on and warmed up for about an hour, the torque readout was adjusted to zero. The zero adjustment was always carried out with the dynamometer shaft in the same position.

After adjusting the power supply to the desired voltage, the motor was turned on by ramping up the reference input signal to the motor controller to 5 volts. The torque load was then ramped up to the maximum possible load using the adjustment potentiometer of the dynamometer. The maximum load was prescribed by the maximum torque or power capability of the dynamometer, or by reaching the stall torque of the motor. Once the load torque was applied the motor quickly reached steady state. Nevertheless, fluctuations around an average in the instrument readouts dependent on load torque and motor speed could be seen. Particularly at low load-torque and high motor speed fluctuations could be observed.

Measurements were logged over four seconds using the oscilloscope (torque and speed) and a multimeter measuring current. After the measurement period was complete the time average of the recorded data was displayed and logged manually in a spreadsheet program. The spreadsheet calculated power-in, power-out and efficiency. This allowed a check on the quality of the obtained data and provided a warning if the maximum power capability of the dynamometer was approached.

While keeping the voltage constant, measurements were taken in steps going from high to zero load-torque. After each measurement the motor was turned off and allowed to cool so that the data were uninfluenced by temperature effects. At high torque and low rotational-speed the thruster heated significantly. To increase cooling in these cases, ice packs were attached to the thruster. However, the attempt to take all measurements at room temperature might not have been always successful, particularly for high load torque, as the thruster had time to heat up in the time period from turning the thruster on up to taking the measurement, which amounted to about 6 to 10 seconds.

Through test series 1 to 5 (Table 4.2) one component after the another was added to the thruster to determine their influence. For each configuration, tests were performed over a range of voltages. The tests started at 24 volts and the voltage was increased in steps of 4 volts. The maximum voltage for the tests was determined by the torque, speed and current capabilities of the test equipment. Between each test series the torque readout of the dynamometer was

readjusted to zero following the procedure described above.

During the second test, which was meant to investigate the influence of the shaft-seal, the thruster and the dynamometer were placed vertically. As the unit was not oil-filled for this test, a sufficient lubrication of the shaft-seal had to be assured in order to obtain realistic results. Initial tests showed that a non-lubricated shaft-seal produced significantly higher friction than a lubricated shaft-seal. By placing the shaft-seal as the lowest part of the unit and filling the housing with some oil, a sufficient lubrication could be assured. The changed position of the dynamometer had no effect on the measurements as was demonstrated by repeating the first test in both positions and obtaining similar results.

To determine the effect of low temperature, present in deep ocean applications, on the thruster performance the unit has been cooled down in a refrigerator to 3 ^{o}C for about three hours. Afterwards the unit was mounted as quickly as possible to the dynamometer and surrounded by ice-packs. To maximize the surface contact area between the thruster and ice-packs, flexible plastic bags filled with a water-salt solution, cooled down to -1 ^{o}C, were used. Starting this time at low load-torque to prevent the motor from heating up quickly, measurements were taken over increasing load torque. As this procedure differs from the one used before, starting at high load-torque, a reference test was conducted utilizing the same procedure at room temperature. This allowed the determination of low temperature effects independent of test procedure influences.

The purpose of test seven and eight were to determine the effects of viscosity of the filling fluid and of lubrication. First the Enduro oil was drained completely. The thruster was then flushed thoroughly with alcohol, filled with new oil and flushed again while the motor was spinning. Finally the oil was drained entirely and the unit refilled with the new oil. Data was obtained as described above.

The last test series, number nine, investigated the influence of the position of the Hall-effect sensors. The end-cap of the thruster was removed, revealing the Hall-effect sensors which are fixed onto a plastic disc rotatable within 40^{o}. While spinning the thruster under a constant torque load, the position of the Hall-effect sensors was varied by rotating the plastic disc in increments of about 6^{o} to 7^{o}. The resulting speed readout varied, resulting in a different efficiency for each Hall-effect senor position.

4.4.4 Data Processing and Evaluation

The performance of the thruster is completely determined by measuring the speed-versus-load-torque and motor current-versus-load-torque curves. As these curves are linear for all tests, a linear least-squares curve fit was put through the logged data-points and the resulting continuous linear functions were used to calculate power-in, power-out and efficiency. Therefore, the displayed power-out and efficiency versus load torque curves in the following sections are continuous functions and show no discrete data points. The least squares interpolation of the gathered data has two effects. First, the random experimental error is reduced and the motor curves are smoothed. The experimental error and the quality of the least square curve fits are discussed in the next section. Second, the resulting continuous functions make it possible to compare tests to each other which would not be possible otherwise as data was not always taken at exactly the same load torque for each test. Therefore, the continuous least square curve fits were used for all calculations and evaluations in the following.

As described above, one component of the thruster after the other was added to determine its influence. It can be expected that the torque losses, T_M, increase with each added component. Comparing the resulting characteristic motor curves with the ones from the test without the component in question, allows to draw quantitative and qualitative conclusions regarding the influence of the added component on the thruster performance. For example, comparing the characteristic motor curves for the test case, motor+seal at 48 volts, to the test case, motor+seal+oil at 48 volts, reveals the influence of the added oil.

To develop an understanding of how to interpret the test results and how torque losses will affect the motor performance and consequently the characteristic motor curves, the theoretical representation of the characteristic motor curves introduced in Chapter 3 is examined below.

By solving Equation 3.6 and 3.8 for the torque loss T_M, two expressions for the torque loss are obtained. The increase in torque loss due to the added component can be calculated by comparing the characteristic motor curves for the both cases, evaluated at the same load torque. For the current-torque relationship, Equation 3.6, and the speed-torque relationship, Equation 3.8, the following expressions are obtained

$$\Delta T_M = T_{M2} - T_{M1} = K_T\,(I_2 - I_1), \tag{4.2}$$

and

$$\Delta T_M = T_{M2} - T_{M1} = \frac{K_T\, K_E}{R_T}\,(\omega_1 - \omega_2). \tag{4.3}$$

The torque loss due to an added component can be obtained by comparing the current-versus-load-torque curves or the speed-versus-load-torque curves at the same load torque.

Using Equation 4.2, the increase in torque loss can be obtained by multiplying the difference in current at a prescribed load torque with the torque constant, K_T. The torque constant is the slope of the current-versus-load-torque curve and can be obtained from the manufacturer of the electric motor or from the first set of tests. The first test series is used as the base-line for all following tests as it tests only the motor to give the least-biased torque-constant, although internal motor losses like friction in the two ball-bearings and viscous losses in air are included.

The second case, Equation 4.3, is more involved as the back emf and the motor resistance need to be known in order to obtain the torque loss from the experimental results. These constants cannot be extracted easily from the gathered data. Nevertheless, the complete information needed to determine the torque loss due to the added component is contained in both characteristic motor curves.

It can be expected that Equation 4.2 applied to the evaluation of the test results gives good estimates for the torque loss as the underlying physical principle leading to Equation 3.6 is simple and well captured [18]. However, Equations 4.2 and 4.3 are expected to give the same results as can be proved by substituting equations 3.11 and 3.12 into equations 4.2 and 4.3, respectively

The power loss due to an added component can be calculated by multiplying the torque loss at a prescribed load torque with the speed at that load torque.

Having discussed how the torque and power loss due to an added component can be extracted from the experimentally obtained results, the alteration of the characteristic motor curves due to the increased torque losses is discussed below. This makes it possible to make suppositions about the dependence of the torque losses on motor speed or load torque.

The torque losses can depend on the load torque as well as on the motor speed. Equations 3.11 and 3.12 are solutions to the current and speed-versus-load-torque curves for the case of losses that are linear in speed and torque. In these equations, it is assumed that non-linear speed-dependent effects, for example non-linear terms in the viscous losses in the gearbox, are

negligible.

In the list below, different torque-loss cases are discussed and the resulting behavior of the speed and current-versus-load-torque curves (according to equations 3.11 and 3.12) is described. The curves for the ideal case, without any losses, are compared to a case with torque losses. The resulting curves show qualitatively how both are altered compared to the ideal case. That is, the curves show what happens when a component with a certain torque loss characteristic is added.

- *no speed-dependent losses, constant torque-dependent losses*; Both current-versus-load-torque curves are parallel, separated by a significant distance. The added torque loss causes a fixed increase in current current. The speed-versus-load-torque curves are also parallel, separated by a significant distance. The added torque-loss results in a constant reduction in speed.

- *no speed-dependent losses, linear torque-dependent losses;* The slope of both the current and speed-versus-load-torque curves is significantly increased. Starting at the same point for zero load torque, the current increases linearly with load torque while the achieved speed linearly decreases.

- *no speed-dependent losses, non-linear torque-dependent losses;* This kind of loss causes the current and speed-versus-load-torque curves to take non-linear shapes. As this kind of behavior was not observed in the tests, it is not of interest. From this, the conclusion can be drawn immediately that load-torque-dependent non-linear effects are negligible.

- *speed-dependent losses, no torque-dependent losses*; In this case, the current-versus-load-torque curve is significantly shifted to higher current, while its slope is slightly decreased. The speed-versus-load-torque curve is slightly shifted to lower speed, while its slope is significantly decreased.

- All combinations of the above cases are linear superpositions and can therefore be described by simply adding up the characteristics of the losses discussed above.

In summary, the way to extract torque and power losses due to an added component from the test results is to plot the linearly-interpolated continuous speed and current-versus-load-

torque curves for both cases in one graph. Entering the current-versus-load-torque graph at a certain load torque, taking the difference between the currents, and multiplying by the torque constant, reveals the torque loss due to the added component at this load torque. Multiplying the torque loss with the speed at the same load torque reveals the power loss due to the added component. Qualitative estimates of the dependence of the torque loss on speed or load torque can be made according to the analysis above.

In the following, the effect of the applied voltage on the characteristic motor curves is discussed briefly. By recalling equations 3.6 and 3.8, it can be seen that the current-versus-load-torque curve is not affected by the applied voltage, whereas the intersection of the speed-versus-load-torque curve with the y-axis (no-load speed) is a function of the applied voltage. For increasing voltage, the speed-versus-load-torque curve is expected to be shifted to higher speeds, or in other words, motor speed is dependent on the applied voltage.

The previous discussion was based on the theoretical motor model presented in Chapter 3, which can only approximate reality. Nevertheless, the governing physical characteristics are represented in the model. Analyzing the behavior of the model therefore improves the understanding and interpretation of the experimentally obtained data and makes it possible to make suppositions about the origin of observed trends and results.

In order to identify trends dependent on the applied voltage, the slopes and intersections (no-load speed and current) of the interpolated current and speed-versus-load-torque curves were plotted versus the test-series voltage-range. From these plots, variations in slope and intersections dependent on the applied voltage could be identified, which also reveals the influence of different components in two test series when compared.

Even though it would be possible to extrapolate the fitted, and therefore continuous current and speed-versus-load-torque curves to speed and torque regimes not measurable with the dynamometer, this has not been done as it cannot be verified that the curves remain linear. Nonlinear effects may not be negligible anymore particularly for high speed and torque. Consequently, the discussion of the results is restricted to regimes where experimental data has been gathered.

The discussion of each test series is structured in five headings. First, the *limitations* imposed by the test equipment upon the test range are described. Then a typical example of

characteristic motor curves for the set of tests in question is shown in comparison to a reference test. This allows the component influences to be determined and their behavior analyzed by invoking the theoretical model discussed above. The discrete data as well as the least square curve fit is plotted to show the quality of the fit. The slope and intersection comparison of the characteristic motor curves for the set of tests in question is presented along with the reference set of tests. The *trends* of the curves over the tested voltage range are identified. The comparisons between the set of tests in question and the reference set of tests clarifies and shows the consistency of trends observed in the example given in the second paragraph. The next paragraph displays and discusses examples of efficiency curves (*qualitative efficiency behavior*) for the set of tests in question, compared to the reference set of tests. Finally, *torque losses* due to an added component are quantified and summarized. Furthermore, the power losses due to the added component are quantified, including electrical losses (I^2R) due to the increase in current.

The resistance R, required to quantify I^2R losses, given by the manufacturer is not the real resistance encountered, as the resistance of the cabeling and the motor controller are included in the evaluation and add to the motor resistance. The real resistance cannot be measured easily and has therefore been obtained by closing the power balance, as discussed in the section 'Summary and Conclusions' at the end of this chapter, and independently by matching the theoretical model and the experimental results in Chapter 5. The value found in both cases is about

$$R_T = 3.75\ \Omega. \tag{4.4}$$

To quantify the torque losses due to an added component, the torque constant K_T needs to be known. The torque constant is the slope of the current-versus-load-torque curve. As mentioned before, the torque constant specified by the manufacturer of the motor is inaccurate up to 15%. On the other hand side, the torque constant extracted from the experimental results of Test 1, which are expected to reveal the least biased torque constant, contain already torque losses due to viscous and frictional losses within the motor. These added losses will reduce the 'true' torque constant. The slight trend observed for increasing voltage to an decreased slope of the current-versus-load-torque in Test 1 specifies the torque constant between 0.082 and 0.085 $\frac{N\,m}{A}$.

The torque constant given by the manufacturer is $0.12 \frac{N\,m}{A}$, which is greater than the measured torque constant, as expected. The torque constant given by the manufacturer allows the closure of the power balance at the end of this chapter, and provides a good fit between the model and the experimental data. Therefore, the torque constant for the evaluation of the torque losses is assumed to be

$$K_T = 0.12 \frac{N\,m}{A}. \tag{4.5}$$

4.5 Results and Discussion

4.5.1 Experimental Error

The variables in Equation 4.1 are measured values and will be not without error. The contribution of systematic errors was minimized by careful calibration of the dynamometer and a cautious experimental setup. The contribution of random errors was minimized by averaging the instrument readings over time and interpolating the resulting motor curves. Speed and current readings for one measurement were recorded over a period of four seconds after steady state was reached, and averaged using the oscilloscope and the multimeter. As the resulting speed and current-versus-load-torque curves were linear functions, a linear least-squares curve has been fit through the data-points, minimizing the influence of spurious readings. The coefficient of determination has been calculated for the least square curve fits for all tests conducted and was found to be always between 0.99 and 1, which indicates a good fit.

To quantify and characterize the random experimental error, tests were run repeatedly for a chosen thruster configuration and at a fixed voltage. For 24 volts and 40 volts each five tests were conducted, applying the test procedure described above. To determine the influence of the test procedure and possible trends due to the procedure, two more tests at 40 volts were carried out. First, an inverse procedure was applied, starting with low load-torque and increasing the torque. Secondly, data-points were taken randomly over load torque.

From the gathered data, the standard deviation and the 99% confidence interval were calculated. The standard deviation is a measure of how widely values are dispersed from the average value (the sample mean). The confidence interval is a range on either side of a sample mean

	24 volts	40 volts
standard deviation speed (range) [rpm]	2.17 (84-313)	2.63 (531-270)
standard deviation current (range) [A]	0.017 (0.4-4.7)	0.017 (0.2-5.1)
99% confidence interval speed [rpm]	0.72	0.85
99% confidence interval current [A]	0.0058	0.0055

Table 4.3: Experimental Error

which indicates a particular level of confidence that the true value is within this interval. The commonly used confidence interval ψ is the 95% confidence interval, which is given by

$$\psi = \overline{x} \pm 1.96 \, (\frac{\sigma}{\sqrt{n}}), \tag{4.6}$$

where $\overline{x}$ is the sample mean, σ is the standard deviation and n is the sample size. The sample size was approxmately 120 points. The sample mean $\overline{x}$ for these calculations was assumed to be a linear least square curve fit through all gathered data-points for a fixed voltage. Due to the good quality of the data the 99% confidence interval was calculated. The results are summarized in Table 4.3.

Visualizing these results by plotting them in form of error bars does not work as the deviations with respect to the range are so small that the error bars are hardly visible. The standard deviation of the speed and current-versus-load-torque readings, which is the root mean square of the deviations, is in both cases less than 1% of the range. The 99% confidence interval for the speed-versus-load-torque readings in both cases is less than 1 rpm, whereas for the current-versus-load-torque readings a 99% confidence interval of less than 6 mA has been found. A slight trend to a broadened standard deviation and confidence interval for the speed-versus-load-torque readings is observable for increasing voltage, which subsequently means higher torque and speed. This indicates that the deviations of speed and torque readouts are slightly dependent on the torque and speed level. Nevertheless, the increase is very small compared to the range. The standard deviation and confidence interval for the current-versus-load-torque readings is nearly the same for both voltages. This indicates that the deviations of current and torque readouts are independent from the torque and current level and are constant.

The distribution of the deviations from the sample mean are Gaussian for both voltages. As the distribution of all the collected data, including the data collected with varying test-

procedures, is Gaussian, the conclusion can be drawn that the error is random and not systematically dependent on applied voltage or test procedure. No trends appear to shift the distribution.

The speed and current-versus-load-torque curves obtained for the changed test procedures were plotted and compared to the curves obtained applying the standard test procedure. Visual inspection and comparison revealed no significant differences or trends indicating an influence of the test procedure.

As the individual data-points are replaced by a continuous linear function, it is meaningful to investigate the possible deviations of the interpolated functions. A linear function is defined by its slope and intersection. Figure 4-3 shows the 99% confidence interval for the speed and current-versus-load-torque curves. Figure 4-4 shows the 99% confidence interval for the calculated efficiency assuming a constant voltage. This means, that the 'true' values lie to 99% probability, within the plotted envelopes. The envelopes are generated by taking the 99% confidence interval values for slope and intersection of the characteristic motor curves and assuming a worst case by altering the slope and intersection of the characteristic motor curves by the amount of the 99% confidence interval.

These results indicate a high precision for the tests conducted.

4.5.2 Test 1 - motor

Operating Range Characterized The limits for the first set of tests were prescribed by the maximum speed capability of the dynamometer (2000 rpm) and the current limit of the power supply (8 amperes). At high load-torque and voltages of 36 and 40 volts, the motor current exceeded 8 amperes. At lower load torque the motor speed exceeded 2000 rpm. Furthermore, the dynamometer exerted a rest load torque, due to losses within the apparatus, on the motor even when the load torque has been turned off. This prevented the motor from spinning at full no-load speed.

Characteristic motor curves Due to the limitations discussed above, only segments of the motor curves shown in Figure 3-2 (a), (b), (c) and (d) could be reproduced. A typical group of speed, current, power-out, and efficiency-versus-load-torque curves are shown for the 24 volts

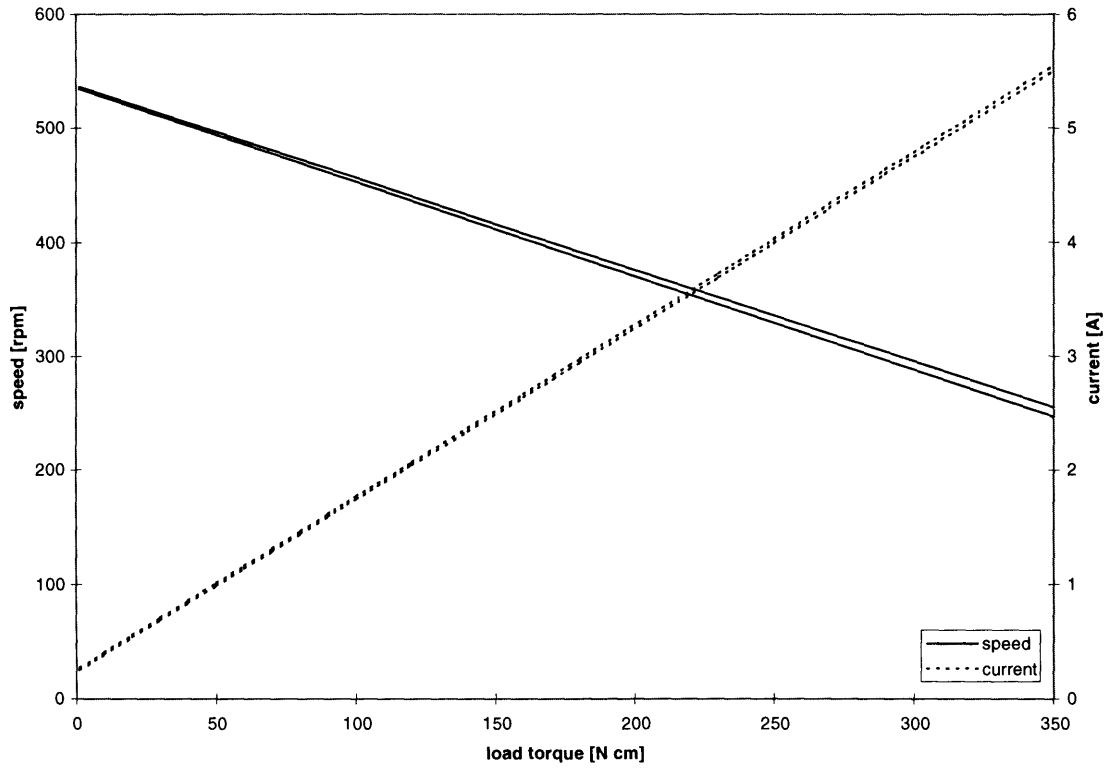

Figure 4-3: 99% Confidence Interval of the Speed and Current Curves. The plotted envelope shown for both curves was generated by assuming 'worst case values' for slope and intersection of the curves.

test case in Figure 4-5 and Figure 4-6. Figure 4-5 shows the discrete datapoints as well as the least square fit, whereas Figure 4-6 has been generated by using the continuous speed and current-versus-load-torque curves resulting from the least square curve fit.

The plots show the expected results (compare with Figure 3-2). Motor-speed-versus-load-torque and motor-current-versus-load-torque are linear functions. Power-out has a quadratic dependence on load torque as it is the product of two linearly-dependent values, speed and torque. Efficiency is linear over load torque within the tested range. The physical explanation for the linear behavior of the efficiency is that, within the tested range, I^2R losses cause a linear decrease in efficiency for increasing load torque whereas speed dependent losses are not significant.

The discussion applies to all tests conducted in this configuration over the whole tested

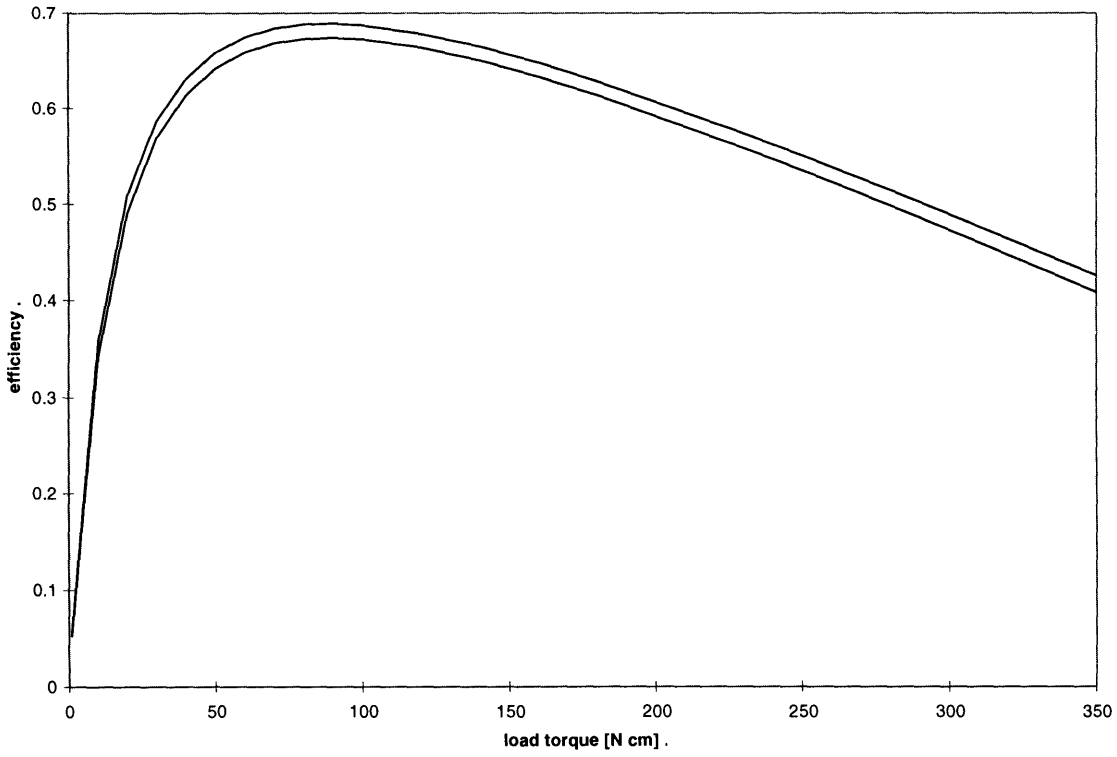

Figure 4-4: 99% Confidence Interval of the Efficiency Curve. The plotted envelope shown was genrated by assuming the 'worst case values' for speed and current from Figure 4-3.

voltage range from 24 to 40 volts.

Trends For increasing voltage, two trends in the speed-versus-load-torque curves are observable. First, the no-load speed is shifted to higher speed for increasing voltage. This is in agreement with the theoretical behavior of this curve described by Equation 3.8, where the theoretical no-load speed (y-axis intersection of the speed-versus-load-torque curve) is a function of the applied voltage. Second a slight trend to increasing slope for increasing voltage is observed (-25 $\frac{rpm}{V}$ for 24 volts to -28.5 $\frac{rpm}{V}$ for 40 volts). A trend in the current-versus-load-torque curve for increasing voltage is a slight decrease in the slope of the curve (0.085 $\frac{N\,m}{A}$ for 24 volts to 0.082 $\frac{N\,m}{A}$ for 40 volts).

Both of the latter trends are not captured in the model, but indicate an improved motor performance at higher voltages. Another trend in the current-versus-load-torque curve is a

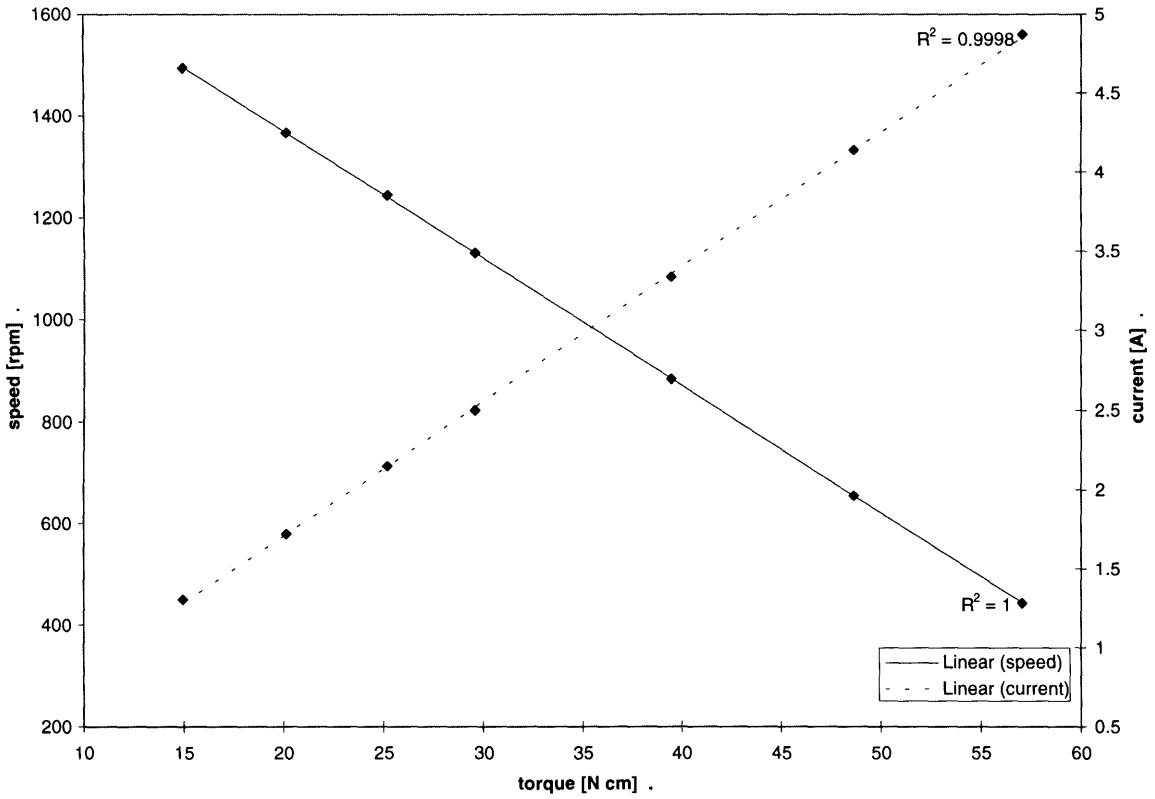

Figure 4-5: Motor Speed and Current at 24 volts for Test 1. Discrete data as well as the linear least-square curve-fit is shown.

slightly increasing no-load current for increasing voltage (about 0.05 amperes over a voltage range from 24 to 40 volts). This trend is contained in the model discussed above. The no-load current is a function of the torque loss, but not of the applied voltage. Therefore, it can be supposed that the torque losses are slightly dependent on the applied voltage as higher voltage means higher speed and thus increasing speed dependent losses.

Qualitative efficiency behavior Figure 4-7 presents the efficiency curves using the continuous speed and current-versus-load-torque curves of the first test series. The following characteristics are revealed:

- Efficiency increases with decreasing load torque, which is equivalent to increasing motor speed as the speed-torque relationship is linear.

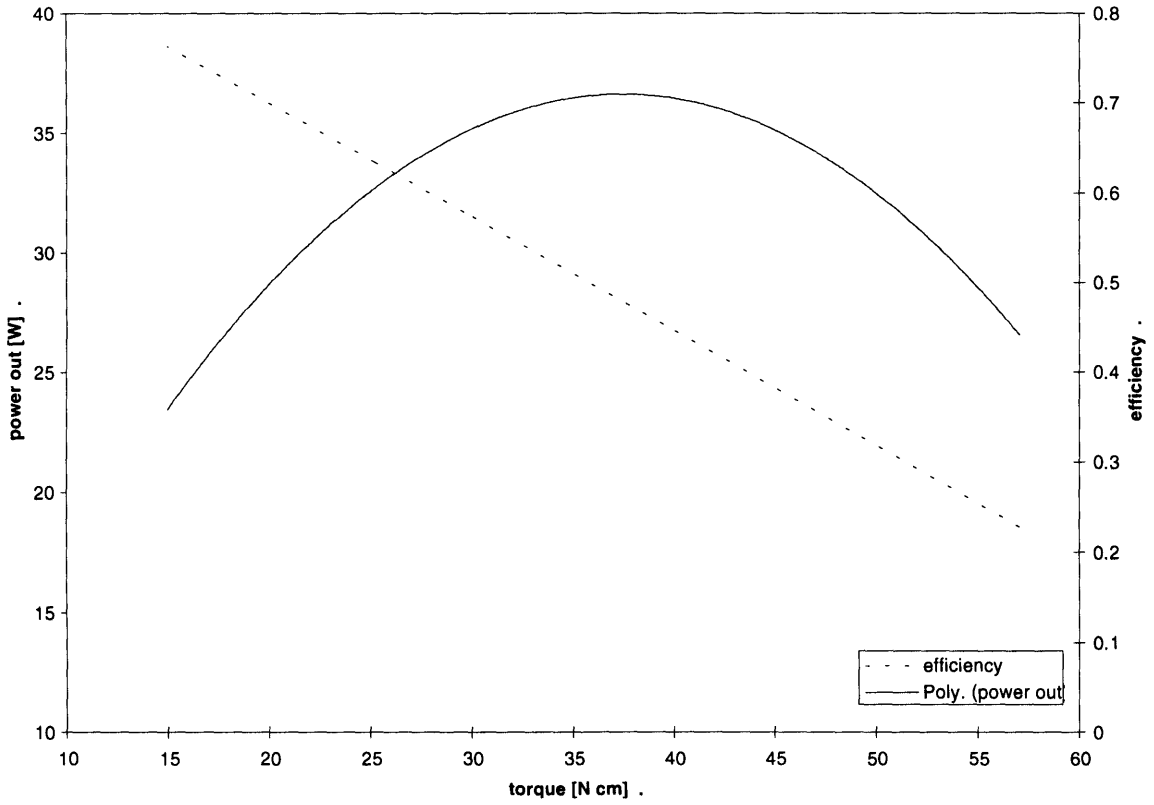

Figure 4-6: Power-Out and Efficiency at 24 volts for Test 1. Power-Out is a second-order-polynomial while efficiency behaves linear within the tested load-torque range. Both curves were generated from the least-square fit for the speed and current curves shown in Figure 4-5.

- Efficiency increases with increasing voltage.

- Efficiency behaves linearly within the tested range.

- With increasing voltage, the slope of the efficiency curve decreases, providing a decreased change of efficiency over load torque.

- The peak-efficiency shown in Figure 3-2 could not be reached due to the rest load torque exerted by the dynamometer and the maximum speed-capability of the dynamometer.

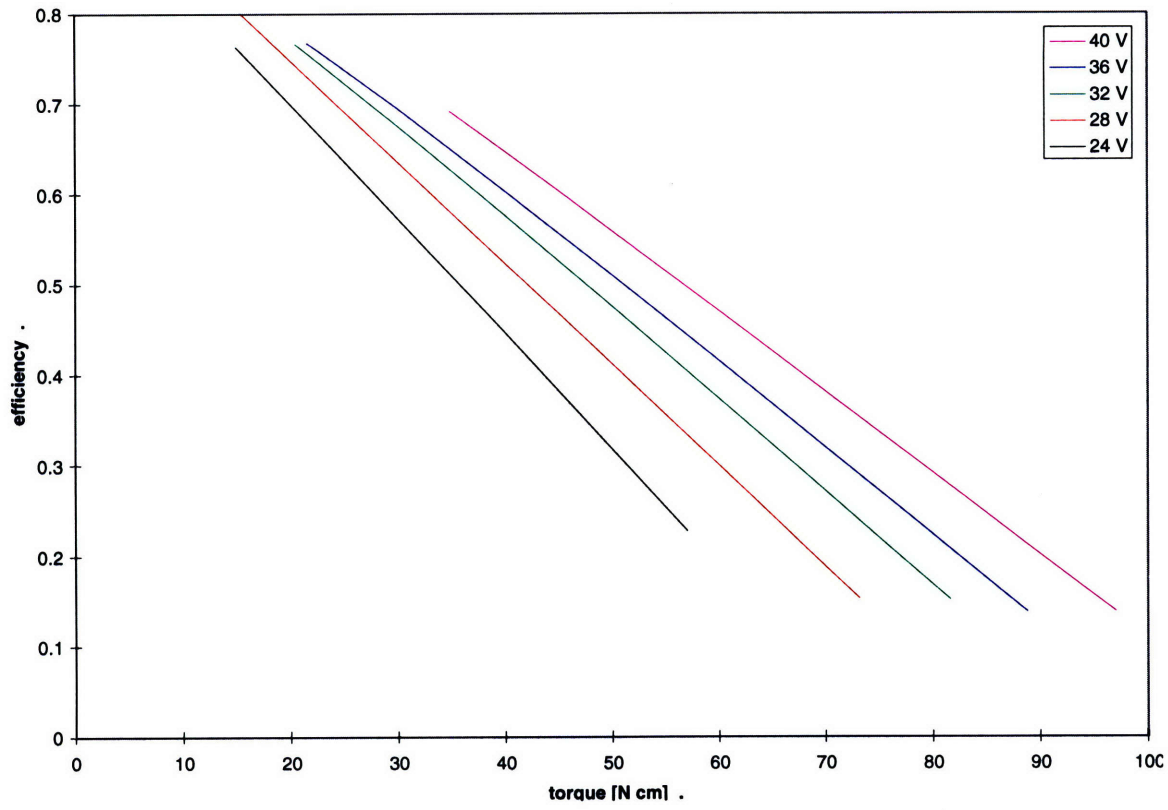

Figure 4-7: Efficiencies Test 1. The efficiency curves for all tests conducted in test configuration 1, differing by the applied voltage in increments of 4 volts, are shown.

4.5.3 Test 2 - motor + seal

Operating Range Characterized The second test was very similar to the first one, differing only by the presence of the shaft-seal, which had no significant influence on the limitations discussed for Test 1.

Characteristic motor curves speed and current-versus-load-torque curves are shown for the 28 volts test-case in Figure 4-8. Both cases, motor and motor + shaft-seal are plotted in the same graph to show the influence of the shaft-seal on the characteristic motor curves.

As discussed above, the shaft-seal is expected to give a constant or slightly speed dependent torque loss, independent from the load torque. It is clearly observable in this case (and also for the other tested voltages) that both current and speed-versus-load-torque curves are parallel.

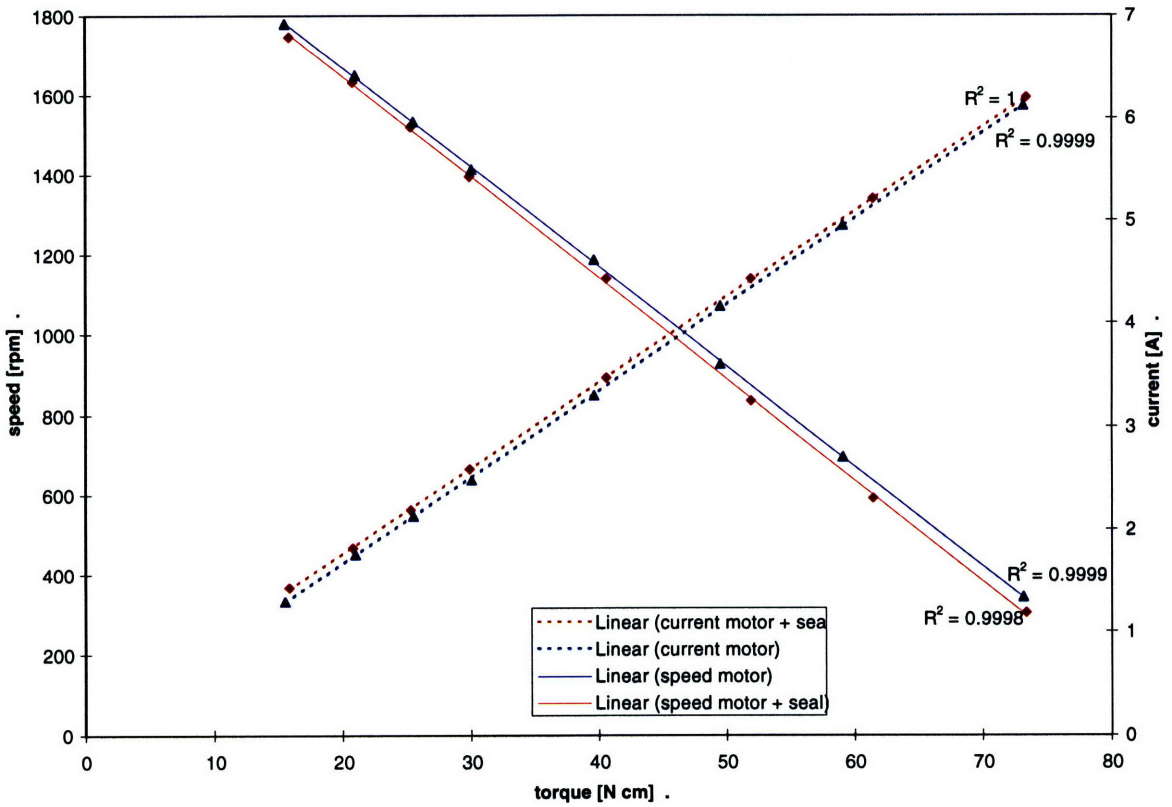

Figure 4-8: Motor Speed and Current at 28 volts Test 1 and 2 Compared. Discrete data as well as the linear least-square curve-fit is shown. The comparison in this plot shows the impact of the shaft-seal on the speed and current curves.

This indicates that there is, as expected, a constant torque-loss independent of speed and load torque. It also indicates that the variation in the frictional coefficient is small, as the torque loss does not exhibit speed dependence.

The discussion applies to all tests conducted in this configuration over the whole tested voltage range from 24 to 40 volts.

Trends For increasing voltage, the same trends, within the same range and order of magnitude, are seen as in Test 1. By comparing the no-load currents for Test 1 and Test 2 at each tested voltage, it is apparent that they are constantly separated by an increment of about 0.07 amperes. This is also true for the no-load speeds and currents, where the separation amounts about 15 rpm. The slopes of both current and speed-versus-load-torque curves are identical for

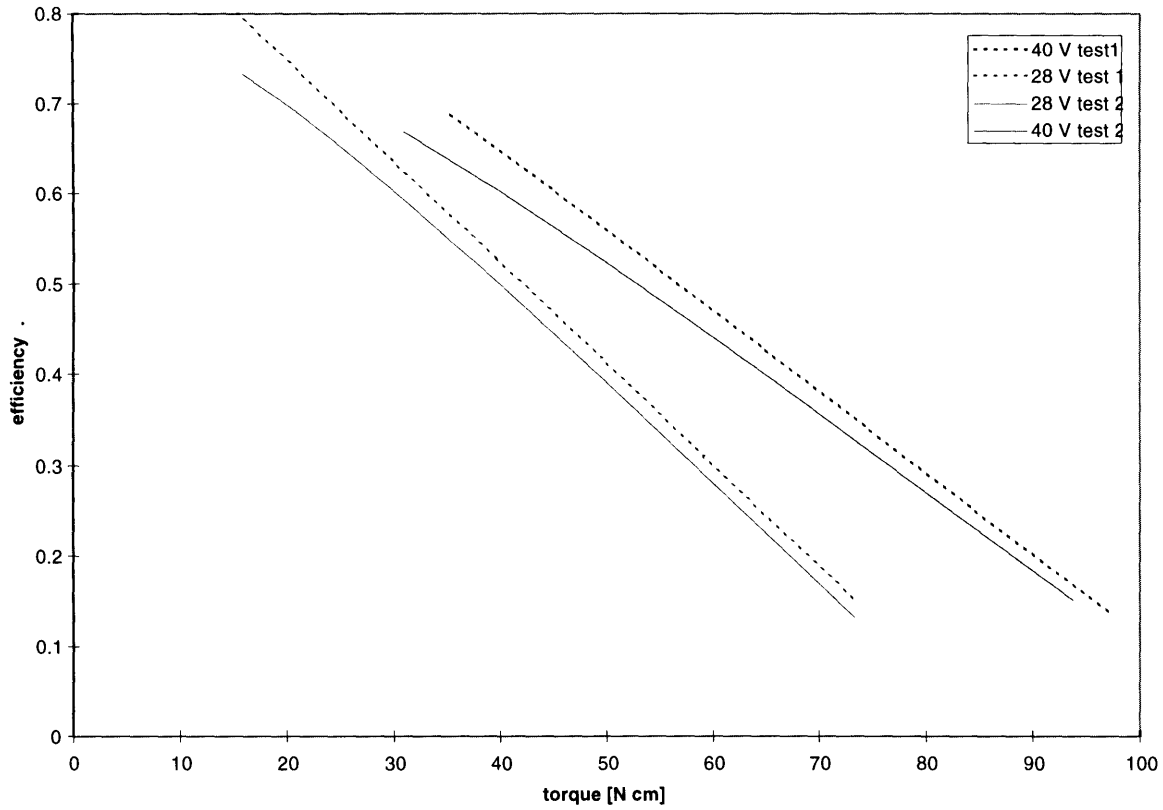

Figure 4-9: Efficiency Test 2 Compared to Test 1 at 28 and 40 volts. The comparison of both efficiency curves shows the impact of the shaft-seal on efficiency. The Test 2 curve shows a slight curvature in contrast to the linear curve form Test 1.

Test 1 and Test 2.

Qualitative efficiency behavior Selecting the efficiency curves at 28 and 40 volts and plotting them for Test 1 and Test 2 in the same graph, shows the effect of the shaft-seal on efficiency (Figure 4-9). Again, the efficiency curves were generated using the continuous speed and current-versus-load-torque functions and therefore no discrete datapoints are shown. For Test 2, a slight curvature of the efficiency curves is seen, in contrast to the linear curves in Test 1. The small torque loss becomes increasingly significant at lower load torque which is equivalent to higher motor speed.

Torque loss It appears that the torque loss due to the shaft-seal is independent from the motor speed, the load torque and the applied voltage and therefore constant. The value obtained is approximately 1.2 Ncm. For example, at a speed of 1650 rpm and a load torque of 20 Ncm, the overall power loss, due to torque and increased I^2R losses, is 2.9 watts. At a load torque of 70 Ncm, the overall power loss amounts to 3.3 watts due to torque and increased I^2R losses.

4.5.4 Test 3 - motor + seal + oil

Operating Range Characterized Filling the thruster with oil had no significant influence on the operating range discussed for Test 1 and 2.

Characteristic motor curves Figure 4-10 shows the speed and current-versus-load-torque curves for the 28 volts test case. Both cases, motor + seal and motor + seal + oil are plotted in the same graph to show the influence of the oil-filling on the characteristic motor curves. According to the model presented earlier, it can be expected that the oil-filling generates a linearly speed dependent torque loss. The example of the characteristic motor curves for this test series, given in Figure 4-10 for the 28 volts test, shows a not necessarily expected result.

Comparing the current and speed-versus-load-torque curves from Test 3 to the ones from Test 2 reveals a decreased slope of both curves, while the increase in slope of the speed-versus-load-torque curve is more significant than the increase of the current-versus-load-torque curve. This is in agreement with the behavior predicted by the theoretical model for linearly speed dependent losses as discussed before. It can therefore be supposed that due to the oil-filling, linearly speed dependent losses occur.

The unexpected result is that the characteristic motor curves are not significantly shifted apart, but intersect. In particular, for load torque greater than 35 Ncm ,the speed achieved in Test 3 is higher than in Test 2, and vice versa for the opposite side of this range. Instead of the expected decrease in speed over the whole range, a range with even higher speed output is observable. Both current-versus-load-torque curves are slightly shifted apart, but not as significantly as expected. They converge at the high torque end of the tested range. Generally speaking, the range of improved motor performance comparing both tests is characterized by relatively low rotational-speed and high load-torque, whereas the range of decreased motor

performance is characterized by relatively high rotational-speed and low load-torque.

One possible explanation for this behavior is that the lubrication in the ball-bearings of the motor has been increased by the added oil. At low rotational-speed this causes an increased performance, whereas for increasing speed viscous losses increase, first canceling out the effects of improved lubrication, and then further decreasing motor performance. Another explanation could be that Test 2 overestimated the losses due to the shaft-seal as the vertical orientation of the thruster did not adequately lubricate the shaft-seal. Filling the whole thruster with oil then for Test 3, may have improved the lubrication of the shaft-seal and therefore also influenced the characteristic motor curves by shifting them to higher performance characteristics.

The discussion applies to all tests conducted in this configuration over the whole tested voltage range from 24 to 48 volts.

Trends For increasing voltage the same trends within the same range and order of magnitude as in Test 1 and 2 are observable. The no-load current for Test 2 and Test 3 at each tested voltage differ by an increment of about 0.07 amperes for each 4 volts increment. This is the same separations as found for Test 2. This indicates that the influence of the shaft-seal, which was found to exert a constant torque loss, has not changed, and that the unexpected behavior of the characteristic motor curves is due to a better lubrication of the ball-bearings and not due to an unrealistic lubrication of the shaft-seal in Test 2. The no-load speeds are constantly shifted apart over the tested voltage range where the separation amounts about 30 rpm. The slope of the current-versus-load-torque curve is constantly decreased by an amount of about 0.0012 $\frac{A}{N\,cm}$ over the voltage range from 24 to 36 volts, while the decrease in slope of the speed-versus-load-torque curve linearly increases from 1 $\frac{rpm}{N\,cm}$ for 24 volts to 1.6 $\frac{rpm}{N\,cm}$ for 36 volts.

Qualitative efficiency behavior Selecting two efficiency curves, at 28 and 40 volts, and plotting them for Test 2 and Test 3 in the same graph, shows the effect of the oil-filling on efficiency (Figure 4-11). The improved efficiency due to the oil-filling for decreasing motor speed and increasing load torque is apparent as well as the decrease in efficiency for increasing motor speed and decreasing load torque.

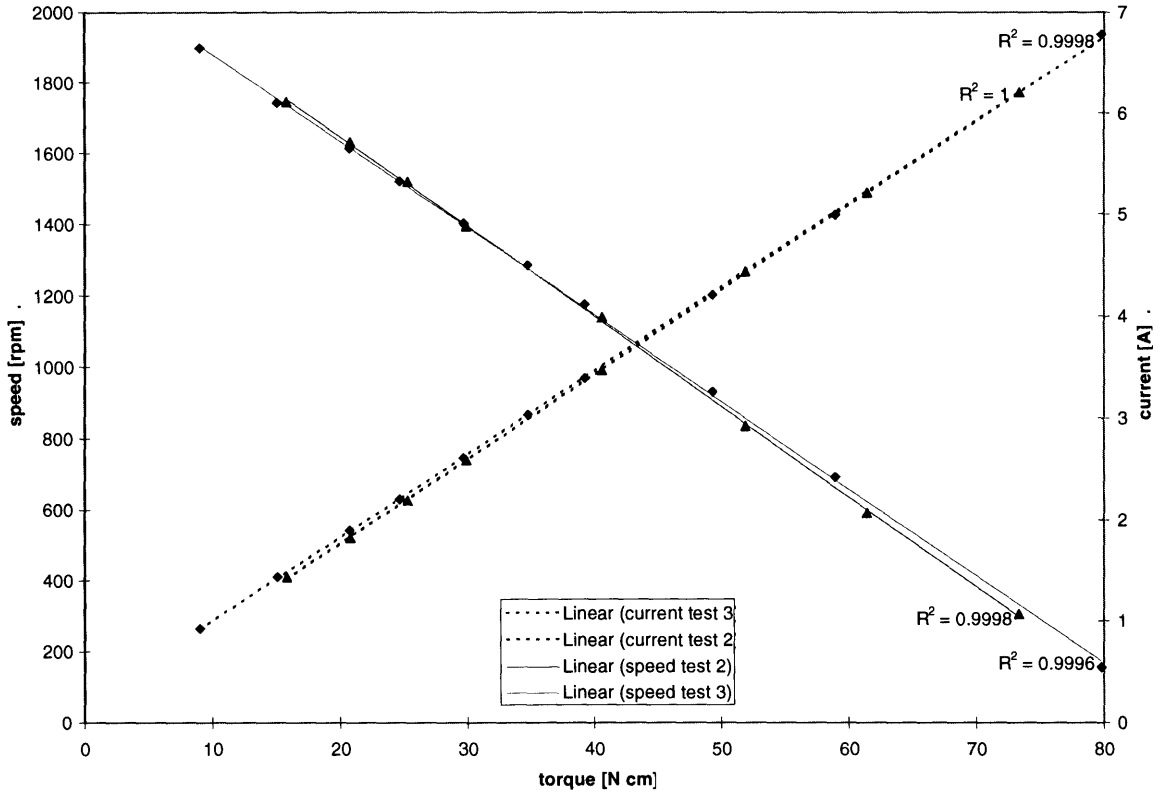

Figure 4-10: Motor Speed and Current at 28 volts Test 2 and 3 Compared. Discrete data as well as the linear least-square curve-fit is shown. The comparison in this plot shows the impact of the oil on the speed and current curves. It can be seen that the oil has a small effect.

Torque loss It appears that the torque gain and loss, respectively, due to the oil-filling depends on the motor speed. It does not make much sense to calculate the torque loss in this case as the torque loss and gain, respectively, varies with the motor speed and is small. For example, the torque loss at a load torque of 15 Ncm, which corresponds to a speed of 1760 rpm, is about 0.78 Ncm. This is equivalent to a power loss of about 1.84 watts, including the increase in I^2R losses. For increasing load torque, the losses become less as motor speed reduces.

4.5.5 Test 4 - motor + seal + oil + gearbox

Operating Range Characterized The presence of the gearbox shifts the torque and speed output from the motor to higher and lower regimes, respectively. This test series was able to

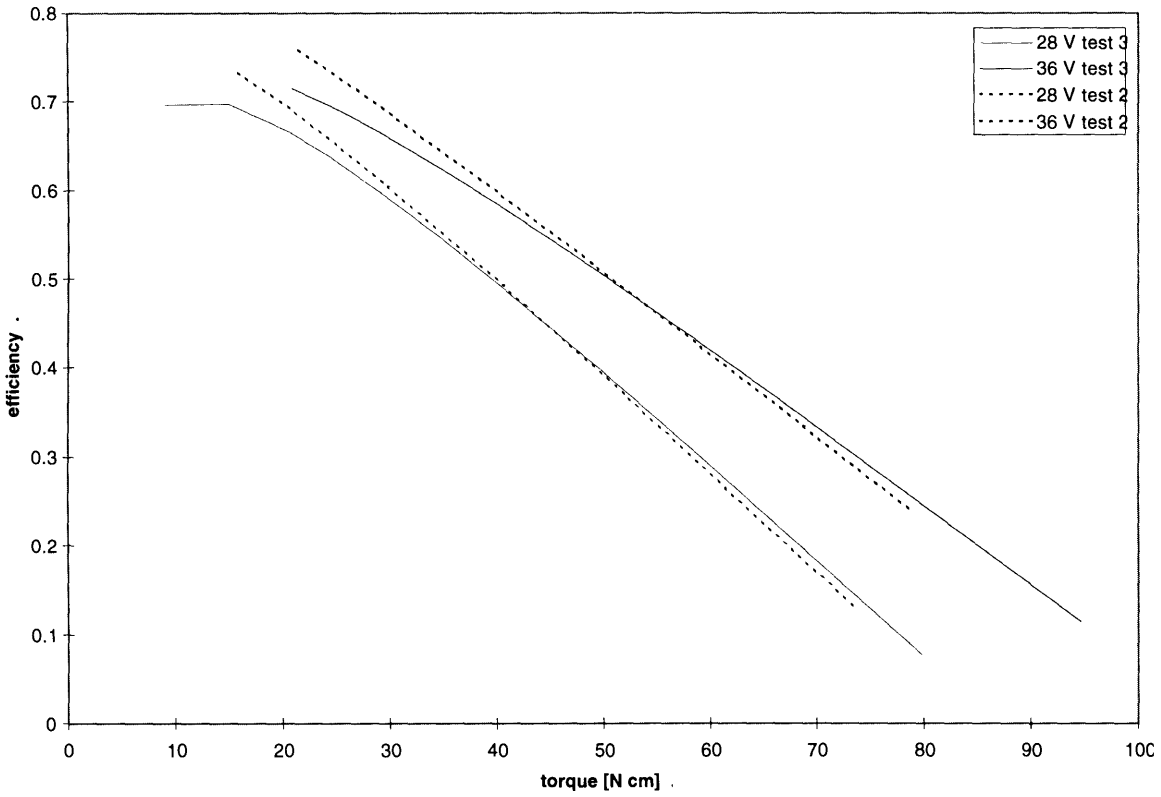

Figure 4-11: Efficiency Test 3 Compared to Test 2 at 28 and 36 volts. The comparison of both efficiency for curves shows the small impact of the added oil-filling on efficiency.

characterize the motor over a much broader speed range than previous tests, including the high-speed range where viscous losses become dominant. The limit encountered in this test series is the maximum torque and power capability of the dynamometer rather than its maximum speed capability.

Characteristic motor curves Speed and current-versus-load-torque curves are shown for the 36 volts test case in Figure 4-12. Both cases, motor + seal + oil and motor + seal + oil + gearbox are plotted in the same graph to show the influence of the gearbox on the characteristic motor curves. To make the test results of Test 3 and 4 comparable, the results of Test 3 have been shifted by the gearbox reduction ratio to higher torque and reduced speed. Discrete data are not plotted for Test 3 as the continuous curves have been shifted and not the discrete data points.

According to the model developed above, it can be expect that the gearbox generates a speed and torque dependent torque loss that may be non-linear. But as both current and speed-versus-load-torque motor-curves are linear ($R^2 \approx 1$ for least square curve fit), it can be supposed that non-linear influences are small and that occurring losses are nearly linear.

Figure 4-12 shows that the characteristic motor curves from Test 3 and Test 4 are offset but parallel. This is a not necessarily expected result as speed as well as torque dependent losses tend to alter the slope of the speed-versus-load-torque curve. According to the model, losses that depend linearly on the load torque significantly increase the slope of the speed-versus-load-torque curve, whereas losses that depend linearly on the speed significantly decrease its slope. Therefore, it can be supposed that in this case the opposite trend of speed dependent and load torque dependent losses cancel each other out. Or in other words, due to the fact that both curves are parallel, it can be supposed that speed-dependent as well as torque-dependent losses are encountered due to the presence of the gearbox.

Comparing the slopes of the current-versus-load-torque curves shows that the slope of Test 4 compared to Test 3 is slightly increased. By invoking the model again, this behavior can be understood. Linearly load torque dependent losses significantly increase the slope of the current-versus-load-torque curve, whereas linearly speed dependent losses slightly decrease its slope. Therefore, if both kinds of losses occur, it can be expected that the slope of the current-versus-load-torque curve is slightly increased.

The discussion applies to all tests conducted in this configuration over the whole tested voltage range from 24 to 52 volts.

Trends For increasing voltage, basically the same trends (within the same range and order of magnitude) as in Test 1, 2 and 3 are seen except for the no-load currents. By comparing the no-load currents for Test 3 and Test 4 at each tested voltage, it is seen that the trend to an increasing value over voltage, observed in Test 1, 2 and 3, is weaker now in Test 4. For increasing voltage, the difference between the no-load current of Test 3 and 4 is linearly decreasing. In particular, the difference between the Test 3 and 4 value decreases from 0.07 amperes at 24 volts to 0.04 amperes at 48 volts. Invoking the model again, this implies that the torque loss becomes comparably smaller for increasing voltage than in Test 1, 2 and 3. Recall that the

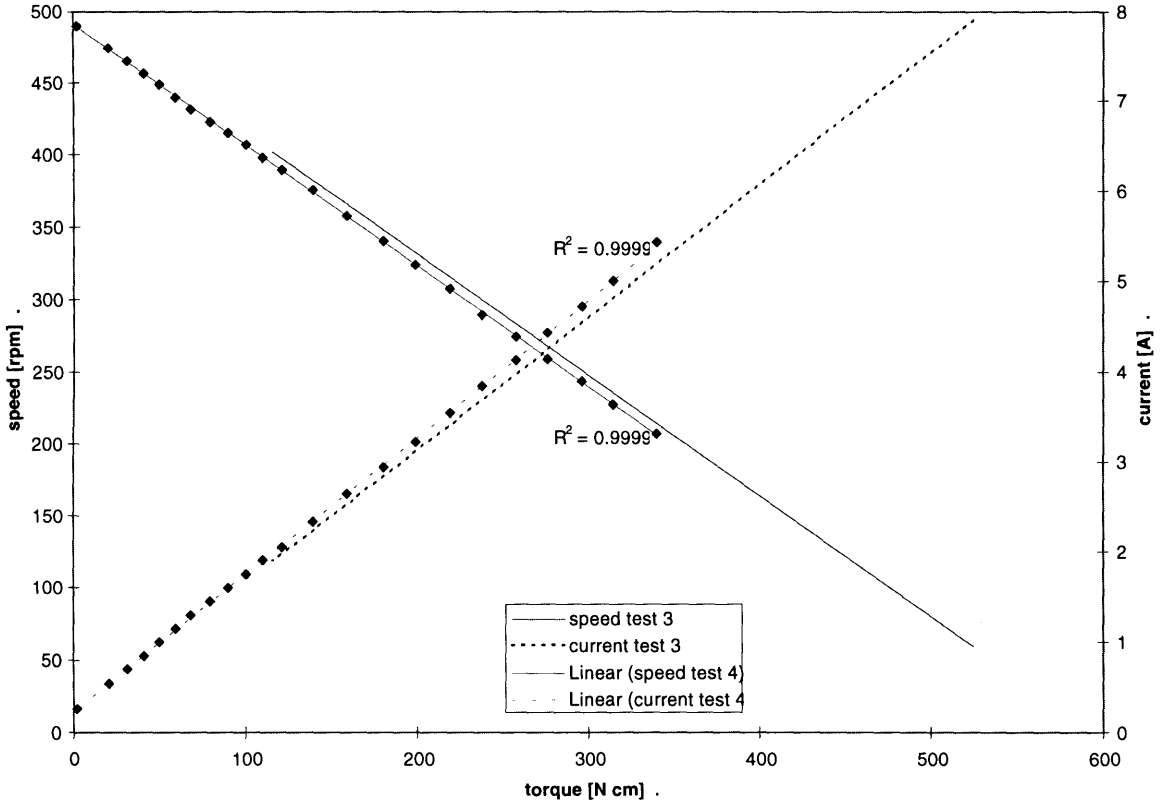

Figure 4-12: Motor Speed and Current at 36 volts Test 3 and 4 Compared. For Test 4 discrete data and the least-square curve-fits are shown. For Test 3 only the continuous curve-fit is shown as the curves had to be shifted (by the gearbox-reduction-ratio) to higher torque and lower speed to make both test comparable. The comparison in this plot shows the impact of the oil-filled gearbox on the speed and current curves.

no-load current is a function of the torque loss but not of the applied voltage. The no-load speeds are shifted apart by a constant over the tested voltage range. The separation is about 10 rpm in terms of gearbox shaft-speed or 55 rpm in terms of motor speed. The slope of the speed-versus-load-torque curve in both cases is nearly identical over the comparable voltage range, whereas the slopes of the current-versus-load-torque curves are constantly separated by about 0.0005 $\frac{A}{N\,cm}$.

Qualitative efficiency behavior Selecting two efficiency curves, at 24 and 36 volts, and plotting them for Test 3 and Test 4 in the same graph, shows the effect of the gearbox on efficiency (Figure 4-13). The difference in efficiency between Test 3 and 4 decreases with increasing

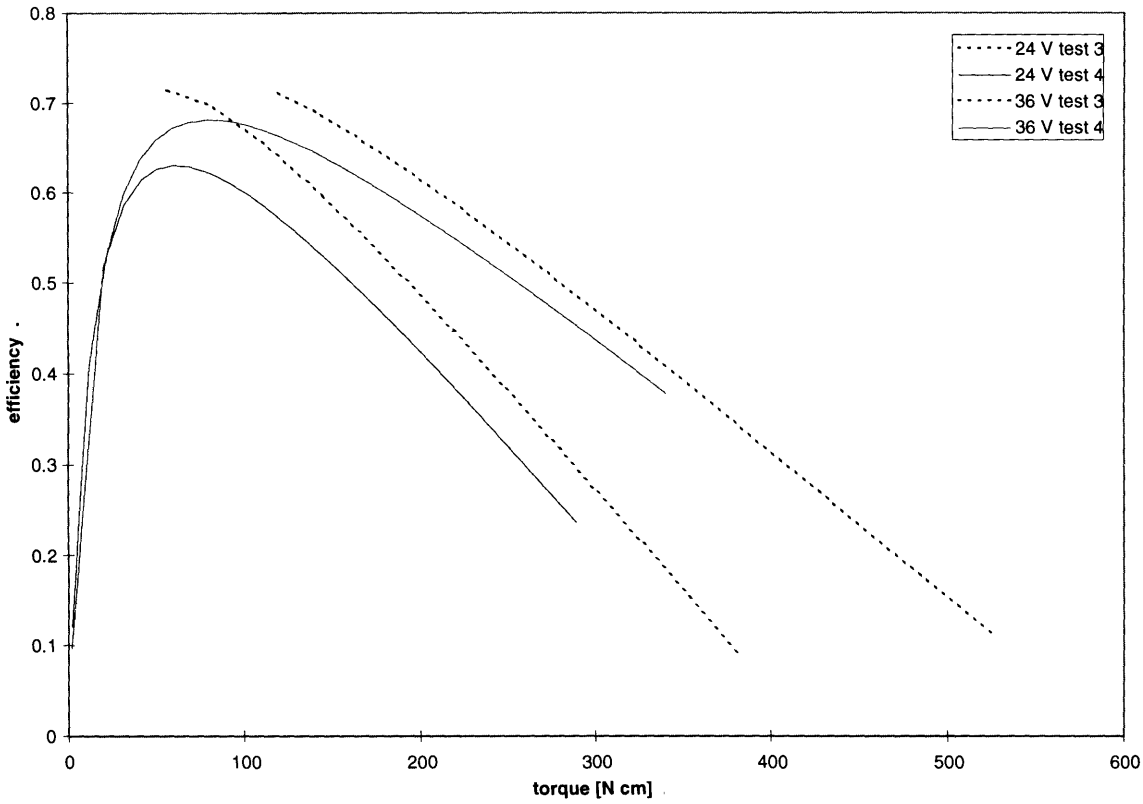

Figure 4-13: Efficieny Test 4 Compared to Test 3 at 28 and 36 volts. The comparison of both efficiency curves shows the impact of the gearbox on efficiency. It can be seen that the gearbox has a significant impact on efficiency.

voltage. The difference in efficiency due to the gearbox in this comparison is significant. The gearbox can therefore be identified as a important cause of inefficiency.

As in this series of tests the gearbox allowed the motor to reach speed regimes where viscous losses become dominant, it is interesting to plot the efficiency curves for all tests conducted in this configuration in one graph. This has been done in Figure 4-14. The following characteristics are observable:

- After reaching a peak, the efficiency drops rapidly for decreasing load torque due to viscous losses at high rotational-speed.

- On the high-torque side of the efficiency peak, efficiency decreases with increasing load torque until stall torque is reached. The efficiency curve becomes increasingly linear for

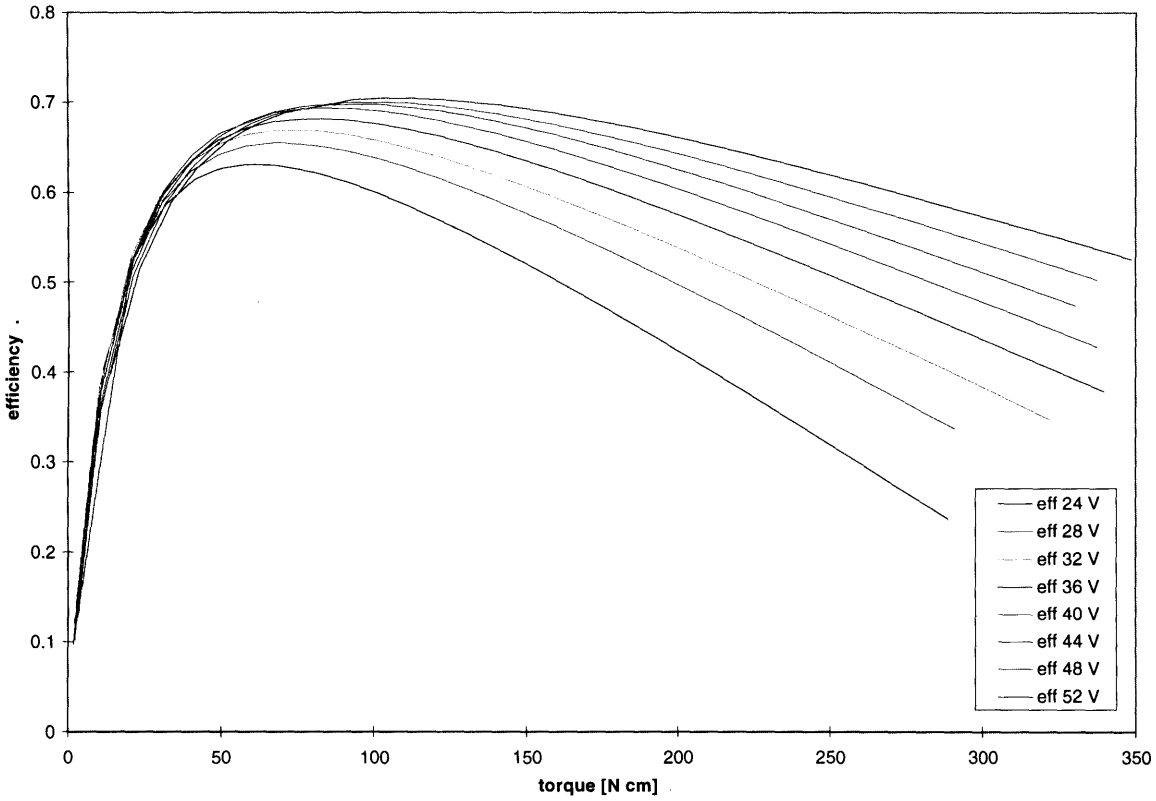

Figure 4-14: Efficiencies Test 3. Due to the gearbox the motor could now be tested at high speed (where viscous losses grow dominant), which was not possible before due to the maximum speed-capability of the dynamometer.

higher load torques.

- Efficiency increases with increasing voltage. The magnitude of the efficiency increase is greatest at low voltages and decreases for higher voltages. For increasing voltages the efficiency peak is shifted to higher load torque.

- The maximum measured efficiency of the thruster is about 71% at an applied voltage of 52 volts.

The underlying principles governing efficiency are seen in this plot. As load torque increases, I^2R losses become dominant. For low load-torque, which is equivalent to high rotational-speed, viscous losses become dominant. Efficiency reaches a maximum between these both extremes.

Torque loss It appears that the torque loss due to the gearbox is dependent on the shaft speed as well as on the load torque. The slope of the current-versus-load-torque curve is constantly increased over the voltage range, whereas the no-load current varies linearly compared to the previous test. As an quantitative example, the maximum and minimum torque losses due to the gearbox within the comparable range of Test 3 and 4 are calculated. The torque and speed values are in terms of shaft torque and speed and not in terms of motor torque and speed. The maximum torque loss, at a load torque of 380 Ncm, is 0.47 Ncm, causing a power loss of 6.12 watts (including I^2R losses) at a shaft speed of 172 rpm. The minimum torque loss, at a load torque of 120 Ncm, is 0.2 Ncm, causing a power loss of 0.97 watts (including I^2R losses) at a shaft speed of 390 rpm.

4.5.6 Test 5 - motor + gearbox

Operating Range Characterized Test 5 was similar to Test 4 one, differing by the removed oil-filling and shaft-seal, which had no significant influence on the limitations discussed for Test 4.

Characteristic motor curves speed and current-versus-load-torque curves are shown for the 36 volts test case in Figure 4-15. The two cases, motor and motor + gearbox, are plotted in the same graph to show the influence of the gearbox. In contrast to Test 4, Test 5 reveals the influence of the gearbox decoupled from oil-filling, lubrication and shaft-seal effects. In order to make the test results of Test 1 and 5 comparable, the results of Test 1 have been shifted by the gearbox reduction ratio to higher torque and reduced speed.

Comparing the current and speed-versus-load-torque curves from Test 5 to the curves from Test 1 reveals a slightly decreased slope of the speed-versus-load-torque curve, while the slope of the current-versus-load-torque curve is significantly increased. This indicates speed-as well as load-torque-dependent losses. According to the model, load-torque-dependent losses tend to increase the slope of both characteristic motor curves significantly, whereas speed-dependent losses tend to decrease the slope of the current-versus-load-torque curve slightly and decrease the slope of the speed-versus-load-torque curve significantly.

The discussion applies to all tests conducted in this configuration over the whole tested

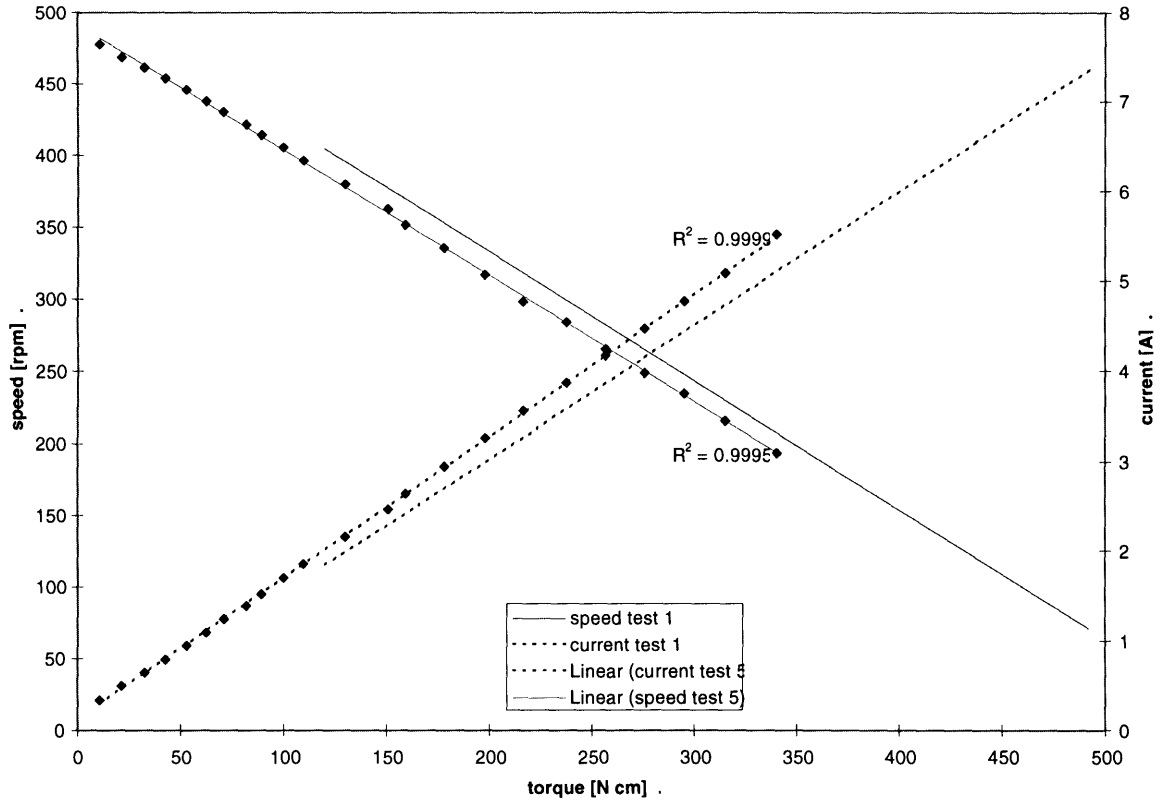

Figure 4-15: Motor Speed and Current at 36 volts Test 1 and 5 Compared. For Test 5 discrete data and the least-square curve-fits are shown. For Test 1 only the continuous curve-fit is shown as the curves had to be shifted (by the gearbox-reduction-ratio) to higher torque and lower speed to make both test comparable. The comparison in this plot shows the impact of the oil-filled gearbox on the speed and current curves.

voltage range from 24 to 40 volts.

Trends For increasing voltage, the same trends within the same range and order of magnitude as in Test 1, 2 and 3 are observable for the no-load current and speed as well as for the slope of the current-versus-load-torque curve. In contrast to earlier tests, the trend of the slope of the speed-versus-load-torque curve is reversed. In the previous tests the slope decreased over the tested voltage range. Here it shifts to higher slope and increases over the voltage range. Compared to Test 5, the slope of the current-versus-load-torque curve is constantly shifted to an increased value, whereas the no-load current is nearly identical over the tested voltage range. The no-load speed is likewise nearly identical compared to Test 5 over the tested voltage range.

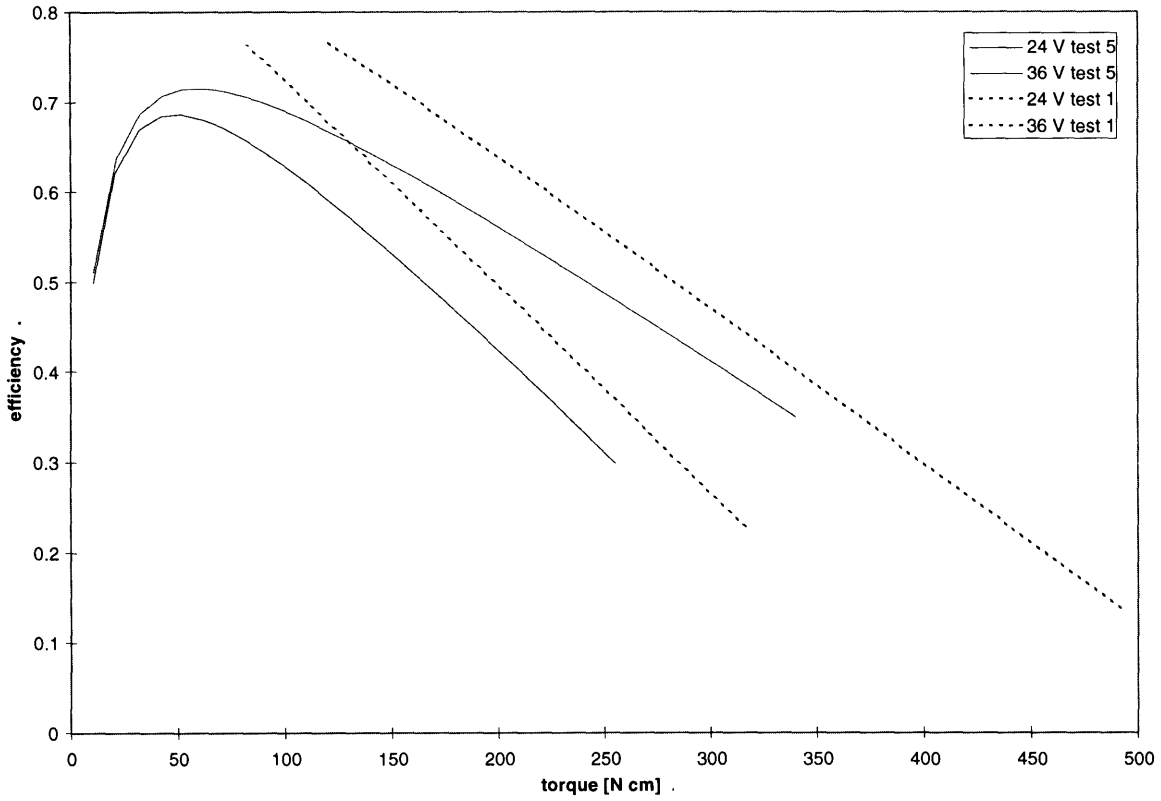

Figure 4-16: Efficiency Test 5 Compared to Test 1 at 28 and 36 volts. The comparison of both efficiency curves shows the impact of the gearbox, decoupled from oil-filling and shaft-seal, on efficiency. It can be seen that the gearbox has a significant impact on efficiency.

Qualitative efficiency behavior Plotting two efficiency curves at 24 and 36 volts for Test 4 and Test 5 in the same graph, shows the effect of the gearbox, decoupled from effects of the seal and the oil-filling, on efficiency (Figure 4-16). To show the performance difference between the oil-filled thruster and the thruster without oil-filling and shaft-seal, the efficiency curves of Test 4 and 5 are compared in Figure 4-17 at 28 and 36 volts. This comparison clearly reveals the influence of viscous effects on the performance of the thruster. At low load-torque, which is equivalent to high rotational-speed, the oil-filled thruster is clearly less efficient than the not oil-filled one. In contrast, for higher load torque viscous losses become less important and the increased lubrication due to the oil-filling makes the oil-filled thruster superior to the not oil-filled one.

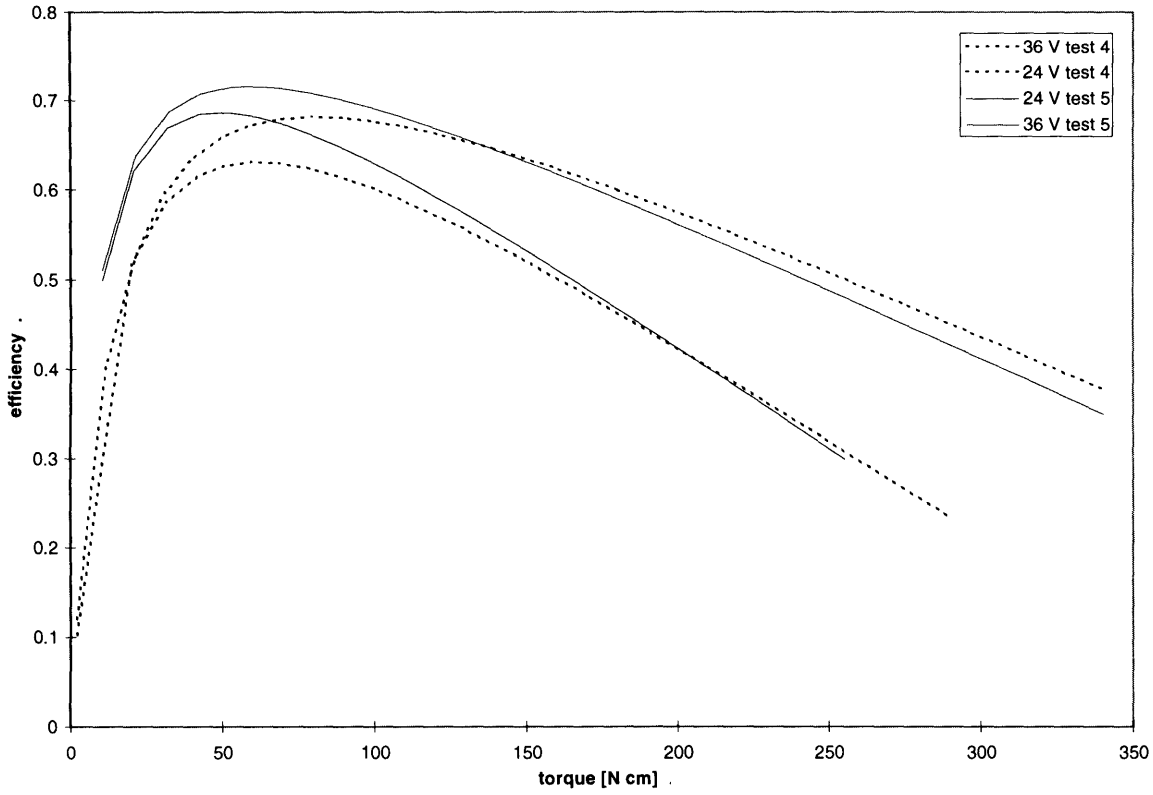

Figure 4-17: Efficiency Test 5 Compared to Test 4 at 28 and 36 volts. The comparison of both efficiency curves shows the impact of the oil-filling (lubrication and viscous losses) and of the shaft-seal on efficiency.

Torque loss As in Test 4, it can be supposed that the torque loss due to the gearbox is dependent on the shaft speed as well as on the load torque. As a quantitative example, the maximum and minimum torque losses due to the gearbox within the comparable range of Test 5 and Test 1 at 36 volts are calculated. The maximum torque loss, at a load torque of 360 Ncm, is 1.9 Ncm, causes a power loss of 0.85 watts (including I^2R losses) at a shaft speed of 172 rpm. The minimum torque loss, at a load torque of 120 Ncm, is 3.4 Ncm, causing a power loss of 0.73 watts (including I^2R losses) at a shaft speed of 400 rpm.

4.5.7 Test 6 - temperature effects

Operating Range Characterized The range of torque and speed characterized in Test 6 were the same as for Test 4, as the exact same configuration was used. Two tests, at the same voltage, were conducted as described in the paragraph outlining the experimental procedures.

Characteristic motor curves speed and current-versus-load-torque curves are shown for the 3°C temperature case compared to the reference test, conducted at room temperature, in Figure 4-18. This test is meant to simulate the environment a thruster encounters in a realistic deep-ocean application. The slope of both characteristic motor curves is decreased for the low-temperature test-case compared to the reference test. Furthermore, both speed-versus-load-torque curves intersect in the low load-torque range. The model does not address these characteristics, as the physical laws governing the influences are not easily quantifiable.

The model indicates that the viscosity of the oil, the conductivity of the stator windings, and the heat dissipation increases for decreasing temperature. The increased viscosity of the oil-filling of the thruster will reduce motor performance, particularly within the high speed-range, whereas the improved conductivity of the stator windings and the improved heat dissipation will improve motor performance.

Qualitative efficiency behavior Figure 4-19 shows the effect of the decreased temperature on the thruster performance. For higher load torque, the performance of the thruster is significantly increased, whereas for light loading, which causes high motor speed, viscous losses increase and compensate the improved electrical performance of the motor. At high load-torque the positive influence of low temperature is largest as high current is drawn, which causes excessive I^2R losses. These losses are reduced in the low temperature case as the motor resistance is lower and the heat due to the occurring losses is better dissipated, resulting in turn in a lower winding temperature.

Torque loss The effect of the low temperature generally causes an increase in torque. The maximum torque gain within the comparable range at 300 Ncm load torque is about 0.3 Ncm at a speed of 320 rpm. This is equal to a power gain of about 3 watts.

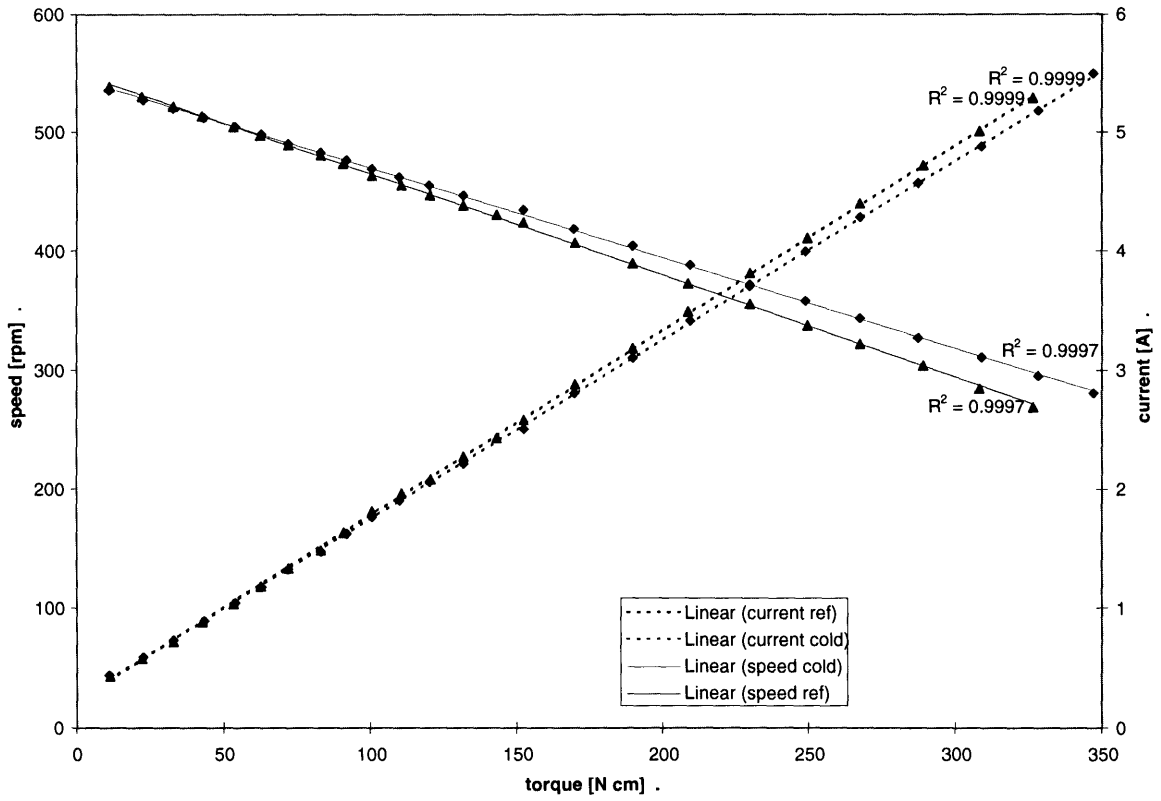

Figure 4-18: Motor Speed and Current Test 6 for Reference Test at Room Temperature and Test at 3°C. Discrete data as well as the linear least-square curve-fit is shown. The comparison in this plot shows the impact of of a low-temperature environment on the speed and current curves.

4.5.8 Test 7 and Test 8 - viscosity and lubrication effects

Operating Range Characterized The limitations encountered in Test 7 and 8 were the same as in Test 4 as the exact same configuration has been used. Three tests at 40 volts were conducted as described in the paragraph outlining the experimental procedures.

Characteristic motor curves speed and current-versus-load-torque curves are shown for two test cases in Figure 4-20, for three different kinds of oil fillings. The 'Enduro Oil' used in the reference test has the lowest viscosity with about 0.001596 $\frac{N\,s}{m^2}$ at 40^oC. The viscosity of the 'Carnation Oil' is unknown, but significantly higher than the viscosity of the 'Enduro Oil' (by observation), while the 'Power Up Lubricant' is even more viscous. The Power Up Lubricant

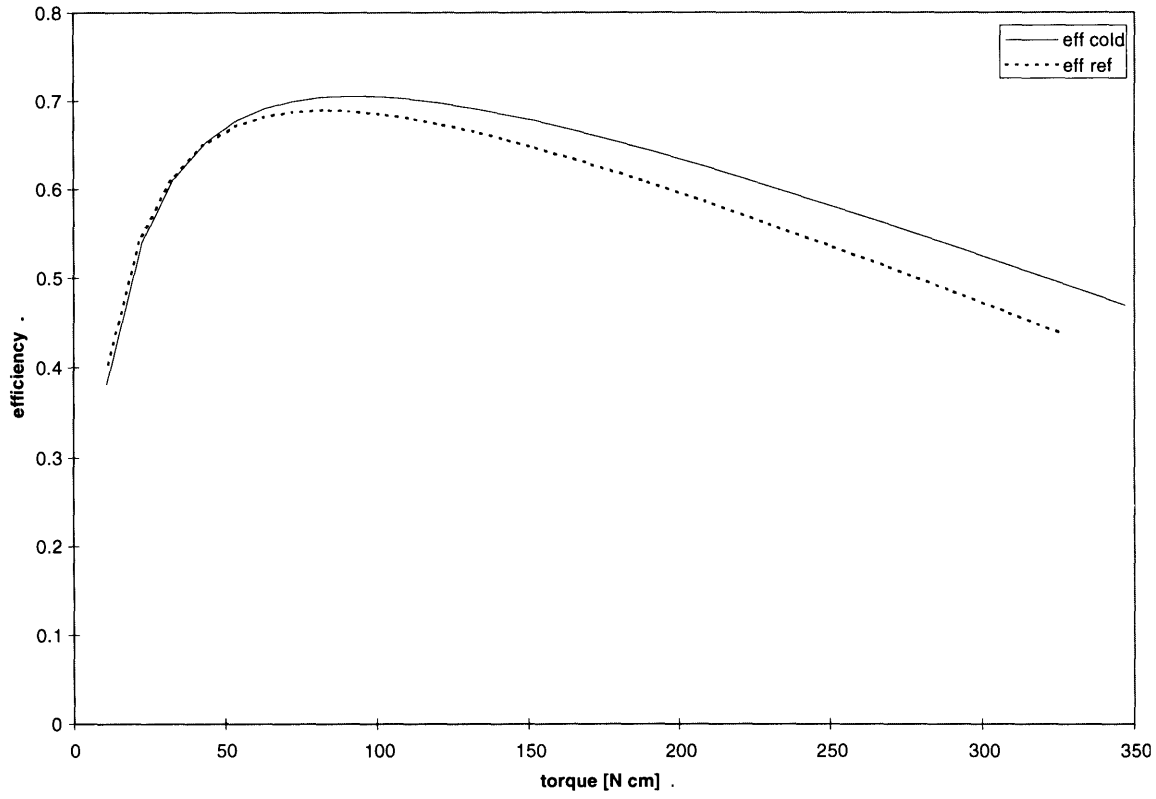

Figure 4-19: Efficiency Test 6 Compared to Reference Test at Room Temperature. The comparison of both efficiency curves shows the impact of a low-temperature environment on efficiency.

is an additive which is supposed to increase lubrication and is therefore expected to improve gearbox performance and to extend its life. It was mixed with the Carnation Oil in a ratio of 1:10.

The higher viscosity of the Carnation Oil and the Carnation Oil / Power Up Lubricant mixture are expected to increase speed-dependent losses and decrease load-torque-dependent losses decrease. The slope of both the current and speed-versus-load-torque curves is expected to decrease. This is observed in Figure 4-20. Unfortunately, the characteristic motor curves for the three tests are very close to each other and it is therefore hard to distinguish significant trends. Nevertheless, the slope of both current and speed-versus-load-torque curves in the Carnation Oil test case is decreased compared to the reference test. Additionally, the slope of both current and speed-versus-load-torque curves in the Carnation Oil / Power Up Lubricant

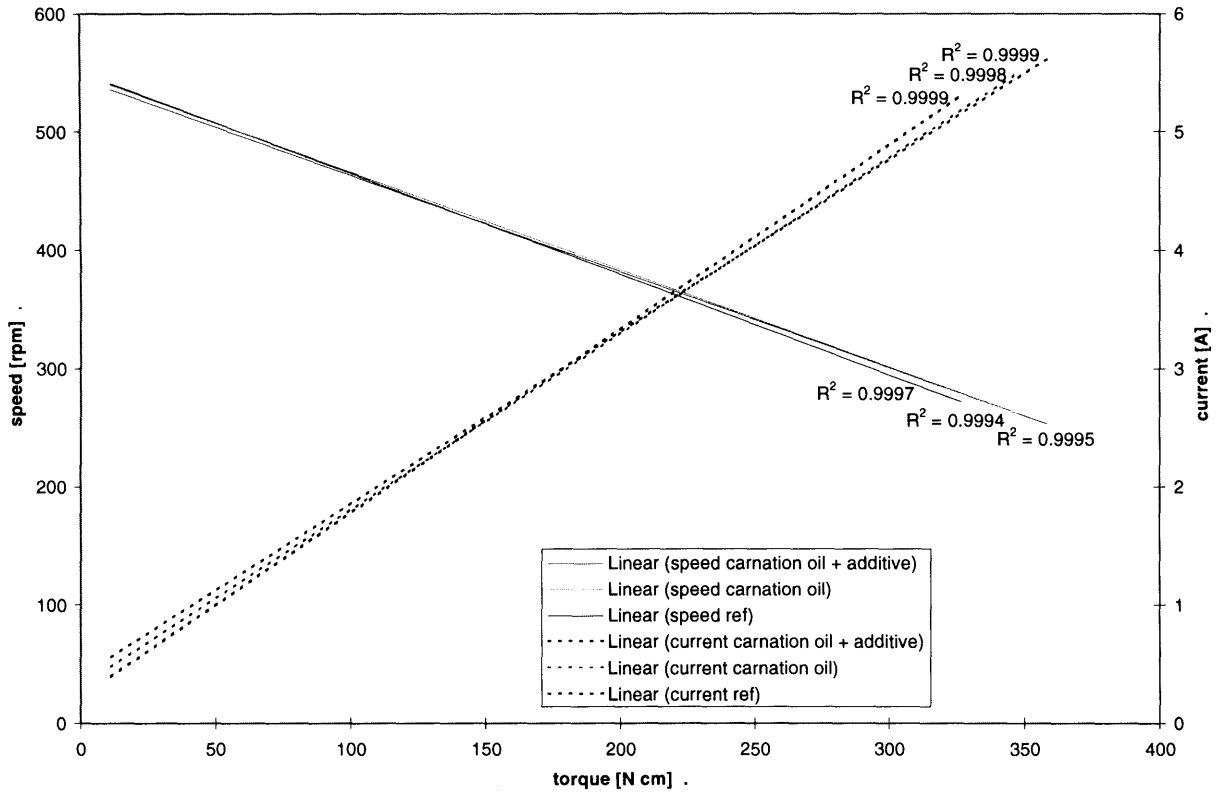

Figure 4-20: Motor Speed and Current for the Reference Test, Test 7 and Test 8. The reference test was conducted with an Enduro-Oil–filled thruster, in Test 7 Carnation Oil was employed while in Test 8 a Carnation Oil / Power Up Lubricant mixture with a ratio of 1/10 was used. Discrete data is not plotted to make it easier to distinguish between the curves. The comparison in this plot shows the impact of fill-fluids with different viscosity and lubrication properties.

mixture test case is decreased compared to the Carnation Oil test case.

The comparison of the efficiency curves in the next paragraph shows the trends discussed above more clearly.

Qualitative efficiency behavior Plotting the efficiency curves in the same graph (Figure 4-21) shows the effect of the different oil fillings on the thruster performance. The Carnation Oil results in an improved efficiency at higher load-torque, probably due to a better lubrication, whereas it decreases efficiency at low load-torque (high rotational-speed) presumably due to increased viscous losses. The Carnation Oil / Power Up Lubricant mixture decreases the thruster

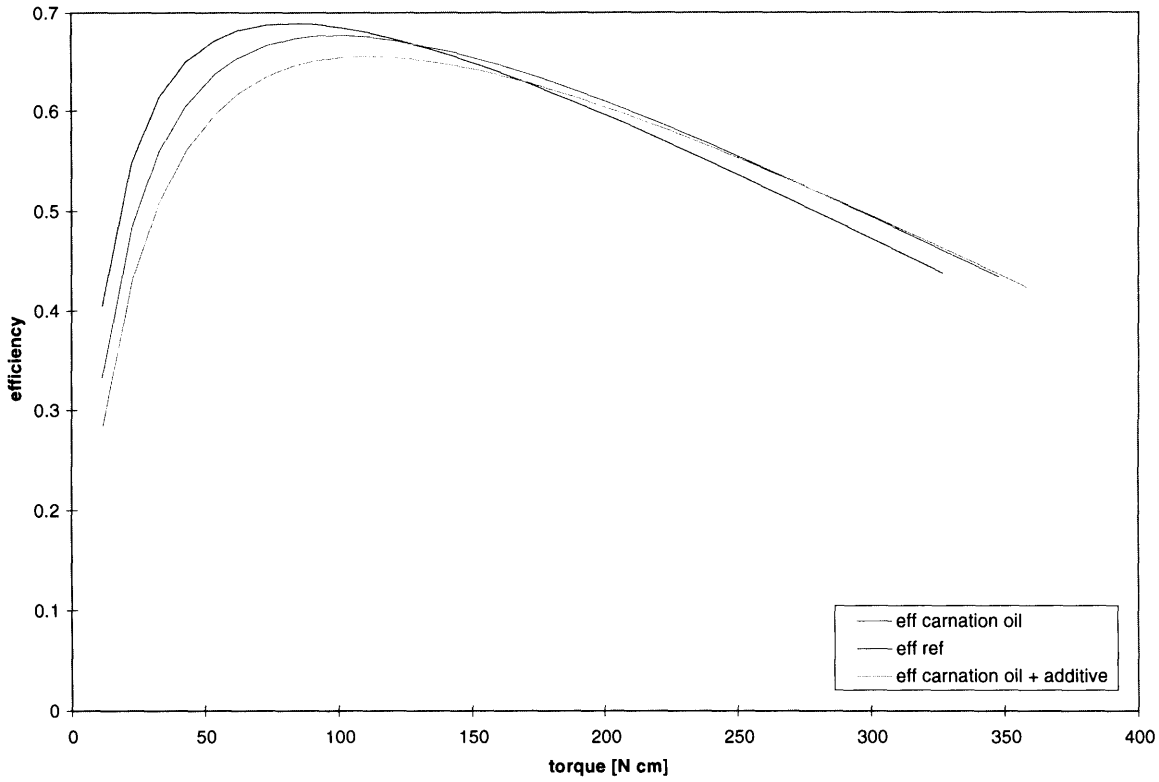

Figure 4-21: Efficiency Reference Test Compared to Test 7 and Test 8. The comparison of the efficiency curves for different thruster fill-fluids (Enduro Oil, Carnation Oil, and Carnation Oil/Power Up Lubricant mix) shows the impact of fill-fluids with different viscosity and lubrication properties on efficiency.

efficiency at low load-torque and improves it only slightly at high load-torque. An additional observation was that the gearbox noise was significantly reduced when the Carnation Oil / Power Up Lubricant mix was used. Therefore, Power Up Lubricant should not be used unless prolonging the life-span of the gearbox or lowering acoustic noise is a factor.

Torque losses The more viscous oils apparently provide an improved lubrication for higher load torques, but decrease efficiency at higher rotational-speed due to increased viscous losses. As the differences between the characteristic motor curves are small, the calculation of torque changes is not statistically significant. The previous qualitative discussion is therefore considered to be sufficient.

4.5.9 Test 9 - effect of Hall-effect sensor position

The position of the Hall-effect sensors can be varied by rotating the plastic disc they are mounted on. This leads to varying efficiencies shown in Figure 4-22. For the voltages tested (30 and 40 volts), the overall difference in efficiency due to the position of the Hall-effect senors amounted about 40%. The position of the Hall-effect sensors initially chosen by the manufacturer was close to the maximum efficiency. Nevertheless, the efficiency peak was found to be 2% higher than the efficiency achieved in the position chosen by the manufacturer.

For efficiency-sensitive applications it might be useful to check if the chosen position of the Hall-effect sensors is the most efficient one. This could be accomplished by exerting a constant load torque, for example, by applying a frictional force on the shaft, and then measuring the achieved speed, for example, by measuring the frequency of the Hall-effect sensor signal, while varying the position of the Hall-effect sensors. The position in which the maximum speed is achieved is the position of maximum efficiency.

4.6 Summary and Conclusions

The dynamometer tests revealed the influence of each component of the thruster on the overall system performance and allowed, together with the model of the electric motor, suppositions to be made about the dependence of the occurring torque losses on load torque and rotational speed. Furthermore, the influence of a low-temperature environment, of different thruster fill-fluids and the effect of the position of the Hall-effect sensor was investigated. The experimental error is small and the results are sufficiently repeatable and accurate.

The following list summarizes the experimentally-obtained efficiency-behavior of the thruster (Figure 4-14):

- There is one peak in the efficiency versus load torque curve, located in the low load-torque range.
- Below the peak, the efficiency drops rapidly for decreasing load torque, mainly due to viscous losses at high rotational-speed (viscous losses dominate).
- Above the peak, the efficiency decreases with increasing load torque, mainly due to I^2R

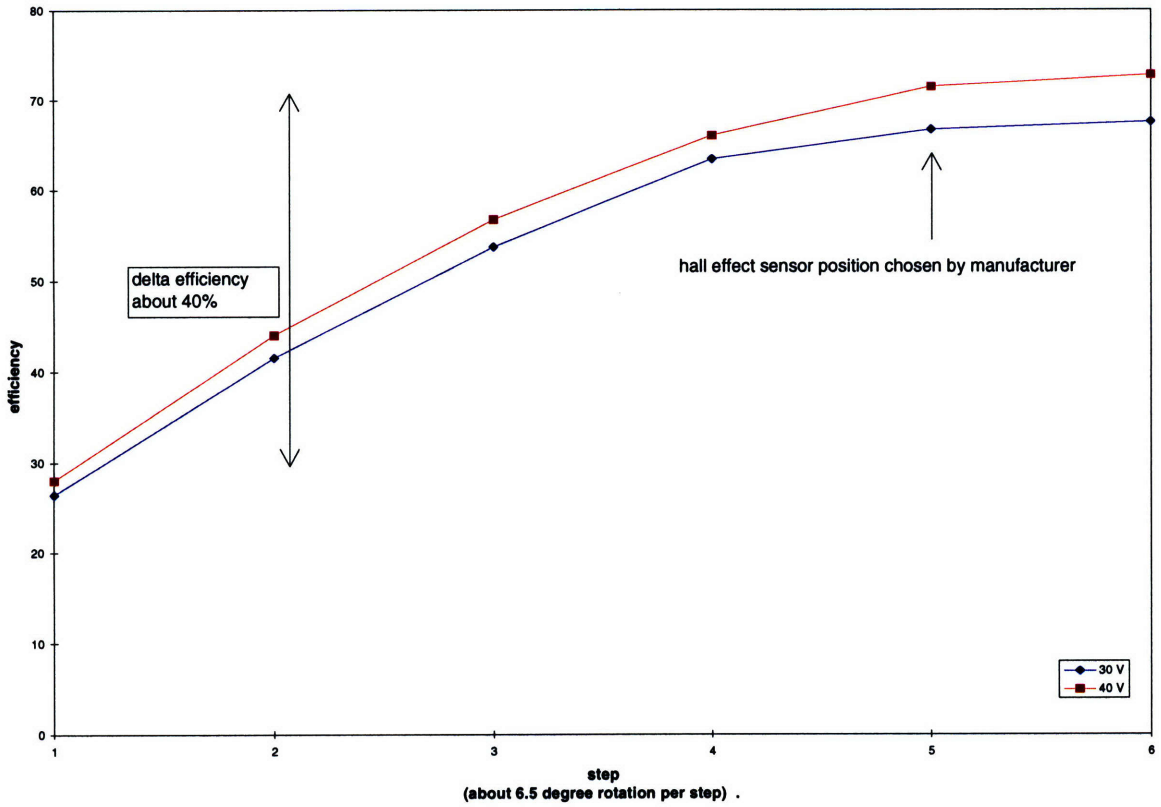

Figure 4-22: Effect of Hall-Effect Sensor Position. In this plot the effect of the Hall-effect-sensor position on motor efficiency is shown. The maximum difference in efficiency amounted to 40%.

losses, until the stall-torque is reached (electrical losses dominate). The behavior of the efficiency curve becomes increasingly linear for higher load-torques.

- Efficiency increases with increasing voltage. The magnitude of the efficiency increase is greatest at low voltages and decreases for higher voltages. For increasing voltages the efficiency peak is shifted to higher load torque.

- With increasing voltage, the slope of the efficiency curve becomes less, providing a decreased change of efficiency over load torque.

- The maximum measured efficiency of the thruster is about 71% and occurs for an applied voltage of 52 volts.

This behavior coincides with that seen in the model for the simulated not-steady-state

performance of the thruster. The following list summarizes briefly the findings of each conducted test:

- *Shaft-Seal* The torque loss due to the shaft-seal is essentially constant and amounts to approximately 1.2 Ncm.

- *Oil-Filling* Oil-filling the thruster improves its performance slightly at low rotational-speed, presumably due to the increased lubrication, and degrades its performance at high rotational-speed, presumably due to viscous losses. The influence of the oil-filling is not load-torque dependent when the thruster is operated without the gearbox.

- *Gearbox* The torque losses associated with the gearbox are linearly dependent on load torque and speed. If the thruster is oil-filled, the performance at higher load-torque (low speed) is superior than without oil. In contrast, the oil-filled thruster is inferior at low load-torque (high rotational-speed) than without oil. The behavior can be attributed to significant viscous losses at high speed and the effects of improved lubrication at high load-torque.

- *Temperature Effects* A low-temperature environment improves the thruster performance at high load-torque. This is due to the improved heat dissipation and the reduced winding resistance. At low load-torque the system performance is slightly worse than at room temperature, due to the increased viscosity of the oil-filling.

- *Viscosity and Lubrication effects* The three different oil-fillings tested differed in viscosity and lubrication quality. The more viscous the filling fluid, the better the performance of the thruster at high load-torque and the worse the performance at low load-torque. Power Up Lubricant should not be used unless it has other benefits, such as prolonging the life-span of the gearbox or to reduce gearbox noise. It only slightly increases performance at high load-torque while decreasing performance significantly at the efficiency peak.

- *Hall-effect-sensor position* The position of the Hall-effect sensors strongly influences the efficiency of the thruster. Variations in efficiency of 40% were observed for different Hall-effect-sensor positions. For the tested motor, the position chosen by the manufacturer

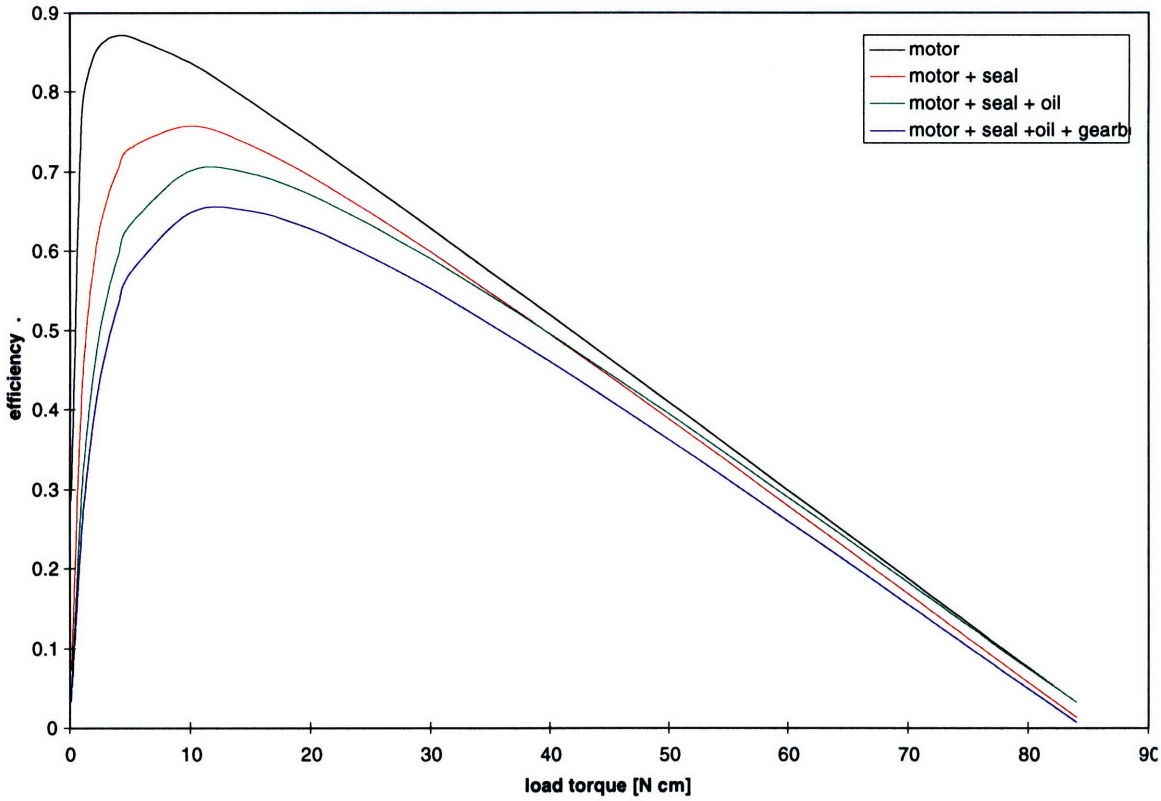

Figure 4-23: Efficiency for Different Thruster Configuarations at 28 volts. The experimentally determined charateristic motor-curves for the tested thruster configurations were extrapolated over the full motor-operating-range to show the influence of each thruster component in a direct comparison. It can be seen that the seal and the gearbox are mainly responsible for degrading the efficiency.

was close to the maximum achievable efficiency. Nevertheless, for efficiency sensitive applications, it is advisable to check the position of the Hall-effect sensor.

Figure 4-23 and Figure 4-24 show qualitatively and quantitatively how significant each thruster component worsens the system performance. In Figure 4-23 the efficiency curves for the thruster in different configurations at 28 volts are shown. The experimentally obtained characteristic motor curves have been extrapolated to higher and lower load torques than actually tested. The underlying assumption for this is that the linear nature of the motor-curves, observed within the tested range, extends outside the tested load torque range. The purpose is to show the probable influence of each thruster component over the full possible motor op-

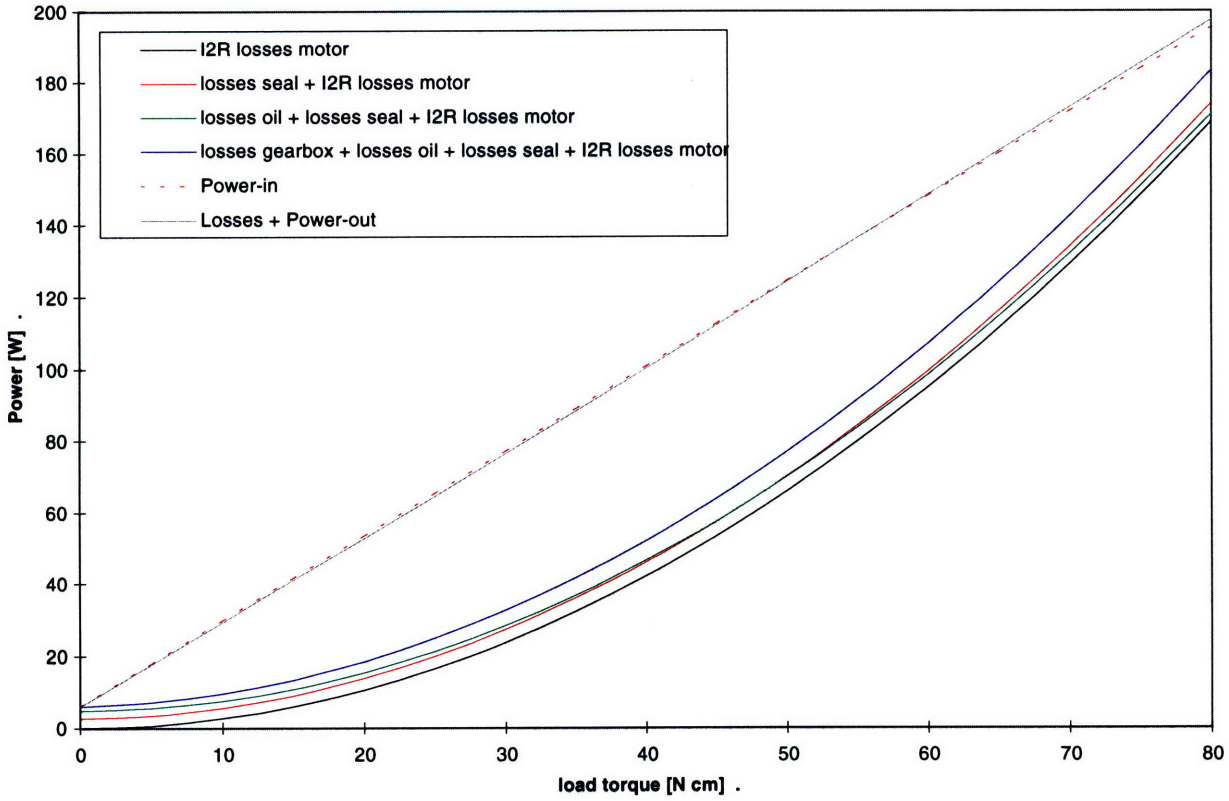

Figure 4-24: Power Balance at 28 volts. The torque losses due to each component of the thruster are expressed as power losses and added up, closing the balance between power-in the thruster and power-out. The major losses are electrical losses, followed by gearbox losses and losses in the seal.

erating range and to clarify its contribution. The difference between each curve in Figure 4-23 reveals the increase or decrease of efficiency due to an added component as a function of load torque.

In order to show quantitatively the power loss associated with each component, the power balance between power-in, losses, and power-out has been closed in Figure 4-24 for the 28 volts test case. The power balance is

$$P_{in} = P_{out} + P_{loss,\,motor} + P_{loss,\,seal} + P_{loss,\,oil} + P_{loss,\,gearbox}. \tag{4.7}$$

Figure 4-24 shows the absolute power loss due to each added component. The power loss

associated with a component consists of I^2R losses (due to the increased drawn current) as well as power losses due to the torque-loss inherent to the added component at the current rotational speed. Generally, for low load-torque, the power losses due to the torque loss are dominant, whereas at high load-torque I^2R losses due to the increased drawn current are dominant.

The first black line in Figure 4-24 represents the I^2R losses encountered in the case when only the motor is tested. Added on top of this is the power loss due to the shaft-seal, represented by a red line. The power loss due to the shaft-seal increases linearly over load torque. The green line denotes the power loss (and gain) due to the oil-filling. At low load-torque (high rotational-speed) the oil-filling causes a power loss, whereas at high load-torque (low rotational-speed) the oil-filling causes a power gain. The power loss due to the oil-filling decreases exponentially (torque loss decreases linear) over load torque. The blue line represents the power loss inherent to the gearbox, added on top of the previous losses. The power loss due to the gearbox increases exponentially (torque loss increases linear) over load torque. The grey line is the sum of all power losses and power-out and should be the same as the dotted red line, which represents power-in. Both lines are nearly identical, which in turn indicates a low experimental error and a precise identification of the power loss inherent to each thruster component.

To conclude this discussion above, it should be noted that the shaft-seal and the gearbox cause significant losses, whereas the oil-filling causes only a minor loss or even improves the thruster performance at low speed. However, electrical losses are mostly dominant and increase exponentially over load torque, showing the need to operate the thruster in a regime where electrical losses are small.

Chapter 5

Verification of the Computational Model

In this chapter the computer program modelling the thruster, presented in Chapter 3, is verified using the experimental results discussed in Chapter 5. As the thruster was not tested at thermal steady-state, but was always kept close to room temperature by giving it time to cool down between measurements, only the first stage of the computer program, predicting the non-thermal-steady-state performance of the thruster, can be compared to the experimental data. The thruster was not tested at thermal steady-state for three reasons. First, the amount of time needed to assure a thermal steady-state operating condition is infeasible long if a complete set of motor performance curves is desired. Second, the danger of damaging the thruster is significant. Finally, it significantly simplified the comparison of various thruster configurations.

By setting the counter of the loop enclosing the first stage of the computer program to one, and by omitting the second stage calculating the altered motor constants due to the temperature rise encountered during thermal steady-state operation, the performance of the thruster omitting steady-state thermal effects can be calculated. However, the first stage of the computer program is the most important one as in here the concepts modelling the different thruster components are joined together. Therefore, an agreement between the first stage of the computer program and the experimental results would proof the validity of the applied concepts.

Parameter	Value	Description
E	28 V	applied Voltage
R	2.33 ohms	stator resistance
R_T	3.75 ohms	overall resistance, including wiring and controller
K_T	0.12 $\frac{N\,m}{A}$	torque constant
K_E	0.12 $\frac{V}{rad/s}$	back emf constant
T_F	4 10^{-3} N m	motor friction torque
T_L	0-200 N cm	load torque range, in terms motor shaft torque
T	20 C^o	ambient temperature
T_{max}	155 c^o	max winding temperature
D_1	30.4292 mm	rotor diameter
D_2	31.1658 mm	stator diameter
L	62 mm	length of rotor/stator
G	5.54	gearbox speed reduction ratio
T_1	26^oC	temperature of known viscosity of fill-fluid
μ	24.84 10^{-4} $\frac{N\,s}{m^2}$	viscosity of fill-fluid at two temperatures

Table 5.1: Thruster Parameters

The second stage of the computer program is needed to simulate thermal steady-state performance of the thruster. The concepts to model thermal steady-state performance are purely empirical as discussed in Chapter 3 and the outcome of the calculation is dependent on the estimation of the thermal impedance of the thruster in its operating environment. Nevertheless, it is expected that stage two provides reasonable estimates. In contrast, the concepts introduced in stage one are mostly the representation of physical principles.

The characteristic motor performance curves predicted by the first stage of the computational model without thermal effects are compared below to the experimentally determined characteristic motor curves obtained by the dynamometer tests. For the speed-and current-versus-load-torque, the discrete experimental data and the interpolated curve are plotted. Different thruster configurations and the resulting model predictions are compared. The continuously used thruster parameters are summarized in Table 5.1.

Motor In Figure 5-1, the experimentally obtained characteristic motor curves are compared to the curves reproduced by the part of the computer program simulating only the electric motor. By visual inspection it can be seen that both current-versus-load-torque curves coincide. The slope of the theoretical speed-versus-load-torque curve is slightly higher, which indicates an additional speed-dependent loss not included in the computational model. A candidate is

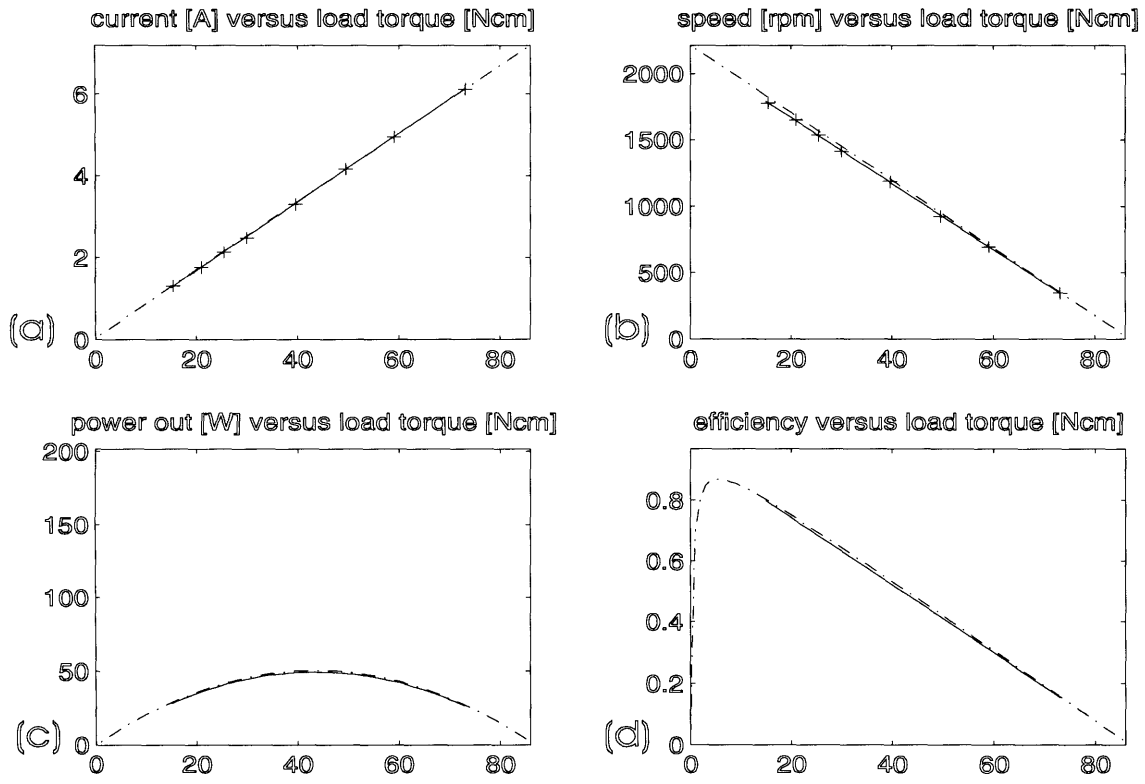

Figure 5-1: Comparison Model and Experimental Results: Motor (x: discrete data; solid line: least squares curve fit; dashed-dotted line: model estimation)

the loss in the ball-bearings or an imprecise damping coefficient (DF). Nevertheless, the model prediction and the experimental results show good agreement.

Motor + Seal Figure 5-2 shows the same comparison after the shaft-seal has been added to the thruster configuration. The same slight difference in the speed-versus-load-torque curve is observable as well as the good agreement between both current-versus-load-torque curves. A good agreement could be expected as the influence of the shaft-seal has been determined experimentally and was then incorporated in the computational model.

Motor + Seal + Oil Figure 5-3 displays the comparison between model prediction and experimental results for the motor + seal + oil case. The viscosity of the fill-fluid has been estimated for a temperature of 26^oC as a slight warming of the thruster over the duration of

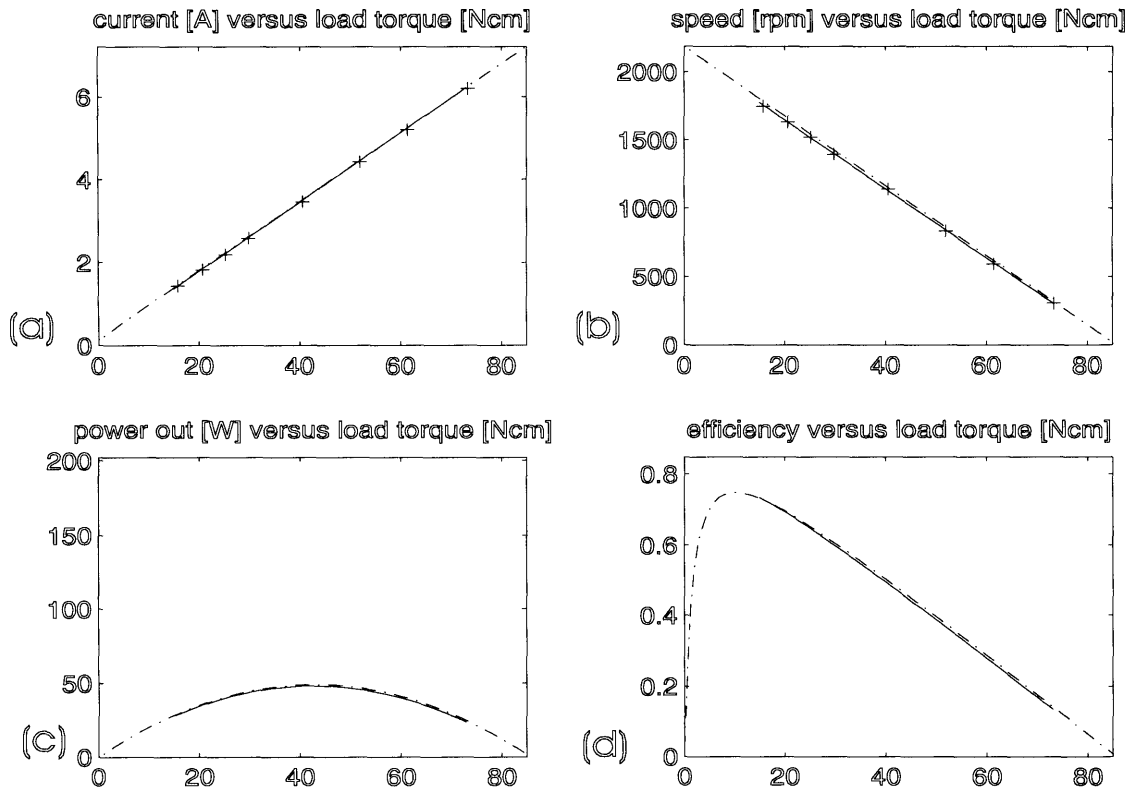

Figure 5-2: Comparison Model and Experimental Results: Motor + Seal (x: discrete data; solid line: least squares curve fit; dashed-dotted line: computational model estimation)

the tests could not be prevented. The estimation of the fill fluid viscosity was performed as described in Chapter 3.4. The agreement between model prediction and experimental results is good. However, the model overestimates the peak efficiency slightly, probably due to an inaccurate value for the fill-fluid viscosity.

Motor + Seal + Oil + Gearbox In Figure 5-4, the comparison between the model prediction and the experimental results has been extended by the influence of the gearbox. By visual inspection, it can be seen that the slope of the theoretical current-and speed-versus-load-torque curve is increased compared to the experimental result. This causes the model to overestimate the thruster efficiency in the low load torque range and to underestimate the efficiency for high load-torques. This is probably due to different reasons. First, the gearbox-efficiencies used to obtain the theoretical continuous gearbox-efficiency estimates are 'worst case' values and there-

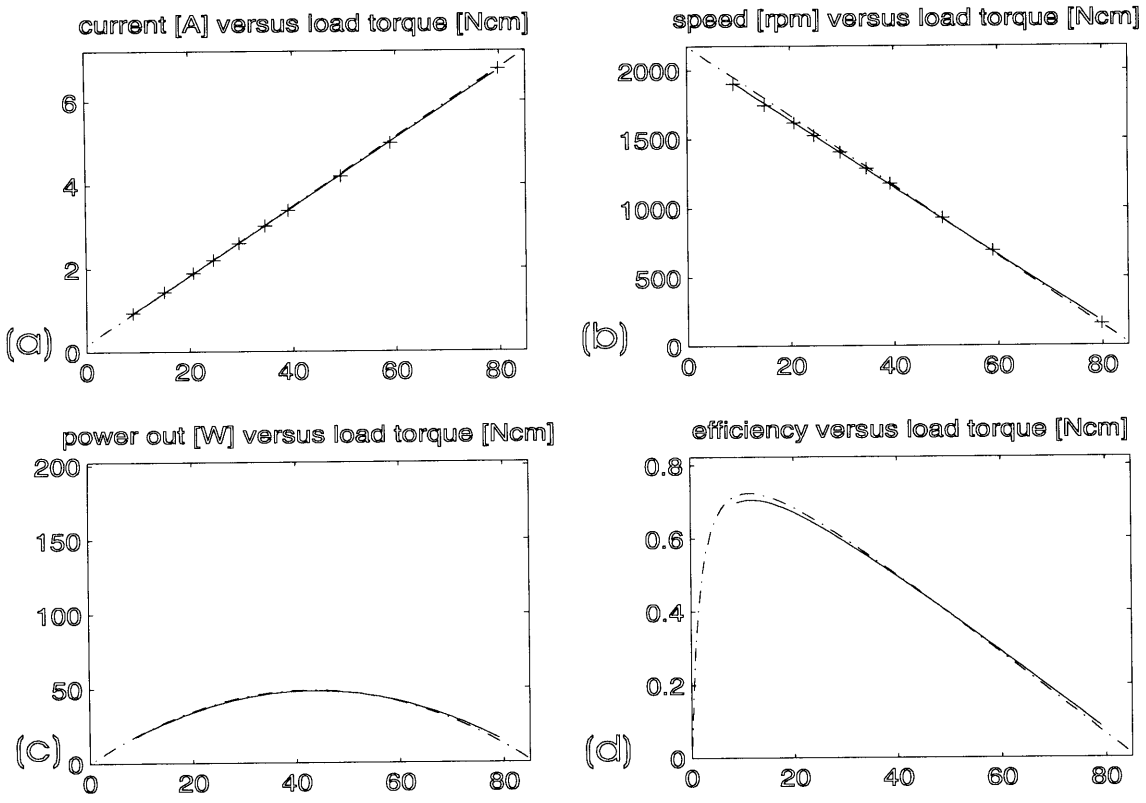

Figure 5-3: Comparison Model and Experimental Results: Motor + Seal + Oil (x: discrete data; solid line: least squares curve fit; dashed-dotted line: computational model estimation)

fore overestimate the real torque loss associated with the gearbox. Furthermore, the effects of lubrication, which increase gearbox performance, are not included in the computational model. In addition, viscous losses within the gearbox are not taken into account. Nevertheless, the model still shows general agreement with the experimental results.

Low Temperature Figure 5-5 shows the comparison between the model prediction and the experimental results for the test conducted at low temperature ($3°C$). The applied voltage in this case was 40V and the fill-fluid viscosity obtained from the computer program is 0.0071 $\frac{N\,s}{m^2}$. The temperature-altered motor-constants were calculated for a temperature of $3°C$. The torque constant increased from 0.12 to 0.1205 $\frac{N\,m}{A}$. The motor resistance R_T decreased from 3.75 to 3.7 ohms. The thruster configuration in this run is the same as in the run described before. Again, as in the previous run, it can be seen that the slope of the theoretical current-and

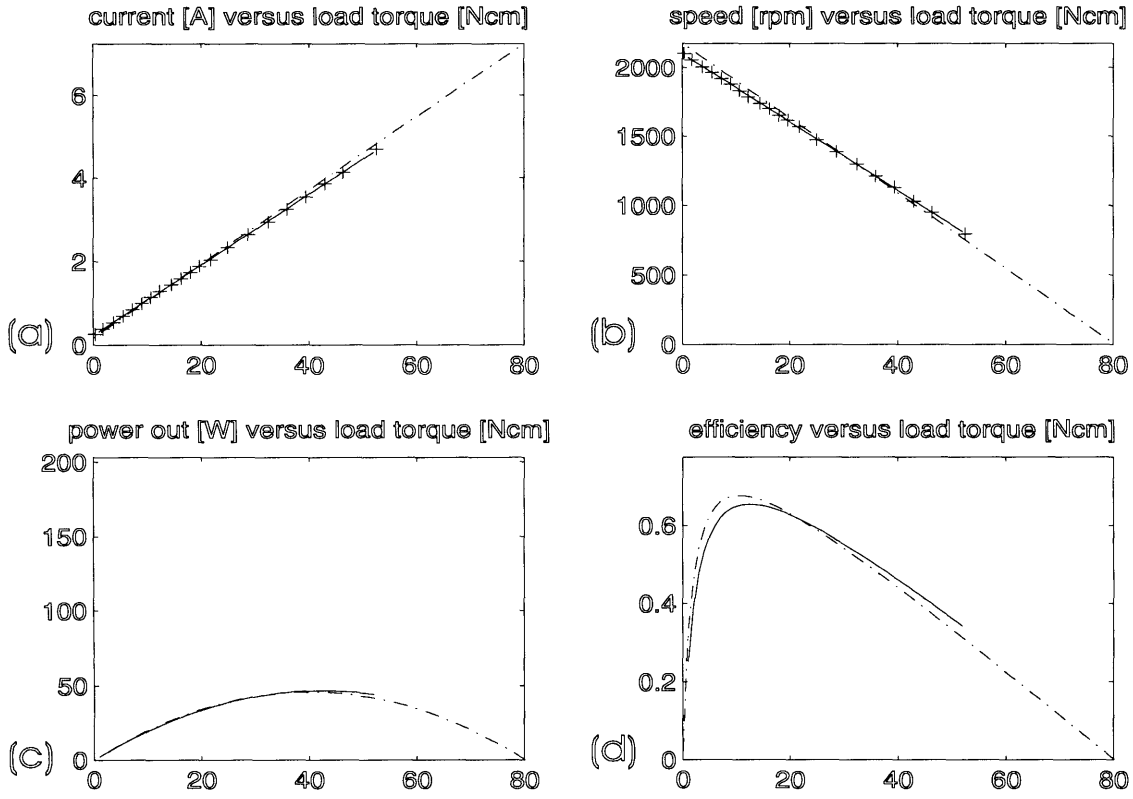

Figure 5-4: Comparison Model and Experimental Results: Motor + Seal + Oil + Gearbox (x: discrete data; solid line: least squares curve fit; dashed-dotted line: computational model estimation)

speed-versus-load-torque curve is increased compared to the experimental result.

Conclusion The discussion above suggests that the computational model is capable of reproducing the experimentally obtained thruster performance characteristics. The maximum error in the vicinity of the efficiency peak for the complete thruster is approximately 4%. If the thruster units consists of components similar to Odyssey II's thruster components, good results can be obtained for thermally controlled conditions. It can be expected that for thermal steady-state conditions, reasonable estimates of the thruster performance are obtained.

Recall that for the thruster design the operating range close to the efficiency peak is desirable. The important quantities are power-out and efficiency. Around the efficiency peak, the difference between the thermal steady-state and the values obtained under thermally controlled

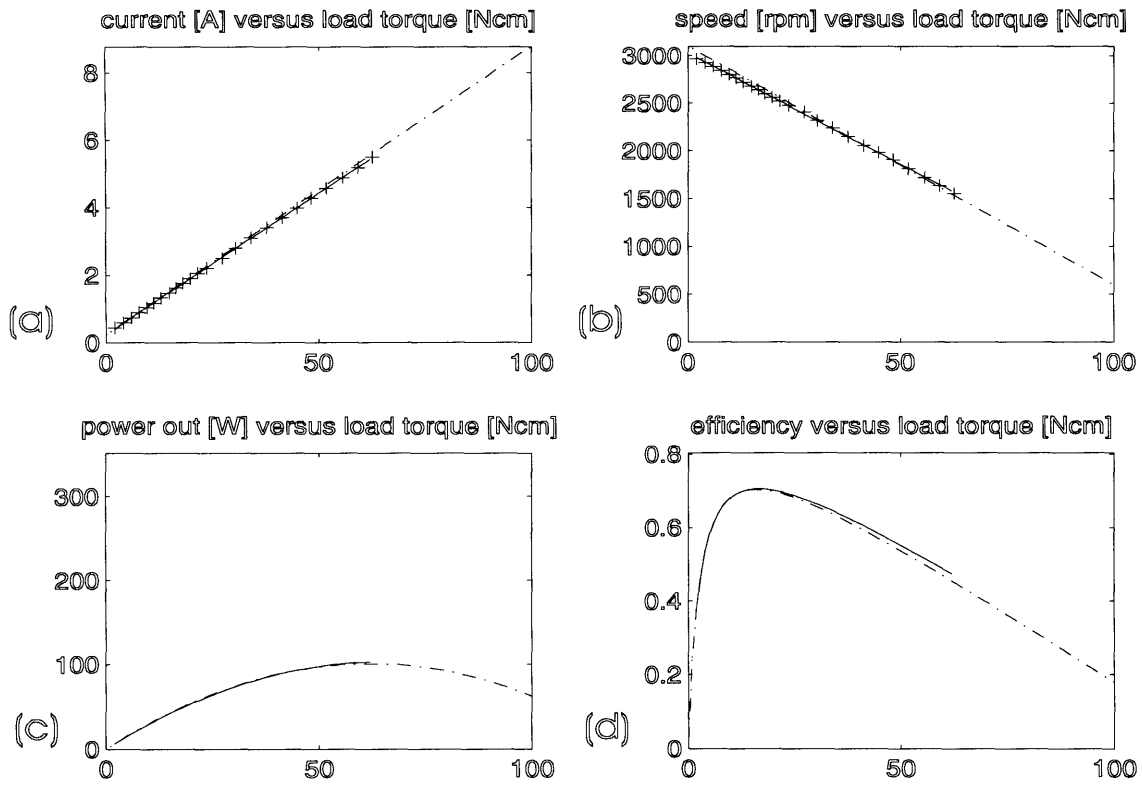

Figure 5-5: Comparison Model and Experimental Results: Low Temperature (x: discrete data; solid line: least squares curve fit; dashed-dotted line: computational model estimation)

conditions is small as only few I^2R losses occur, which are mainly responsible for the heating of the thruster at high load-torque. This property is indicated in Figure 3-6. Therefore, the computer program will still give good estimates for the thermal steady-state thruster performance within the design range of interest, even if the estimate for the thermal impedance is imprecise.

Chapter 6

Evaluation of Design Options

In this chapter, Odyssey II is used as an example for the design process and each of the steps outlined in Chapter 2 is applied. The different propulsor options discussed are mated to the thrusters, and the possible system performance is assessed. The outcome of this process is the optimum propulsion system for Odyssey II. The performance potential of alternative design solutions is also examined.

6.1 Design Example Odyssey

Required Thrust and Power Odyssey II's hull has been taken from a form family of extensively tested hull forms. Therefore, the drag coefficient C_D with respect to the projected area of the body A is known to be $C_D = 0.07$ [5]. Odyssey II is capable of carrying various pay-loads, which partly afford hull modifications. Sensors, acoustic devices or other tools may be placed outside the streamlined hull and therefore increase the drag. Assuming that the drag increases up to 30% due to these modifications, the drag coefficient C_D varies between

$$C_D = 0.07 - 0.091.$$

The diameter of the vehicle is 0.58 m, which results in a projected area of 0.26 m^2. For the vehicle design speed of 3 knots and seawater ($\rho = 1024\ \frac{kg}{m^3}$) the expected vehicle drag is

according to Equation 6.1 between

$$R = 23\ N - 30\ N.$$

The propulsive power P_{prop} required to achieve the design speed of three knots is 35.5 Watts and 46.3 Watts, respectively. This drag value does not yet include the effects of the propulsor.

As efficiency is the dominant design specification, the propulsion system should operate in the vicinity of its efficiency peak most of the mission time. The optimum propeller design is found for a specified vehicle speed, which determines the inflow velocity, and the required thrust to achieve this speed. Changes in thrust and vehicle speed with respect to the design point degrade the propulsive efficiency. Additionally, the motor controller should be operated at its maximum setting at the design point as it otherwise chops the applied voltage to control the thruster output. The motor efficiency is highest for high voltages. Therefore, the design speed should be the maximum vehicle speed.

To design the optimum propulsor, an intermediate drag and required-power value is chosen. It is assumed that the encountered C_D value is increased by 15%, resulting in a vehicle drag of 26.5 N and a required propulsive power of 41 Watts, not including the effects of the propulsor on the vehicle drag. This choice implies the following consequences. If the vehicle drag is increased more than 15%, the design speed is not achievable as the motor controller is already operated at its maximum setting (for a 30% increase in drag, the achievable speed would be 2.83 knots). If the vehicle drag is increased less than 15%, the vehicle exceeds the design speed if the motor controller is kept at its maximum setting, or the speed is adjusted by means of the motor controller.

Preliminary Drive Power Estimation and Motor Selection Assuming an actuator disc propulsor with the diameter of the vehicle, the ideal propulsor efficiency according to Equation 2.2 is 98% at 3 knots. The actuator-disc representation of a propeller does not include rotational velocities and viscous losses. Therefore, the real propeller efficiency is significantly lower than the ideal efficiency. Nevertheless, this calculation shows that the given operating conditions make it possible to design a highly-efficient propulsor.

To estimate the influence of the propulsor on the vehicle drag, the thrust deduction co-

efficient t has to be determined. The tailcone angle of Odyssey II is about $^o30$. The thrust deduction coefficient can then be estimated using reference [9] to be about 0.075. Thus, the required thrust, including the increased drag due to the presence of the propulsor, is according to Equation 2.3, 28.6 N. This corresponds to a required propulsive-power of 44 Watts to maintain the design speed of 3 knots.

Estimating the power requirement for the Odyssey II motor using Equation 2.4, with P_{prop} = 44 Watts, $\eta_P = 0.9$ and $\eta_G = 0.92$, yields a required motor shaft-power of approximately 54 Watts. The value of η_P is not the ideal efficiency calculated by the actuator model, but a reduced efficiency based on common sense and experience.

To to choose between candidate motors the computational model is used. The thruster is assumed to be oil filled, to have a shaft seal and to operate at 3^oC with a supply voltage of 48 volts. A gearbox is not included as it was already included in the estimation of the required motor-power. The evaluated sample motors are Pittman Elcom Series 5113 brushless DC motors with different windings. Figure 6-1 shows the calculated steady-state power-out and efficiency of the thruster for different motor-windings.

From Figure 6-1 it can be seen that winding-option number three with a resistance of 2.33 ohms, represented by the green curve, yields the highest efficiency for the estimated required power-out level of 54 Watts. The selected motor is therefore a Pittman Elcom Series 5113 brushless DC motors with winding-choice number three.

The Inflow Field For Odyssey II's polyethylene surface and submerged operating conditions a critical Reynolds number of $R = 7 * 10^5$ is assumed [27]. This causes the flow to change from laminar to turbulent after approximately 0.51 m. The overall length of Odyssey II's stretched surface is 2.3 m.

The thickness of the laminar boundary-layer can be estimated using Equation 2.6. For $x = 0.51\ m$ the thickness of the laminar boundary-layer is $\delta = 3.007\ mm$. The fluid velocity U is assumed to be the vehicle velocity of 3 knots. The turbulent boundary-layer will extend form x coordinate 0.51 m to 2.3 m of the hull in the direction of the flow. The thickness of the turbulent boundary-layer with a length of 1.79 m can be estimated using Equation 2.6 and is found to be $\delta = 35.27\ mm$.

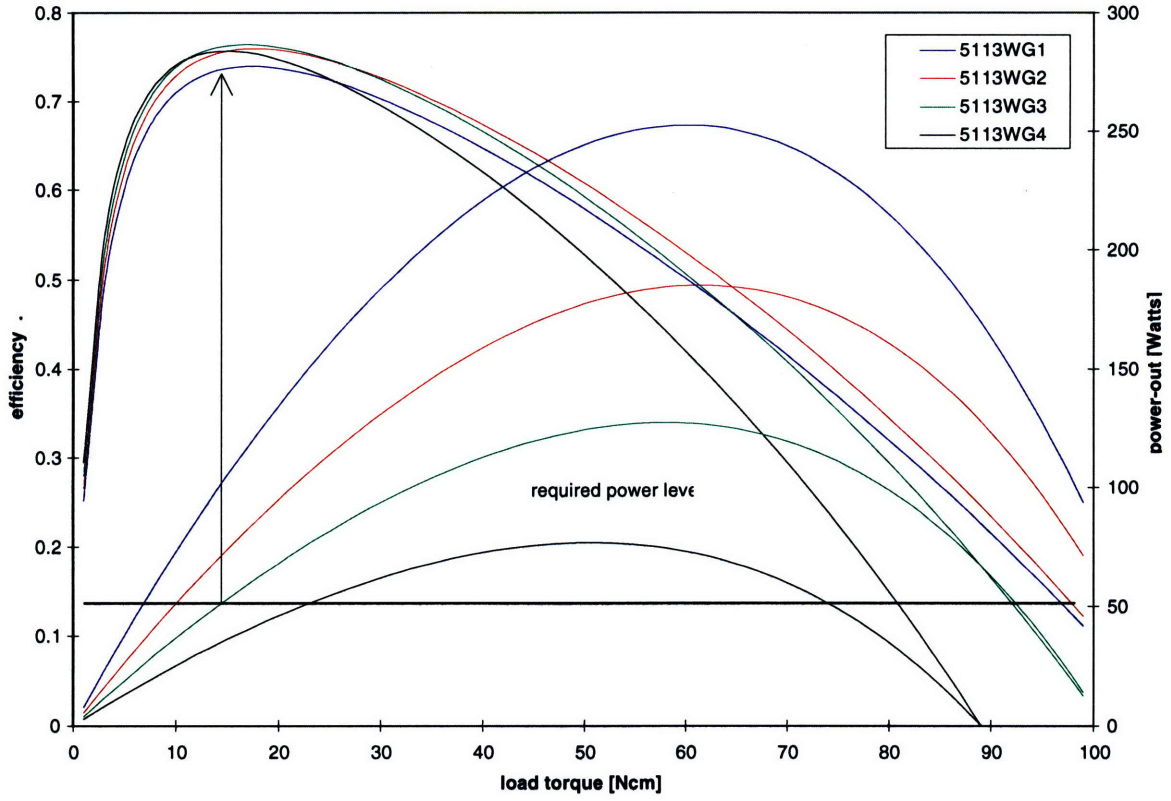

Figure 6-1: Power-Out and Efficiency for Candidate Motors. The assessed motors have different windings but the same geometrical properties. The motor with winding-option number three (green curve) provides the required power-output at its efficiency peak and is therefore chosen for the Odyssey II thruster.

The total thickness of the boundary-layer can be estimated by taking the sum of the laminar and turbulent boundary-layer thickness and is

$$\delta_{total} = 38.285\ mm.$$

Compared to the expected dimensions of the propulsor of about 300 mm, this value is small and therefore it can be assumed that the wake has no significant influence on the propeller design and that the inflow field is thus uniform. Recall that the increase in fluid velocity over the boundary-layer is exponential and that therefore only about $\frac{1}{3}$ of the boundary-layer has a significant lower speed than the free flow.

Vehicle	
vehicle speed	3 knots
required thrust	28.6 N
required propulsive power	44 Watts
Motor	
model	Pittman Elcom Series 5113
stator resistance	2.33 ohm
torque constant	0.12 $\frac{N\,m}{A}$
back emf constant	0.12 $\frac{V}{rad/s}$
thermal impedance	1 $\frac{C^o}{W}$
ambient temperature	3 C^o

Table 6.1: Vehicle Design and Motor Parameters

6.2 Performance Predictions

Having collected the required design parameters, the sections below apply steps 5 and 6 of Figure 2-1 to the Odyssey II design. Propeller based propulsion systems and their maximum expected efficiency are assessed using MIT-PLL and the computational thruster model. A general quantitative discussion of propulsor options for small AUVs is not possible, as the optimum propulsion solution is much dependent on individual properties of the vehicle. The discussion below gives an insight to the possible performance of different classes of propulsors. The required design parameters collected in the previous paragraphs are summarized in Table 6.1.

MIT-PLL was run with its default settings, which included wake alignment, an automatic estimation of the blade drag coefficient based on a NACA 66 thickness form, and chord length optimization based on cavitation constraints and considerations regarding viscous effects. The maximum possible propeller diameter was assumed to be 0.67 m.

6.2.1 Single Propeller

This section investigates the performance of a single-propeller-based propulsion-system. First, the optimum propeller for the required thrust and speed was designed. For the single-screw propeller the variable design parameters are propeller rpm, diameter and number of blades. This is a design space of manageable size.

The optimum propeller with two, three and four blades was found by iterating over a range

	2 Blades	3 Blades	4 Blades
efficiency	*88.9*	*89.7*	*89.3*
rpm	95	85	80
diameter [ft]	2.2	2.2	2.1
torque [Ncm]	500	554	591
requ. power [W]	49.96	49.21	49.18

Table 6.2: Optimum Single-Screw-Propeller

of diameters and rpms. The iteration procedure is to pick a first guess for the diameter and then to determine the optimum rpm and efficiency for this diameter. Afterwards, the diameter is either increased or decreased and the optimum rpm is determined again. Recall that there is one optimum rpm and diameter for a given vehicle speed, number of blades, inflow field and required thrust. Therefore, efficiency either increases or decreases by varying rpm or diameter, giving the direction for the next iteration.

The obtained results are summarized in Table 6.2. The highest efficiency is achieved with the three-bladed propeller. The efficiencies are similar and depend only slightly on the number of blades. The more blades, the lower is the rpm and the higher the torque.

To estimate the system performance, the optimum propellers from Table 6.2 are matched to the thruster by means of a gearbox. An example for this procedure is given for the two-bladed propeller according to the discussion in Section 2.3.5.

The required gearbox-reduction ratio to match thruster and propeller was determined using a short MATLAB script file. The user inputs the required power as well as the required torque of the propulsor. The program then uses the estimated performance curves from the thruster model and picks the corresponding operating-point of the thruster on the power-out curve. The ratio of the torque produced by the thruster at this operating point and the required propeller torque yields the gearbox reduction-ratio. For the first iteration, assuming no gearbox, a steady-state efficiency of 76.13% of the thruster for the required power-out of 49.96 Watts was found right on the efficiency peak of the efficiency curve. The required gearbox reduction-ratio is 35.7. Rerunning the thruster model now with a gearbox reduction-ratio of 35.7 led to a thruster efficiency of 66.9% including the gearbox efficiency of 87.21%. The operating point is still located on the efficiency peak, shifted only slightly to higher torque due to the losses in the gearbox. The next iteration yielded a gearbox reduction-ratio of 35 compared to

	2 Blades	3 Blades	4 Blades
thruster eff.	*66.98*	*66.71*	*66.53*
gearbox ratio	35	39	41.5
gearbox eff.	87.21	86.84	86.6
system efficiency	59.47	59.83	59.2

Table 6.3: System Efficiency Optimum Single-Screw-Propeller

120 rpm	2 Blades	3 Blades	4 Blades
propeller efficiency	88.4	88.2	88.4
diameter [ft]	2	1.9	1.7
thruster eff.	67.55	67.55	67.55
gearbox ratio	28	28	28
gearbox eff	87.96	87.96	87.96
system eff	*59.71*	*59.57*	*59.71*

Table 6.4: Optimum Single-Screw-Propeller at 120 rpm

35.7 calculated in the first iteration. It can be seen, that the influence of the gearbox on the power-out operating-point is small and that the iterations converge rapidly.

The result of the previous calculations is that the propulsion system efficiency, calculated from the two bladed propeller efficiency of 88.9%, and the thruster efficiency of 66.9%, is 59.47%. The system efficiencies for the three cases are summarized in Table 6.3. It can be seen that the three-bladed propeller is the best choice despite the fact that it operates at lower rpm and requires a higher gearbox reduction-ratio than the two-bladed propeller. Recall that the efficiency of the gearbox is an exponential function of the gear-reduction ratio and therefore changes in the lower gear-reduction range have a higher impact than those in the higher gearbox-reduction range. Therefore, the change from 35:1 to 39:1 in the gearbox reduction-ratio has a relatively slight effect on the thruster performance and the advantage in propulsive efficiency of the 3 bladed propeller prevails the disadvantage in gearbox efficiency.

To determine the effect of increased propeller rpm on system efficiency, the propeller rate of rotation was increased in steps. The previous rates of rotation were around 90 rpm; the next chosen rate of rotation was 120 rpm. For each rate of rotation, the optimum propeller was found by varying the diameter. Afterwards, the system efficiencies were determined as described above. The results are summarized in Tables 6.4 to 6.10.

The calculated efficiencies of the thruster, the propeller and the system for the different

170 rpm	2 Blades	3 Blades	4 Blades
propeller efficiency	87.1	87	86.8
diameter [ft]	1.7	1.6	1.5
thruster eff.	68.4	68.44	68.44
gearbox ratio	20	19.7	19.7
gearbox eff	89.1	89.16	89.16
system eff	*59.57*	*59.54*	*59.4*

Table 6.5: Optimum Single-Screw-Propeller at 170 rpm

250 rpm	2 Blades	3 Blades	4 Blades
propeller efficiency	85.2	85.3	84.9
diameter [ft]	1.4	1.3	1.2
thruster eff.	69.47	69.47	69.47
gearbox ratio	13.2	13.2	13.2
gearbox eff	90.54	90.45	90.45
system eff	*59.18*	*59.25*	*58.98*

Table 6.6: Optimum Single-Screw-Propeller at 250 rpm

350 rpm	2 Blades	3 Blades	4 Blades
propeller efficiency	83.2	83	82.5
diameter [ft]	1.2	1.1	1
thruster eff.	70.33	70.33	70.33
gearbox ratio	9.5	9.5	9.5
gearbox eff	91.7	91.7	91.7
system eff	*58.51*	*58.37*	*58.02*

Table 6.7: Optimum Single-Screw-Propeller at 350 rpm

550 rpm	2 Blades	3 Blades	4 Blades
propeller efficiency	79.6	79.6	78.8
diameter [ft]	0.9	0.9	0.8
thruster eff.	71.53	71.53	71.53
gearbox ratio	6	6	6
gearbox eff	93.3	93.3	93.3
system eff	*56.93*	*56.93*	*56.36*

Table 6.8: Optimum Single-Screw-Propeller at 550 rpm

1000 rpm	2 Blades	3 Blades	4 Blades
propeller efficiency	73.3	72.6	72.2
diameter [ft]	0.7	0.7	0.6
thruster eff.	73.17	73.03	73.03
gearbox ratio	3.2	3.3	3.3
gearbox eff	95.62	95.51	95.51
system eff	*53.63*	*53.01*	*52.72*

Table 6.9: Optimum Single-Screw-Propeller at 1000 rpm

2000 rpm	2 Blades	3 Blades	4 Blades
propeller efficiency	64.8	63.2	62.2
diameter [ft]	0.5	0.5	0.4
thruster eff.	74.72	74.53	74.48
gearbox ratio	1.6	1.61	1.6
gearbox eff	98.2	98.2	98.2
system eff	*48.41*	*47.1*	*46.32*

Table 6.10: Optimum Single-Screw-Propeller at 2000 rpm

rates of rotation and number of blades are compared in Figure 6-2. The black lines represent the efficiencies of the optimum propellers dependent on their rates of rotation. The green line indicates the efficiency of the thruster. The red lines show overall system efficiencies, which are the product of the thruster and propeller efficiencies.

Some conclusions can be drawn from the data presented in Tables 6.4 to 6.10 and their illustration in Figure 6-2. First it can be seen that the number of blades has only a minor influence on the system performance. Furthermore, it is apparent that the system performance achieved with the optimum propeller design and the high gearbox-reduction-ratio is not exceeded. Nevertheless, the system efficiency curve is relatively flat up to about 250 rpm, offering efficiencies close to the optimum efficiency. High propeller efficiency is sustained over a broad rpm range as the propeller is only slightly loaded. An interesting alternative to the optimum propeller (Table 6.2) operating with three blades and a 39:1 gearbox (85 rpm shaft speed) at a system efficiency of 59.83% is the three bladed propeller operating with a 13.2:1 gearbox (250 rpm shaft speed) at a system efficiency of 59.25%. The advantage of this solution is the reduced gearbox reduction-ratio from 39 to 13.2 (smaller gearbox), and the reduced propeller diameter from 2.2 feet to 1.3 feet (simplifying the handling of the vehicle, making it more robust). The penalty in efficiency is only 0.58% which is not significant.

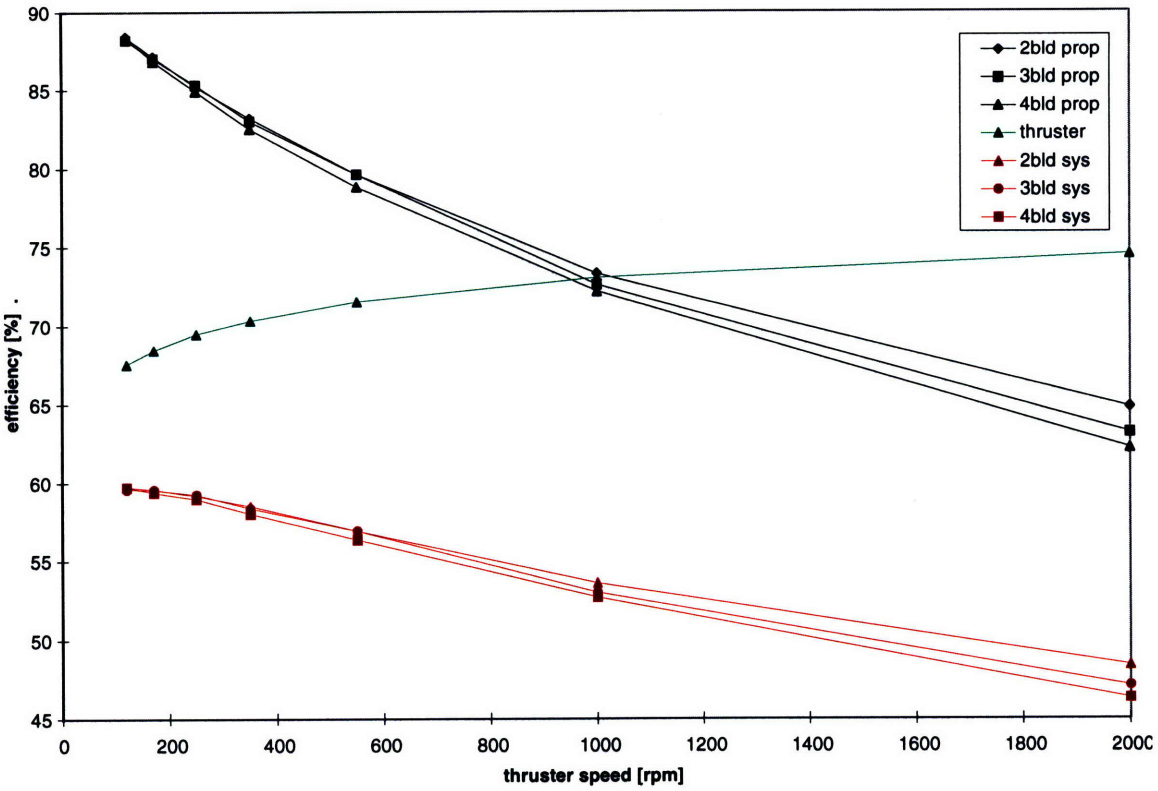

Figure 6-2: Thruster, Single-Propeller and System Efficiencies. The efficiencies of the thruster, the single propellers and the system efficiencies are shown as a function of the thruster shaft-speed. With increasing thruster shaft-speed, the gearbox reduction-ratio decreases, resulting in reduced gearbox losses and an increased thruster performance. In contrast, the propeller efficiency decreases for high rates of rotation, resulting in a decreasing system efficiency for increasing rates of rotation.

Figure 6-2 illustrates that a system without gearbox would perform significantly worse than a system with gearbox. As the gearbox reduction-ratio approaches 1.6 the system performance has reached 48.41% which is already significantly less than the optimum system efficiency of 59.83%. For higher thruster shaft rpm (lower gearbox reduction-ratio) the trend observable in Figure 6-2 is towards decreased system performance and therefore a further decreased system efficiency can be expected for a solution without a gearbox.

If a thruster without oil-filling,seal and gearbox were employed, feasible by using a magnetic coupling between motor and propeller, the solution employing a gearbox, seal and oil-filling would still be superior. This can be seen by assuming that the thruster operates at its peak

	Contra-Rotating Propeller
efficiency	*90.2*
rpm	60 each
diameter [ft]	2.2 and 2.15
torque [Ncm]	390 each
requ. power [W]	49.21

Table 6.11: Optimum Contra-Rotating Propeller

efficiency, which is in the case of no oil filling, gearbox and seal 89%, the propeller efficiency has to be 66.3% to achieve a system efficiency of 59%. It is apparent from Figure 6-2 that this is not realistic for the required rate of rotation of about 3000 rpm to operate in the vicinity of the thruster efficiency peak.

In conclusion, a good solution for a propulsion system employing a single propeller consists of a thruster with an approximately 13.2:1 gearbox, and a three bladed propeller with a diameter of about 1.3 feet. The achievable steady state system performance in this case is about 59%.

6.2.2 Contra-Rotating Propellers

The optimum contra-rotating propeller for Odyssey II's operating conditions was found by varying the propeller rate of rotation, the propeller diameters and the number of blades between two and four systematically. It was assumed that both propellers require the same torque, have the same number of blades and operate with the same rate of rotation in opposite directions. Usually the propeller downstream is slightly smaller than the propeller placed upstream as shed tip-vortices from the upstream propeller can induce vibrations in the propeller placed downstream. The distance between both components was chosen to be 0.2 feet. Varying the distance had a slight or no influence on the efficiency, as ideal flow is assumed for lifting line theory and swirl induced to the fluid does not disperse. The characteristics of the resulting optimum contra-rotating propeller are summarized in Table 6.11.

The estimation of the system performance requires an estimate of the drivetrain efficiency for the contra-rotating propellers. This efficiency was assumed to be 90%. The low rate of rotation of the propellers required a gearbox reduction-ratio of 55:1, degrading the thruster performance to 65.8%. The system performance could then be estimated to be 53.4%. This performance is significantly worse than for the single propeller due to the penalty of the drivetrain efficiency

and the high gearbox reduction-ratio.

To assess if a propulsion system using contra-rotating propellers can out-perform a system employing a single propeller, the performance of the contra-rotating propulsor at an increased rate of rotation was investigated. The optimum propulsive efficiencies at rates of rotation of 550 rpm and 1000 rpm were calculated and were found to be 79.2% and 71.7%, respectively. Design variables were again propeller diameters and number of blades.

The maximum propulsive efficiencies of a single propeller at the same rates of rotation are 79.6% and 73.3% respectively. The advantage of swirl cancellation for the light-loaded contra-rotating propeller is cancelled by the viscous losses due to the second propeller. The overall propulsive performance is similar to the performance of a single propeller. Together with the complexity inherent to the drivetrain, the maximum propulsive efficiency of the contra-rotating propellers at a high rates of rotation make this solution unattractive.

6.2.3 Vane-Wheel

The optimum propeller/vane-wheel combination for Odyssey II's operating conditions was found by varying the propeller and the vane-wheel's rate of rotation independently, the propeller and vane-wheel diameters assuming that the diameter of the vane-wheel is 20% larger than the propeller diameter, and the number of blades between two and four for the propeller and two and eight for the vane-wheel. The size of the design space, defined by the number of independent propulsor variables, makes a comprehensive investigation infeasible. Therefore, a systematic iterative search was performed. Changing one propulsor parameter and calculating the resulting propulsive efficiency indicated if it is superior to the previous configuration. Inferior versions were eliminated and superior followed up. Different starting points with randomly chosen parameters were used to ensure that the global maximum was found. The search led to a propeller/vane-wheel combination, which characteristics are summarized in Table 6.12

The optimum system performance was estimated to be 59.13% with a gearbox reduction-ratio of 27.6:1 and a thruster efficiency of 67.58%. This system efficiency is close to the efficiency of the propulsion system employing a single propeller.

Below the performance of the propeller/vane-wheel combination for increased rates of rotation is investigated. To justify its use it has to have a significant advantage in propulsive

	Propeller/Vane-Wheel Combination
efficiency	*87.5*
rpm	120 propeller, 20 vane-wheel
diameter [ft]	1.8 propeller, 2.16 vane-wheel
number of blades	3 propeller, 2 vane wheel
torque [Ncm]	401
requ. power [W]	50.7

Table 6.12: Optimum Vane Wheel

	Propeller/Vane-Wheel Combination
efficiency	*73.6*
rpm	1000 propeller, 300 vane-wheel
diameter [ft]	0.6 propeller, 0.72 vane-wheel
number of blades	3 propeller, 3 vane wheel
torque [Ncm]	56
requ. power [W]	60.4

Table 6.13: Optimum Vane Wheel at 1000 rpm

efficiency at high rates of rotation compared to the single propeller. Therefore, the optimum propeller/vane-wheel combination at 1000 rpm was examined by performing a similar search as described above. The result is summarized in Table 6.13.

The propeller/vane-wheel combination offers a similar propulsive efficiency as a single propeller (propulsive efficiency of a two bladed propeller at 1000 rpm is 73.3%). A brief assessment of the propeller/vane-wheel combination at a rate of rotation of 2000 rpm revealed no significant advantage in propulsive efficiency compared to the single propeller.

In summary the propeller/vane-wheel combination offers a comparable propulsive efficiency as the single propeller but is not worth the effort.

6.2.4 Pre/Post-Swirl Stators

A paper published in 1994 by M. Guener and E.J. Glover [16] investigates the effect of stator blades on the propulsive efficiencies of AUV's. In particular, the effect of variation of the axial distance between the propeller and stator and the number of stator blades on the propulsor characteristics were investigated using a computational tool based on lifting line theory such as MIT-PLL. The findings of the research were that an optimum number of stator blades is seven while the propulsive efficiency increases with increasing distance between stator and propeller.

	Stator/Propeller Combination
efficiency	*88%*
rpm	85
number of blades	3 propeller, 4 stator
diameter [ft]	2.1 each
torque [Ncm]	565
requ. power [W]	49.96

Table 6.14: Optimum Propeller/Stator Combination

The vehicle discussed in the paper has a length of 5.3 m, more than double the length of Odyssey II, and therefore the results are not directly applicable for the Odyssey II vehicle.

As with the other energy saving propulsors investigated before, the use of a stator is only worthwhile if the energy losses in the slip stream (swirl losses) are significant i.e. the propeller loading is moderate to high. The previous assessment showed that the use of energy saving devices caused decreased propulsive efficiency due to their inherent viscous losses and the required low rate of rotation of the propulsor causing high gearbox losses. Nevertheless, stator blades provide an effective means of removing the unbalanced torque and therefore it is worthwhile to investigate their performance.

The first step was again to design, the optimum propeller/stator combination for Odyssey II's operating conditions. The variables are the number of blades of the propeller, the number of blades of the stator, the rate of rotation of the propeller, the diameter of the stator and the diameter of the rotor. Varying the distance between the components had little or no influence on the predicted efficiency values as ideal flow is assumed for lifting line theory and swirl imparted to the fluid does not disperse. Furthermore, it made no difference if the stator was placed upstream or downstream of the propeller.

The characteristics of the resulting optimum stator/propeller combination for Odyssey II's operating conditions are summarized in Table 6.14. The result is close to the optimum three-bladed single-propeller, which offered a propulsive efficiency of 89.7%. To assess the potential of stators at higher rates of rotation, the optimum propeller/stator combination for higher rates of rotation were designed. The results are summarized in the Table 6.15 and compared to the propulsive efficiencies of the three-bladed single-propeller. The peak performance of the propulsion system employing stator blades (58.6%) is close to but less than the three-bladed

rpm	Propulsive Efficiency	Diameter	Number of Blades	3 Bladed Single Prop. Eff.
250	*85.1*	1.3	3 prop, 3 stator	85.3
550	*79.3*	0.9	3 prop, 3 stator	79.6
1000	*73*	0.6	3 prop, 5 stator	72.6

Table 6.15: Optimum Propeller/Stator Comination at Higher Rates of Rotation

single-propeller system (59.83).

An interesting design option is to use stator blades additionally as vehicle control fins. As the vehicle requires control surfaces anyway, it makes sense to either use four large control surfaces as stator blades and simultaneously as vehicle control fins, or to use a total of eight stator blades, of which four have an increased area and serve as control fins, while the remaining four blades are smaller and fixed. The control surfaces operate constantly at a slight angle of attack, giving the inflow in the propeller a slight pre-swirl and balancing the propeller torque. Comparison of the efficiency of this configuration is not straight-forward as the drag of the existing control fins is included in the vehicle drag. Using four or eight stator blades instead of three and five, respectively, as assessed in Table 6.15, decreases propulsive efficiency by only up to 0.2%. If the stators double as control fins, then the 0.2% is likely more than compensated by the drop in effective vehicle drag caused by elimination of the existing control surfaces. Furthermore, the propeller torque would be balanced.

It has to be kept in mind that stator blades with a fixed angle of attack are designed for a certain vehicle speed. Thus, if vehicle speed changes, stator blades do not provide the same increase in efficiency unless their angle of attack is adjustable. If the angle of attack is variable, as in the case when they additionally function as control fins for the vehicle, a possible control loop for optimum stator-angle of attack could be a coupling with the roll-sensor of the vehicle. The induced swirl from the propeller, causing the unbalanced torque, tends to roll the vehicle. The optimum angle of attack for the stator blades is reached when the swirl and therefore the torque is balanced, which could be noticed by measuring the deviation from the neutral roll angle of the vehicle. The coupling of control of the vehicle with propulsion in the manner described above might lead to unforeseen problems and requires further investigation.

The stator can be placed either upstream or downstream of the propeller. If the stator is placed upstream from the propeller, the inflow speed is approximately the vehicle velocity,

whereas if the stator is placed downstream from the propeller, the inflow speed is higher than the vehicle speed. To achieve the same amount of swirl, the stator-blades placed upstream need to operate at a higher angle of attack (low viscous losses, high drag losses) than the stator blades downstream (high viscous losses, low drag losses). For Odyssey II's operating conditions it made no difference if the stator blades were placed upstream of downstream from the propeller. The position downstream is more challenging from a practical perspective than upstream, as in the upstream position the stator can be mounted to the hull which is not possible downstream. If the control-fin function is incorporated in the stator, a placement downstream from the propulsor would be even more difficult.

6.2.5 Ducted Propeller

The optimum ducted propeller for Odyssey II's operating conditions was found by varying the propeller rate of rotation, the propeller diameter and the number of blades of the propeller. The inherent drag of the duct is included in the MIT-PLL calculation of the propulsive efficiency. Therefore, the geometry of the duct has to be specified by defining its chord length and maximum thickness, which are normalized with the propeller diameter, as well as the drag coefficient. The normalized chord length was chosen to be 0.25, the normalized maximum thickness 0.01, and the drag coefficient 0.0085, which is a typical value for a duct. Chord length and thickness are minimal values to keep duct drag-forces small. The duct was conservatively assumed to produce no thrust as the design of a thrust producing duct is difficult. The gap between propeller tip and duct was assumed to be smaller than physically feasible as ongoing research [25] has shown that the water flux through this gap is smaller than predicted by potential flow.

The optimum ducted-propeller for Odyssey II's operating conditions was found to have a relative small diameter of 1.3 feet and a propulsive efficiency of 85% at 180 rpm using three blades. The results are summarized in Table 6.16. The resulting system efficiency is inferior to the efficiency of a propulsion system using a three-bladed single-propeller. Therefore, to out-perform the single-screw propeller, the ducted propeller would have to be significantly more efficient at high rates of rotation to take advantage of the inherent increase in gearbox efficiency. The maximum propulsive efficiency of a ducted propeller at 1000 rpm is 75.1%, resulting in a system efficiency of 54.75%. Compared to the propulsion system employing a single propeller

	Ducted Propeller
propulsor efficiency	*85*
diameter [ft]	1.3
thruster eff.	68.6
gearbox ratio	18.51
gearbox eff	89.37
system eff	58.31

Table 6.16: Optimum Ducted Propeller

at the same rate of rotation, the system efficiency of the propulsion system employing a ducted propeller is slightly higher, but still inferior to the maximum system performance of 59.57 achievable with a single propeller at a lower rate of rotation. The maximum system performance for a ducted propeller and a thruster using no gearbox, oil filling and seal was assessed briefly and was found to be approximately 48%, which is again an inferior solution.

The propulsion system employing a ducted propeller achieves an efficiency comparable to the solution employing a three-bladed single-propeller with the same diameter. The drag of the duct and its positive tip-flow-influencing effect nearly cancel each other. In applications where a well protected propeller is desirable, a duct is therefore an attractive alternative to an un-ducted propeller. Nevertheless, the design of the duct has to be carried out very carefully to prevent unnecessary losses.

A brief assessment of the combination of stator blades and duct showed no potential for a significant increase in propulsive efficiency and was therefore not pursued.

6.2.6 Conclusion

The clear result of the propulsor and propulsion system assessment in this chapter is the superiority of the single-screw propeller over all other propeller based design options for Odyssey II's operating conditions. Energy-saving propulsors offer similar system efficiencies but are neither better nor worth the effort. Odyssey II's operating conditions favor lightly-loaded propellers and therefore swirl-recovering devices degrade efficiency due to inherent viscous losses and the required low rate of rotation of the propeller(s), causing high gearbox losses.

A good choice for Odyssey II's propulsor is a three bladed propeller with a diameter of 1.3 feet. The matching thruster employs a 13.2:1 gearbox, which allows the propulsion system

to operate at a predicted efficiency of 59.25%. The advantage of this choice is the moderate gearbox reduction-ratio and the intermediate propeller diameter of 1.3 feet, which simplifies the handling of the vehicle and makes it more robust. Although the efficiency of a three bladed propeller is only slightly better than a two bladed propeller, it provides a higher redundancy. If one propeller blade is lost during a mission, the remaining parts of the propulsor are still capable of generating sufficient thrust. Additionally, the resulting eccentric force is less than for a two bladed propeller loosing a blade and therefore a damage of the seal or gearbox is less likely. In general, the number of blades was found to have only a slight influence on propulsive efficiency.

Chapter 7

Summary and Conclusions

In this chapter, the major findings of the research presented in this thesis are summarized and conclusions are drawn concerning the Odyssey II propulsion system. The chapter concludes with suggestions for future work and attempts to identify promising approaches.

In Chapter 2, possible propulsion system components were identified and discussed. Propeller-based propulsors and brushless, permanent-magnet DC motors as actuator options were found to be the components most likely to meet the design specifications requiring high efficiency, low cost and high reliability.

In Chapter 3 a computational model of the thruster was developed, which included the characteristics of a brushless, permanent-magnet DC motor, the viscous effects of a fill-fluid in the gap between the rotor and the stator of the motor, the planetary gearbox, the shaft-seal, and thermal effects. The computational model is modular and enables the designer to assess different thruster configurations and to match thruster and propulsor to maximize system performance.

Chapter 4 presents the results of tests on the Odyssey II thruster. The experimental error was small and the results accurate. The measured losses inherent to the seal, fill-fluid and the gearbox were discussed qualitatively and quantitatively. Losses inherent to the motor controller have been included in the performance of the electric motor as they are not easily measured. The most significant losses are typically electric I^2R losses, followed by gearbox, seal and viscous losses. Viscous losses due to the fill-fluid are significant at high motor-speed, but in general less significant than electric I^2R, gearbox and seal losses. At lower motor-speed, the increased lubrication of the fill-fluid improves thruster performance. Operating the thruster in

a low-temperature environment improved performance at high load-torque by improving heat dissipation and reducing the winding resistance and therefore I^2R losses. Independent from the component losses, the position of the Hall-effect senors can change the overall efficiency of the thruster by as much as 40%.

Motor efficiency increases as the applied voltage increases. In addition, the efficiency-versus-load-torque curve becomes flatter for high load-torque. This implies that the motor controller should be operated at maximum setting at design speed to maximize efficiency, instead of running at an intermediate setting. Another observation, which was not quantified, was that the high viscosity fill-fluids noticeably reduced gearbox noise.

In Chapter 5, experimental data from dynamometer tests was used to verify the computational thruster model. The model showed good agreement with the experimental data. It should prove a valuable tool for the design of thruster units constructed with components similar to those employed in Odyssey II.

In Chapter 6, the computational model of the thruster was used to assess the design options for the propulsion system. This assessment showed the clear superiority of a propulsion system consisting of a three-bladed single-screw propeller, mated to a thruster employing a permanent-magnet brushless DC motor. Including the effects of the gearbox and oil-filling, a system efficiency of approximately 59% was predicted. Propulsion systems employing energy-saving propulsors (which place additional control surfaces in the flow to recover energy contained in the propeller wake) are seen to have inferior performance. This is due to inherent viscous losses or low rates of rotation, resulting in a high gearbox reduction-ratio. Odyssey II's operating conditions favor lightly-loaded propellers, which produce insufficient swirl-losses to justify the use of swirl-recovering devices. The maximum propulsive efficiencies for the propulsors examined, as well as the properties for the required gearboxes and the system efficiencies are summarized in Table 7.1. It was shown in Chapter 6 that, while the gearbox causes significant losses, eliminating the gearbox results in an unacceptable system performance due to the significantly degraded propulsive efficiency.

The poor performance of Odyssey II's existing propulsion system is due to the poor match between motor and propeller. This mismatch causes the electric motor to operate at high load torque, increasing significantly electrical losses. Defining Odyssey II's operating point by the

Propulsion System	Max. Propulsive Efficiency	Requ. Gerabox Reduction Ratio	Gearbox Efficiency	System Efficiency	Complexity Rating (1-5)
single screw propeller	89.7	39	86.84	**59.83**	1
contra-rotating prop.	90.2	55	85.7	53.4	5
propeller/vane-wheel	87.5	28	87.96	59.13	3
pre/post-swirl stators	88	39.3	86.81	58.6	2
ducted propeller	85	18.51	89.37	58.31	3

Table 7.1: Summary of System Efficiencies

design torque of the original propeller design, Figure 7-1 illustrates the flaw of the current design. It can be seen that the thruster efficiency at the estimated operating point is approximately 22%, which when combined with an assumed propulsive efficiency of the propeller of 80%, results in a system efficiency of 17%.

The developed computational model, when used with the design path outlined in Figure 2-1 enables the designer to match thruster and propeller accurately to assure a good match between the thruster operating-point and the propulsor. A quick fix for Odyssey's propulsion system is to employ a different gearbox, shifting the operating point of the motor to high efficiency while keeping the power output constant. A complete redesign of the propulsion system results in a predicted system efficiency of 59%. This system employs a three-bladed propeller with a diameter of approximately 1.3 feet, a 13.2:1 gearbox, and a Pittman Elcom Series 5113 brushless DC motor with a 2.33 ohms winding.

The last section of this chapter discusses suggestions for future work and attempts to identify promising approaches. Looking at propeller-based propulsion systems, there is one major source of inefficiency whose elimination would significantly increase the efficiency of the propulsion system. The assessments in Chapter 6 showed that the propulsion-system performance is maximized by operating the propulsor, as well as the thruster at their efficiency peaks by means of a gearbox. It also became apparent that for Odyssey II's operating conditions only propeller-based propulsors with a low rate of rotation offer high efficiencies. Assuming that there is no propulsor available offering high efficiency at high rates of rotation, a task for the future is to find or to make an actuator, which is highly energy efficient at low rates of rotation. This would allow the elimination of the gearbox, and assuming an oil-filled actuator, lower viscous losses. Based on the computational model, assuming a similar peak performance of the

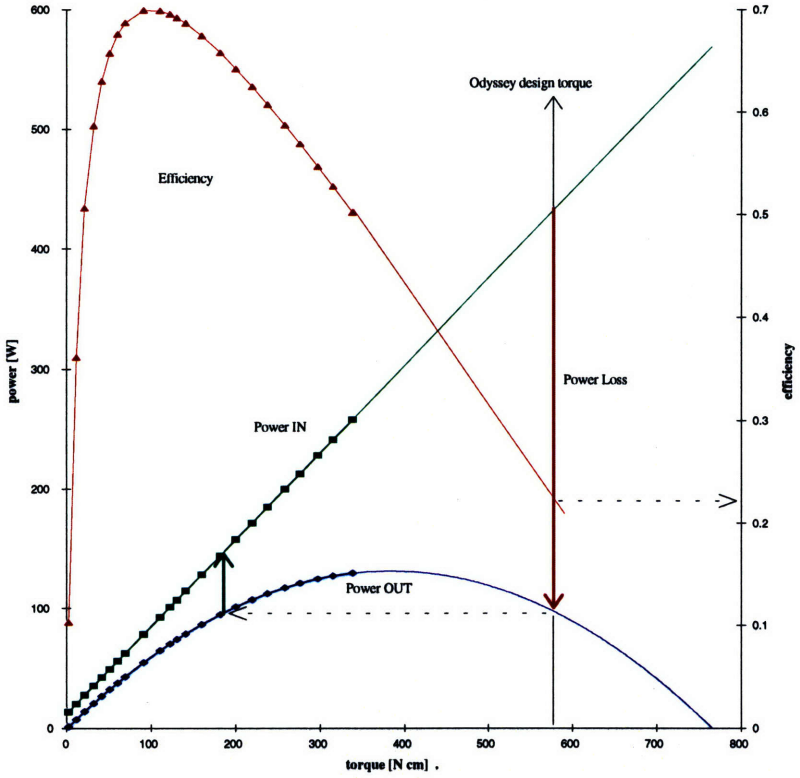

Figure 7-1: Odyssey II's Estimated Operating Point. The curves shown in this plot are power-out, power-in and efficiency. They are the results from the dynamometer tests described in Chapter 4 for the whole thruster at 52 volts. The curves are extrapolated to high load torque (the tested load-torque range is indicated by marks on the curves). Odyssey II's propeller design torque is indicated at a load torque of approxmately 580 Ncm. The difference between the power-out and power-in curve at this load torque, indicated by a red arrow, is the wasted power, which is mainly spent on electrical losses. Shifting the operating point to the same power-out at lower load-torque significantly reduces the wasted power, indicated by a green arrow, and lets the thruster operate close to its efficiency peak. It can be seen that the thruster efficiency at Odyssey II's current operating point is approxmately 22%

hypothetical future actuator as the modeled motor, an increase in system efficiency in the order of magnitude of 10 to 15% can be expected. One possible actuator is the switched-reluctance motor, which offers a high efficiency over a broad speed range and therefore deserves further investigation as it becomes commercially available in the power-range required by Odyssey II.

Minor but important improvements in propulsion system efficiency could be achieved by improving the efficiency of the gearbox, reducing the viscosity of the fill-fluid, improving the efficiency of the motor controller and reducing the friction of the shaft-seal. As long as the power required by the propulsor has to be transmitted by high torque and low rotational-speed, a rigid shaft is required. Unless a low-friction, high-pressure shaft-seal or a suitable magnetic coupling is developed, the thruster housing will be oil-flooded, resulting in viscous losses.

Finally, unconventional developments as the fish-fin propulsion and emerging commercial products as ring-thrusters should be followed up as they promise interesting alternatives to propeller-based propulsion systems that are custom-assembled from off-the-shelf products.

Bibliography

[1] S.M. Abu Sharkh. M.R. Harris, R.L. Stoll. 1995. *Design and Performance of an Integrated Thruster Motor.* Electrical Machines and Drives Conference Publication.

[2] D. Barrett, M. Gosenbaugh, M. Triantafyllou. 1996. *The Optimal Control of a Flexible Hull Robotic Undersea Vehicle Propelled by an Oscillating Foil.* 1996 IEEE Symposium on Autonomous Underwater Vehicle Technology.

[3] C. Barus. 1893. American Journal of Science. 45, 87.

[4] J.G. Bellingham, J.W. Bales, D.K. Atwood, C. Chryssostomides, T.R. Consi, C.A. Goudey. 1992. *Demonstration of a High-Performance, Low-Cost Autonomous Underwater Vehicle.* MIT Sea Grant College Program.

[5] Private communication with Dr. James Bellingham, MIT Sea Grant.

[6] P.R. Bevington. 1969. *Data Reduction and Error Analysis for the Physical Sciences.* McGraw-Hill Book Company.

[7] A.M. Bradley. 1992. *Low Power Navigation and Control for Long Range Autonomous Underwater Vehicles.* Proceedings of the Second International Offshore and Polar Engineering Conference San Francisco.

[8] A.M. Bradley. 1990. *Motor and Gearbox Studies.* Internal Memo, Woods Hole Oceanographic Institution.

[9] R. Burcher, L.Rydill. 1994. *Concepts in Submarine Design.* Ocean Technology Series 2, Cambridge University Press.

[10] J. Collins. 1992. *A Review of Technologies and Applications for Autonomous Underwater Vehicles.* A Draft Discussion Paper for the Working Group on Marine Robotics of the Engineering Committee on Ocean Resources, University of Victoria, Canada.

[11] W.B. Coney. 1988. *MIT-PLL Propulsor Lifting Line Code, User's Manual.* MIT, Department of Ocean Engineering.

[12] Dubbel. 1994. *Handbook of Mechanical Engineering.* Springer Verlag.

[13] S.N. Gangadharan, H.L. Krein. 1989. *Jet-Propelled Remote-Operated Underwater Vehicles Guided by Tilting Nozzles.* Marine Technology, Vol. 26, No. 2.

[14] K.+R. Gieck. 1995. *Technische Formelsammlung.* Gieck Verlag.

[15] Globe Motors. 1990. *Product Catalog M-100.*

[16] M.Güner, E.J. Glover. 1994. *Propeller/Stator Propulsors for Autonomous Underwater Vehicles.* 1994 IEEE Symposium on Autonomous Underwater Vehicle Technology.

[17] J.K. Holt, D.G. White. 1994. *High Efficiency, Counter-Rotating Ring Thruster for Underwater Vehicles.* 1994 IEEE Symposium on Autonomous Underwater Vehicle Technology.

[18] T. Kenjo. 1991. *Electric Motors and their Controls.* Oxford Science Publications.

[19] J.E. Kerwin. 1996. *Hydrofoils and Propellers.* 13.04 Lecture Notes, MIT.

[20] N.M. Kopp, G.W. Brown. 1994. *Electric Motor/Controller, Design Tradeoffs for Noise, Weight, and Efficiency.* Proceedings of the 1994 Symposium on Autonomous Underwater Vehicle Technology IEEE.

[21] W.P. Krol, C.P. Cho. 1996. *High Energy Density Permanent Magnetic Motors for Underwater Systems.* 1996 IEEE Symposium on Autonomous Underwater Vehicle Technology.

[22] Private communiction with Prof. Jeffrey Lang, Professor for Electrical Engineering & Computer Science, MIT.

[23] P.J. Lawrenson, Leeds University, UK. 1996. *Switched Reluctance Motors: The Drive of the Future?.* Handout from a Seminar dated 3/15/1996 in Arlington, VA.

[24] MATLAB. 1984-1994. The MathWorks, Inc.

[25] Private communication with Gerard McHugh, MIT Propeller Tunnel.

[26] J.C.S. Meng, J.D. Hrubes, P.J. Hendricks, D.P. Thivierge, C.W. Henoch. 1991. *Experimental Studies of a Superconducting Electromagnetic Thruster for Seawater Propulsion and Future Technological Challenges.* Proceedings Oceans 91 Volume 3 by the Oceanic Engineering Society of IEEE.

[27] J.N. Newman. 1977. *Marine Hydrodynamics.* The MIT Press.

[28] Norton Petroleum. *Spec. Sheet Enduro Oil.* Newark, Delaware.

[29] PITTMAN. 1989. *Bulletin 500, Motor Data Sheet for the PITTMAN Model 5113 DC Brushless Motor.* PITTMAN Harleysville, PA.

[30] P.K. Poole, P. Clower. 1996. *A Systems Approach to AUV Propulsion Design.* Marine Technology Society Journal, Volume 30.

[31] F.E. Saner. 1987. *PITTMAN Servo Application Notes.* PITTMAN.

[32] H. Schneekluth. 1987. *Ship Design for Efficiency and Economy.* Butterworths.

[33] V. Stepina, V. Vesley. 1992. *Lubricants and Special Fluids.* Elsevier.

[34] P. Stevenson, C.A. Hunter. 1994. *Development of an Efficient Propulsion Motor and Driver for Use in the Deep Ocean.* Institute of Oceanographic Sciences Deacon Lab, UK.

[35] C. Walther. 1933. *Oel und Kohle.* 1, 71.

[36] T.J. Woodford. 1991. *Propulsion Optimization for ABE, an AUV.* Master of Science Thesis at the Massachusetts Institute of Technology and the Woods Hole Oceanoghraphic Institution.

[37] D.R. Yoerger, J.C. Cooke, JJ.E. Slotine. 1990. *The Influence of Thruster Dynamics on Underwater Vehicle Behavior and Their Incorporation Into Control System Design.* IEEE Journal of Oceanic Engineering, Vol. 15.

Chapter 8

Appendix

The following program listing is the MATLAB script file for the computational model of the thruster:

```
% THRUSTER\ SIMULATION
% MATLAB CODE
% Stefan Deucker 10-10-96
% last time edited 12-4-96

clear all;
clear figure;
close all;
! del diary
diary on


%************************************************************
% ////////////////////////// INPUT //////////////////////////
%************************************************************
% MOTOR AND OPERATING CHARACTERISTICS
```

```
%************************************************************
% E: applied voltage [V]
E = 48;
%RT: overall resistance [ohms]
 RT = 3.8;
% R: stator resistance [ohms]
 R = 2.33;
%KT: torque constant [N*m/A]
KT = 120*10^(-3);
%KE: back emf constant [V/(rad/s)]
KE = 120*10^(-3);
%TF: friction torque [Nm]
TF = 4.0*10^(-3);
%TL: external torque load range [N cm] {N m / 100= N cm}
TL = 1:2:100;
% T: ambient temperature [degree C]
T = 3;
% TPR: thermal impedance [deg/W]
TPR = 1;
% Tmax: maximum winding temperature [degree C]
Tmax = 155;
% D1: rotor diameter [mm]
D1 = 30.4292;
% D2: stator diameter [mm]
D2 = 31.1658;
% L: lenght of rotor/stator [mm]
L = 62;
% G: gearbox speed reduction ratio
G = 5.54;
% S: do you want to simulate a shaft seal?; yes=1; no=0
```

```
S = 1;
%*************************************************************
% OIL CHARACTERISTICS
%*************************************************************
% is the motor oil filled? yes: oil = 1; no: oil = 0
% use if structure to calc. both case losses
oil = 1;
% T1: first teperature of known viscosity
T1 = 40;
% visc1: viscosity at T1 [N s / m^2]
visc1 = 0.001569;
% T2: second temperature of known viscosity
T2 = 20;
% visc1: viscosity at T2 [N s / m^2]
visc2 = 0.002484;
% viscosity air, if no oil filling is used [N s / m^2]
viscair = 0.00001798;

%*****************************************************************
% /////////////////////////// CALCULATE ////////////////////////
%*****************************************************************

%*************************************************************
% calc. torque loss due to gearbox + seal for each load torque  *-------------
%*************************************************************

TLs = TL*G; %gearbox shaft torque
effgear=G^(-0.0385); %estimated gearbox eff
TMgear=( (TLs/(effgear*G))-(TLs/G) )/100; %torque loss due to gearbox
```

```
if S == 1
  TMgear = TMgear + 0.012; %torque loss due to shaft seal
end

%*************************************************************
% calculate characteristic motor curves                      *-------------
%*************************************************************

Tactual=T* TL./TL;
figure

% if no heating up of the thruster unit is to be simulated, set the loop
% to 1 and the first plot will show the thruster unit performance at
% room temperature

for a=1:6 %_____________________________________________________________X

for n=1:size(TL,2) %-------------------------------------------------X

  % -----calculate fill fluid viscosity, oil or air
  viscosity(n) = visc(viscair, oil, visc2, visc1, T2, T1, Tactual(n));
  if viscosity(n) < viscair
    viscosity(n)=viscair;
  end

  % -----viscous damping constant, needed for speed calculation
  DF(n) = (-pi * (D1*0.001)^3 * (L*0.001) * viscosity(n)) / ...
          ( (D1*0.001)-(D2*0.001));

  % -----calculate speed
```

```
  omega(n) = -( -E*KT + RT*(TL(n)/100) + RT*(TF+TMgear(n)) ) / ...
             (DF(n)*RT + KT*KE);
  rpm(n) = omega(n)*30/pi;

  % -----calculate torque loss, current, power out, power in and eff.
  TM(n) = DF(n) .* omega(n) + (TF+TMgear(n)); %frictional and viscous losses
  I(n) = (1/KT)* (TL(n) / 100) + TM(n)/KT;  %current
  Pout(n) = 1/30 * pi * rpm(n) * TL(n)/100;  %power out
  Pin(n) = E * I(n);  %power in
  eff(n)= Pout(n) / Pin(n); %efficiency

end %-------------------------------------------------------------------X

%*****************************************************************
% calculate overall ultimate temp. rise due to power losses     *-----------
%*****************************************************************

IR = I.*I.*R;  %electric power losses
loss = TM.*omega;  %viscous and frictional power losses
deltaTIR = IR*TPR;  %temperature rise due to electrical losses
deltaTloss = loss.*TPR;  %temperature rise due to visc.&fric. losses
deltaT = deltaTIR+deltaTloss;  %ultimate temp rise
Tactual = T+deltaT; %actual winding temperature

%************************************
%convergence check plot              *-----------------------------------
%************************************

hold on
subplot(1,2,1), plot(TL,viscosity,'-.y')
```

```
xlabel('load torque [N cm]')
ylabel('viscosity [Ns/m2] ')
title(' Convergence Check ')
hold on
subplot(1,2,2), plot(TL,Tactual,'-.y')
xlabel('load torque [N cm]')
ylabel('Tactual [C]')

end %_____________________________________________________________________X

% determine for which load torque the max winding temp. is exceeded
for i=1:size(TL,2);
  if Tactual(i) < Tmax
   count = i;
  end;
end;

%*****************************************************************
% calculate altered motor constants and resulting performance   *-------------
%*****************************************************************

C = -0.00025; %constant for rare earth magnets, ELCOM series
clear n
for n=1:size(TL,2) %_____________________________________________________X

  % viscosity
  viscosity(n) = visc(viscair, oil, visc2, visc1, T2, T1, Tactual(n));
  if viscosity(n) < viscair
    viscosity(n)=viscair;
  end
```

```
  % viscous damping constant
  DF(n) = (-pi * (D1*0.001)^3 * (L*0.001) * viscosity(n)) /...
          ( (D1*0.001)-(D2*0.001));
  % motor constants at each operating point
  RTsteady(n) = (RT-R)+(R * (234.5 + (23+deltaT(n))) / (234.5+23));
  KTsteady(n) = KT* (1+C*(deltaT(n)));
  KEsteady(n) = KE* (1+C*(deltaT(n)));

  % calculate speed
  omegasteady(n) = -(-E*KTsteady(n) + RTsteady(n)*(TL(n)/100) + ...
  RTsteady(n)*(TF+TMgear(n))) / (DF(n)*RTsteady(n) + KTsteady(n)*KEsteady(n));
  rpmsteady(n) = omegasteady(n)*30/pi;

  % calculate torque loss, current, power out, power in and eff.
  TMsteady(n) = DF(n) * omegasteady(n) + (TF+TMgear(n));
  Isteady(n) = (1/KTsteady(n))* (TL(n) / 100) + TMsteady(n)/KTsteady(n);
  Poutsteady(n) = 1/30 * pi .* rpmsteady(n) * TL(n)/100;
  Pinsteady(n) = E * Isteady(n);
  effsteady(n)= Poutsteady(n) / Pinsteady(n);

end %_____________________________________________________________________X


%************************************************************
% ////////////////////////// WRITE //////////////////////////
%************************************************************

para1 = ['Voltage:' num2str(E) '  Amb.temp.:' num2str(T) '  Therm.impedance:' num2str(TP
para2 = ['Oil:' num2str(oil) '       Gearbox:' num2str(G) '   Seal:' num2str(S) ' '];
```

```
para3 = ['The max. efficiency without temp. effects is:' num2str(max(eff)) ' '];
para4 = ['The max. efficiency with    temp. effects is:' num2str(max(effsteady)) ' '];
u = ['The maximum operating load torque (due to the max. winding temp) is ' ...
    num2str(TL(count)) ' Ncm'];
v = ['    TL  -  Poutst  -  effst - currentst  -  rpmst  -  T  -  Pout  -  eff'];
w = [ TL' Pousteady' effsteady' currentsteady' rpmsteady' Tactual' Pout' eff' ];
disp(para1)
disp(para2)
disp(para3)
disp(para4)
disp(u)
disp(v)
disp(w)

diary off
%*************************************************************
% /////////////////////////// PLOT ////////////////////////////
%*************************************************************

% plot final values in convergence plot
hold on
subplot(1,2,1), plot(TL,viscosity,'-r')
xlabel('load torque [N cm]')
ylabel('viscosity [Ns/m2] ')
title(' Convergence Check ')
axis([ 0 TL(count) 0 0.006 ])
hold on
subplot(1,2,2), plot(TL,Tactual,'-r')
xlabel('load torque [N cm]')
ylabel('Tactual [C]')
```

```
axis([ 0 TL(count) 0 Tactual(count) ])

 plot power losses and temperature rise ____________________________
figure
subplot(2,2,1), plot(TL,loss,'-y')
%xlabel('load torque [N cm]')
%ylabel(' power loss [W] ')
title('Visc.+Fric. P-Loss [W] vs. Load Torque [Ncm]')
axis([ TL(1) TL(count) 0 max(loss) ])

subplot(2,2,2), plot(TL,IR,'-y')
%xlabel('load torque [N cm]')
%ylabel(' power loss [W] ')
title('I2R Losses [W] vs. Load Torque [Ncm]')
axis([ TL(1) TL(count) 0 IR(count) ])

subplot(2,2,3), plot(TL,deltaTIR,'-y')
hold on
plot(TL,deltaTloss,'-.r')
%xlabel('load torque [N cm]')
%ylabel(' temp rise [C] ')
title('Temp.Rise due to P-Losses vs. LT [Ncm]')
axis([ TL(1) TL(count) 0 deltaTIR(count) ])

subplot(2,2,4), plot(TL,Tactual,'-y')
%xlabel('load torque [N cm]')
%ylabel(' temp [C] ')
title('Ultim. Temp. [C] vs. Load Torque [Ncm]')
axis([ TL(1) TL(count) 0 Tactual(count) ])
```

```
% plot comparison between curves, altered results _____________
figure
subplot(2,2,1), plot(TL,I,'-y')
%xlabel('load torque [N cm]')
%ylabel(' current [A] ')
hold on
plot(TL,Isteady,'-.r')
axis([ TL(1) TL(count) 0 Isteady(count) ])
title('Current [A] vs. Load Torque [Ncm] ')

subplot(2,2,2), plot(TL,rpm,'-y')
%xlabel('load torque [N cm]')
%ylabel(' speed [rpm] ')
hold on
plot(TL,rpmsteady,'-.r')
axis([ TL(1) TL(count) 0 rpm(1) ])
title('Speed [rpm] vs. Load Torque [Ncm]')

subplot(2,2,3), plot(TL,Pout,'-y')
hold on
plot(TL,Pin,'-y')
hold on
plot(TL,Poutsteady,'-.r')
hold on
plot(TL,Pinsteady,'-.r')
%xlabel('load torque [N cm]')
%ylabel(' power [W] ')
axis([ TL(1) TL(count) 0 Pinsteady(count) ])
title('P-Out and In [W] vs. Load Torque [Ncm]')
```

```
subplot(2,2,4), plot(TL,eff,'-y')
%xlabel('load torque [N cm]')
%ylabel(' efficiency ')
hold on
plot(TL,effsteady,'-.r')
axis([ TL(1) TL(count) 0 max(eff) ])
title('Efficiency vs. Load Torque [Ncm]')
```

The following listing is the MATLAB script file for the function estimating the viscosity of the fill-fluid for the actual temperature:

```
function  viscosity = visc(viscair, oil, visc2, visc1, T2, T1, Tactual)

% visc(****) calculates the actual viscoity of the thruster unit
% fill fluid, using the actual temperature

if oil == 1
   % calculate oil viscosity at a specified temperature
   viscosity = ( (visc2-visc1)/(log(T2)-log(T1)) ) * ( log(Tactual)-log(T1) ) + visc1;
else
   viscosity = viscair;
end
```